

**JOINT VELOCITY SCALAR FILTERED DENSITY
FUNCTION FOR LARGE EDDY SIMULATION OF
TURBULENT REACTING FLOWS**

by

M. Reza Haji-Sheikhi

M.S., University at Buffalo, 2003

Submitted to the Graduate Faculty of
the School of Engineering in partial fulfillment
of the requirements for the degree of

Doctor of Philosophy

University of Pittsburgh

2005

UNIVERSITY OF PITTSBURGH
SCHOOL OF ENGINEERING

This dissertation was presented

by

M. Reza Haji-Sheikhi

It was defended on

December 1, 2005

and approved by

Dr. Peyman Givi, William Kepler Whiteford Professor of Mechanical Engineering

Dr. G. Paolo Galdi, Professor of Mechanical Engineering

Dr. Minking K. Chyu, Leighton Orr Professor and Chairman of Mechanical Engineering

Dr. Cristina H. Amon, Raymond J. Lane Distinguished Professor of Mechanical

Engineering, Carnegie Mellon University

Dissertation Director: Dr. Peyman Givi, William Kepler Whiteford Professor of

Mechanical Engineering

Copyright © by M. Reza Haji-Sheikhi
2005

JOINT VELOCITY SCALAR FILTERED DENSITY FUNCTION FOR LARGE EDDY SIMULATION OF TURBULENT REACTING FLOWS

M. Reza Haji-Sheikhi, PhD

University of Pittsburgh, 2005

The joint “velocity-scalar” filtered density function (FDF) methodology is developed and implemented for large eddy simulation (LES) of turbulent reacting flows. In FDF, the effects of the unresolved subgrid scales (SGS) are taken into account by considering the joint probability density function (PDF) of the velocity and scalar fields. An exact transport equation is derived for the FDF in which the effects of SGS convection and chemical reaction are in closed forms. The unclosed terms in this equation are modeled by considering an equivalent set of stochastic differential equations (SDEs) which is similar to that typically used in Reynolds-averaged simulation (RAS) procedures. The SDEs are solved numerically by a Lagrangian Monte Carlo procedure in which the Itô-Gikhman character of the SDEs is preserved. The consistency of the proposed SDEs and the convergence of the Monte Carlo solution are assessed. It is shown that the FDF results agree well with those obtained by a “conventional” finite-difference LES procedure in which the transport equations corresponding to the filtered quantities are solved directly. The FDF results are also compared with those obtained by the Smagorinsky closure, and all the results are assessed via comparison with data obtained by direct numerical simulation of a temporally developing mixing layer involving transport of a passive scalar. It is shown that all the first two moments including the scalar fluxes are predicted well by FDF. The predictive capabilities of the FDF are further demonstrated by LES of reacting shear flows. The predictions show favorable agreements with laboratory data, and demonstrate several of the features as observed experimentally.

TABLE OF CONTENTS

1.0 INTRODUCTION	1
1.1 Scope	2
2.0 JOINT VELOCITY SCALAR FILTERED DENSITY FUNCTION FOR CONSTANT-DENSITY FLOWS	3
2.1 Formulation	3
2.2 Velocity-Scalar Filtered Density Function (VSFDF)	6
2.2.1 Definitions	6
2.2.2 VSFDF Transport Equations	7
2.2.3 Modeled VSFDF Transport Equation	8
2.3 Numerical Solution Procedure	12
2.4 Flows Simulated	15
2.5 Numerical Specifications	16
2.6 Consistency and Convergence Assessments	17
2.7 Comparative Assessments of the VSFDF	18
3.0 JOINT VELOCITY SCALAR FILTERED MASS DENSITY FUNC- TION FOR VARIABLE-DENSITY FLOWS	40
3.1 Formulation	40
3.2 Velocity-Scalar Filtered Mass Density Function (VSF MDF)	46
3.2.1 Definitions	46
3.2.2 VSF MDF Transport Equations	47
3.2.3 Modeled VSF MDF Transport Equation	48
3.2.3.1 Model 1 (M1):	49

3.2.3.2 Model 2 (M2):	53
3.3 Numerical Solution Procedure	55
3.4 Flows Simulated	58
3.5 Reaction Mechanism	59
3.6 Numerical Specifications	60
3.7 Consistency Assessments	62
3.8 Validation via DNS	63
3.9 Validation via Laboratory Data	66
4.0 CONCLUSIONS	93
BIBLIOGRAPHY	96

LIST OF TABLES

1	Attributes of the computational methods.	14
2	Computational times for the three-dimensional temporal mixing layer simulations.	94

LIST OF FIGURES

1	Ensemble-averaging	21
2	Cross-stream variations of the Reynolds-averaged values of $\langle \rho \rangle$ at $t=34.3$: (a) $N_E = 40$, (b) $\Delta_E = \Delta/2$	22
3	Temporal evolution of the scalar (with superimposed vorticity iso-lines) (top) and the vorticity (bottom) fields for LES-FD, with $\Delta_E = \Delta/2$ and $N_E = 40$ at several times.	23
4	Temporal evolution of the scalar (with superimposed vorticity iso-lines) (top) and the vorticity (bottom) fields for VSFDF with $\Delta_E = \Delta/2$ and $N_E = 40$ at several times.	24
5	Statistical variability of LES-FD and VSFDF-C simulations with $N_E = 40$ for Reynolds-averaged values of $\tau(u, \phi)$ at $t=34.4$. Solid lines: LES-FD, dashed lines: VSFDF-C.	25
6	Statistical variability of LES-FD and VSFDF-C simulations with $N_E = 40$ for Reynolds-averaged values of $\tau(v, \phi)$ at $t=34.4$. Solid lines: LES-FD, dashed lines: VSFDF-C.	26
7	Cross-stream variations of the Reynolds-averaged values of $\tau(u, \phi)$ (a) $\Delta_E = \Delta/2$, (b) $\Delta_E = \Delta$, (c) $\Delta_E = 2\Delta$	27
8	Cross-stream variations of the Reynolds-averaged values of $\tau(v, \phi)$ (a) $\Delta_E = \Delta/2$, (b) $\Delta_E = \Delta$, (c) $\Delta_E = 2\Delta$	28
9	Cross-stream variations of the Reynolds-averaged values of $\tau(u, \phi)$ (a) $N_E = 20$, (b) $N_E = 40$, (c) $N_E = 80$	29

10	Cross-stream variations of the Reynolds-averaged values of $\tau(v, \phi)$ (a) $N_E = 20$, (b) $N_E = 40$, (c) $N_E = 80$	30
11	Contour surfaces of the $\langle \phi \rangle$ field in the 3D mixing layer at $t = 80$ as obtained by: (a) DNS, (b) Smagorinsky, (c) VSFDF.	31
12	Cross-stream variations of the Reynolds-averaged values of the filtered scalar field at $t = 80$	32
13	Temporal variations of the scalar thickness.	33
14	Cross stream variations of some of the components of τ at $t = 60$	34
15	Cross stream variations of some of the components of τ at $t = 80$	35
16	Cross-stream variations of some of the components of \bar{R} at $t = 60$	36
17	Cross-stream variations of some of the components of \bar{R} at $t = 80$	37
18	Cross-stream variations of some of the components of \bar{r} at $t = 60$	38
19	Cross-stream variations of some of the components of \bar{r} at $t = 80$	39
20	Concept of ensemble averaging. Shown are three different ensemble domains: $1(\Delta_E = \Delta/2)$, $2(\Delta_E = \Delta)$, $3(\Delta_E = 2\Delta)$. Black squares denote the finite-difference grid points, and the circles denote the MC particles.	68
21	Contours of the instantaneous filtered scalar field as obtained by: (a) LES-FD, (b) MC.	69
22	Cross-stream variations of the filtered density in the three-dimensional temporal mixing layer obtained from LES-FD and MC using M1 at $t = 60$	70
23	Cross-stream variations of the Reynolds-averaged values of (a) $\langle \phi \rangle_L$, (b) $\tau_L(\phi, \phi)$. The thick solid line denotes LES-FD predictions. The thin solid and dashed lines denote MC predictions via M1 and M2, respectively.	71
24	Scatter plots of density obtained at $t = 60$ from LES-FD ($\langle \rho \rangle_L$) and MC density ($\langle \rho \rangle^{MC}$, as given in Eq. (3.42)). The solid and dashed lines denote the linear regression and 45° lines, respectively. The parameter r denotes the correlation coefficient.	72
25	Scatter plots of velocity components at $t = 80$. (a) $\langle u \rangle_L$, (b) $\langle v \rangle_L$ and (c) $\langle w \rangle_L$. The solid and dashed lines denote the linear regression and 45° lines, respectively. The parameter r denotes the correlation coefficient.	73

26	Scatter plots of scalar statistics at $t = 80$. (a) $\langle\phi\rangle_L$, (b) $\tau_L(\phi, \phi)$. The solid and dashed lines denote the linear regression and 45° lines, respectively. The parameter r denotes the correlation coefficient.	74
27	Contour surfaces of the instantaneous $\langle\phi\rangle_L$ field in the 3D mixing layer at $t = 80$ as obtained by VSF MDF.	75
28	Contour plots of the spanwise vorticity field at $z = 0.75 L$, $t = 80$ in the 3D temporal mixing layer as obtained by: (a) DNS, (b) VSF MDF, (c) Smagorinsky.	76
29	Contour plots of $\langle\phi\rangle_L$ field on spanwise plane at $z = 0.75 L$, $t = 80$ in the 3D temporal mixing layer as obtained by: (a) DNS, (b) VSF MDF, (c) Smagorinsky.	77
30	Contour plots of the streamwise vorticity field at $x = 0.25 L$, $t = 80$ in the 3D temporal mixing layer as obtained by: (a) DNS, (b) VSF MDF, (c) Smagorinsky.	78
31	Contour plots of $\langle\phi\rangle_L$ field on streamwise plane at $x = 0.25 L$, $t = 80$ in the 3D temporal mixing layer as obtained by: (a) DNS, (b) VSF MDF, (c) Smagorinsky.	79
32	Cross-stream variations of the Reynolds-averaged values of the filtered temperature field at $t = 80$. The thick solid and dashed lines denote VSF MDF predictions via M1 and M2, respectively. The thin dashed line denote the predictions using Smagorinsky closure. The white and black circles show the filtered and unfiltered DNS data, respectively.	80
33	Temporal variation of (a) scalar thickness (δ_s), (b) momentum thickness. The solid and dashed lines denote predictions via VSF MDF (M1) and Smagorinsky closures, respectively. The circles show the filtered DNS data.	81
34	Cross-stream variations of some of the Reynolds-averaged components of τ_L at $t = 60$. The thick solid and dashed lines denote VSF MDF predictions via M1 and M2, respectively. The thin dashed line denote the predictions using Smagorinsky closure. The circles show the filtered DNS data.	82
35	Cross-stream variations of some of the Reynolds-averaged components of τ_L at $t = 80$. The thick solid and dashed lines denote VSF MDF predictions via M1 and M2, respectively. The thin dashed line denote the predictions using Smagorinsky closure. The circles show the filtered DNS data.	83

36	Cross-stream variations of some of the components of \overline{R} at $t = 60$. The thick solid and dashed lines denote VSF MDF predictions via M1 and M2, respectively. The thin dashed line denote the predictions using Smagorinsky closure. The circles show the filtered DNS data.	84
37	Cross-stream variations of some of the components of \overline{R} at $t = 80$. The thick solid and dashed lines denote VSF MDF predictions via M1 and M2, respectively. The thin dashed line denote the predictions using Smagorinsky closure. The circles show the filtered DNS data.	85
38	Cross-stream variations of \overline{r} at $t = 60$. The thick solid and dashed lines denote VSF MDF predictions via M1 and M2, respectively. The thin dashed line denote the predictions using Smagorinsky closure. The white and black circles show the filtered and unfiltered DNS data, respectively.	86
39	Cross-stream variations of \overline{r} at $t = 80$. The thick solid and dashed lines denote VSF MDF predictions via M1 and M2, respectively. The thin dashed line denote the predictions using Smagorinsky closure. The white and black circles show the filtered and unfiltered DNS data, respectively.	87
40	Contours of the instantaneous temperature [$^{\circ}K$] field on a spanwise plane as obtained by: (a) LES-FD, (b) MC.	88
41	Contour surfaces of the instantaneous filtered passive scalar field in the 3D spatial mixing layer simulations as obtained by VSF MDF.	89
42	Time series of filtered temperature field at different cross-stream locations across the layer and $x = 45.7\text{ cm}$ as obtained by VSF MDF. T_{max} denote the maximum temperature recorded by each probe.	90
43	Cross-stream variations of time-averaged filtered temperature field for the case with $\phi = 1$. The solid and dashes lines denote VSF MDF predictions using M1 and M2, respectively. The circles denote experimental data. T_{flm} denotes the adiabatic flame temperature.	91
44	Product thicknesses as obtained by VSF MDF: (a) Product thickness based on high-speed stream concentration, (b) Product thickness based on low-speed stream concentration.	92

ACKNOWLEDGMENTS

I would like to express my sincere appreciation to my advisor, Professor Peyman Givi for his support and guidance through the course of my research. I am grateful to the members of my doctoral committee, Professors Cristina H. Amon (Carnegie Mellon University), Minking K. Chyu and G. Paolo Galdi.

My appreciation also goes to Professor Farhad A. Jaberi (Michigan State University) for his collaboration on many technical aspects of my research. I owe special thanks to Professor Stephen B. Pope (Cornell University) whose insights and collaborations contributed greatly to the quality of my research. I am also indebted to Professors Cyrus K. Madnia and Dale B. Taulbee who contributed greatly to my education during my studies at the University at Buffalo.

I am indebted to my colleagues and friends in the Laboratory for Computational Transport Phenomena at the University of Pittsburgh, Mr. Mehdi Bostandoost Nik, Dr. Tomasz G. Drozda (Sandia National Laboratories), Mr. Mahdi Mohebbi and Mr. Server Levent Yilmaz. I am also thankful to Dr. Cristian R. Nastase (University of Wyoming) and Dr. Laurent Y.M. Gicquel (CERFACS, France) for their friendship and assistance during my earlier years in graduate school.

My deepest gratitude goes to my parents for providing me with the best possible education during my younger years. Their support and encouragement had a significant influence in my life. I have been blessed to have the companionship of my wife, Sheida and our daughters, Bahar and Nasim. Their love, support and patience through my Ph.D. program have been essential in seeing its completion. I dedicate this work to my family and my parents.

This work is part of a research sponsored by the U.S. Air Force Office of Scientific Research under Grant F49620-03-1-0022 (Program Manager: Dr. Julian M. Tishkoff), the

National Science Foundation under Grant CTS-0426857, and the Office of the Secretary of Defense through Contract FA9101-04-C-0014 with Arnold Air Force Base. Computational resources are provided by the Pittsburgh Supercomputing Center (PSC), the National Center for Supercomputing Applications (NCSA) at the University of Illinois at Urbana-Champaign, and the School of Engineering Computational Support Team at the University of Pittsburgh.

1.0 INTRODUCTION

The probability density function (PDF) approach has proven useful for large eddy simulation (LES) of turbulent reacting flows.¹⁻⁴ The formal means of conducting such LES is by considering the “filtered density function” (FDF)^{2,4} which is essentially the filtered fine-grained PDF of the transport quantities. The fundamental property of FDF is to account for the effects of subgrid-scale (SGS) fluctuations in a probabilistic manner.

The FDF, since its original conception,^{2,4} has become very popular in the combustion community.^{5,6} Most contributions so far are based on the marginal scalar FDF (SFDF), originally considered by Madnia and Givi⁷, Gao and O’Brien⁸, Colucci et al.⁹ and Jaber et al.¹⁰ This popularity is due to the capacity of this formulation to provide a closed form for the chemical reaction effect. However, in SFDF the effect of convection needs to be modeled similar to that in “conventional” LES. Gicquel et al.¹¹ developed the marginal FDF of the velocity vector (VFDF) in which the effect of SGS convection is in a closed form. However since the information about scalars is not embedded in the VFDF, this method is only suitable for constant-density, non-reacting flows. Following the developments as cited above, the FDF methodology has experienced widespread usage. Examples are contributions in its basic implementation,¹²⁻²³ fine-tuning of its sub-closures,^{24,25} and its validation via laboratory experiments.²⁶⁻³⁰ The FDF is finding its way into commercial codes^{31,32} and has been the subject of detailed discussions in several books,^{1,33-35} Givi³ provides a comprehensive review of the state of progress in LES/FDF.

The objective of this dissertation is to develop a more comprehensive FDF closure for LES of turbulent reacting flows. This is accomplished by considering the FDF of joint “velocity-scalars” (VSFDF). In this formulation, the SGS convection and chemical reaction are in closed forms. With definition of the FDF, the mathematical framework for its im-

plementation in LES is established. A transport equation is developed for the FDF. The unclosed terms in this equation are modeled in a fashion similar to those in Reynolds-averaged simulation (RAS) procedures.¹ A Lagrangian Monte Carlo procedure is developed and implemented for the numerical solution of the modeled FDF transport equation. The consistency of this procedure is assessed by comparing the first two scalar moments of the FDF with those obtained by the Eulerian finite-difference solutions of the same moments' transport equations. The joint VSFDF is considered first for constant-density flows. Subsequently, for the reacting flows with variations in fluid density, this methodology is extended by developing the joint “velocity-scalar filtered mass density function” (VSFMDF) method. Both methodologies are scrutinized extensively for consistency and accuracy. Furthermore, the predictive capabilities and the advantages of these methods over “conventional” LES closures are demonstrated.

1.1 SCOPE

This dissertation is organized as follows. In Chapter 2, the joint velocity-scalar filtered density function (VSFDF) for constant-density flows is considered. The work described in this chapter has been presented at several conferences^{36,37} and is published in *Physics of Fluids*.³⁸ In Chapter 3, the joint velocity-scalar filtered mass density function (VSFMDF) methodology is developed. This is an extension of VSFDF and accounts for the variations of fluid density. A shorter version of this chapter has been presented at several conferences^{39–41} and is currently under submission for publication. For the convenience of the readers, both of these chapters are self-contained. In Chapter 4, some final remarks regarding the methodologies are discussed, with some suggestions for future research.

2.0 JOINT VELOCITY SCALAR FILTERED DENSITY FUNCTION FOR CONSTANT-DENSITY FLOWS

In this chapter, the previously developed “marginal” FDF methodologies are extended to account for the “joint” SGS components of velocity and scalar fields. This is accomplished by considering the joint “velocity-scalar filtered density function” (VSFDF). Following its mathematical definition, the “exact” VSFDF transport equation is derived. The unclosed terms in this equation are modeled using an equivalent system of stochastic differential equations. A hybrid Eulerian/Lagrangian numerical solution procedure is developed. In the Eulerian part, the filtered transport equations are solved by finite-difference method. In the Lagrangian part, the solution of the modeled VSFDF transport equation is obtained by Monte Carlo method. The unclosed statistics in the Eulerian part are obtained from the Monte Carlo solver. Simulations are conducted of a temporally developing mixing layer in which, the consistency and accuracy of the methodology are established. The comparative capabilities of the VSFDF is assessed by comparing the predicted results with those of direct numerical simulation (DNS) and those obtained by the conventional LES via the Smagorinsky⁴² SGS closure. The sensitivity of the calculations to the model’s constants is assessed and it is shown that the first and the total components of the second order moments are not sensitive to these constants.

2.1 FORMULATION

For the general formulation, we consider an incompressible (unit density), isothermal, turbulent reacting flow involving N_s species. The primary transport variables describing such a

flow are the three components of the velocity vector $u_i(\mathbf{x}, t)$ ($i = 1, 2, 3$), the pressure $p(\mathbf{x}, t)$, and the species' mass fractions $\phi_\alpha(\mathbf{x}, t)$ ($\alpha = 1, 2, \dots, N_s$). The equations which govern the transport of these variables in space (x_i) and time (t) are

$$\frac{\partial u_k}{\partial x_k} = 0, \quad (2.1a)$$

$$\frac{\partial u_i}{\partial t} + \frac{\partial u_k u_i}{\partial x_k} = -\frac{\partial p}{\partial x_i} + \frac{\partial \sigma_{ik}}{\partial x_k}, \quad (2.1b)$$

$$\frac{\partial \phi_\alpha}{\partial t} + \frac{\partial u_k \phi_\alpha}{\partial x_k} = -\frac{\partial J_k^\alpha}{\partial x_k} + S_\alpha, \quad (2.1c)$$

where $S_\alpha \equiv \hat{S}_\alpha(\boldsymbol{\phi}(\mathbf{x}, t))$ denotes the chemical reaction term for species α , and $\boldsymbol{\phi} \equiv [\phi_1, \phi_2, \dots, \phi_{N_s}]$ denotes the scalar variable array. For an incompressible, Newtonian fluid, with Fick's law of diffusion, the viscous stress tensor σ_{ik} and the scalar flux J_k^α are represented by

$$\sigma_{ik} = \nu \left(\frac{\partial u_i}{\partial x_k} + \frac{\partial u_k}{\partial x_i} \right), \quad (2.2a)$$

$$J_k^\alpha = -\Gamma \frac{\partial \phi_\alpha}{\partial x_k}, \quad (2.2b)$$

where ν is the fluid kinematic viscosity and $\Gamma = \frac{\nu}{Sc}$ is the diffusion coefficient of all species with Sc denoting the molecular Schmidt number. We assume a constant value for $\nu = \Gamma$; *i.e.* $Sc = 1$. In reactive flows, molecular processes are much more complicated than portrayed by Eq. (2.2). Since the molecular diffusion is typically less important than that of SGS, this simple model is adopted with justifications and caveats given in Refs. ^{43–45}

Large eddy simulation involves the spatial filtering operation ^{1,46–49}

$$\langle f(\mathbf{x}, t) \rangle = \int_{-\infty}^{+\infty} f(\mathbf{x}', t) G(\mathbf{x}', \mathbf{x}) d\mathbf{x}', \quad (2.3)$$

where $G(\mathbf{x}', \mathbf{x})$ denotes a filter function, and $\langle f(\mathbf{x}, t) \rangle$ is the filtered value of the transport variable $f(\mathbf{x}, t)$. We consider a filter function that is spatially and temporally invariant and localized, thus: $G(\mathbf{x}', \mathbf{x}) \equiv G(\mathbf{x}' - \mathbf{x})$ with the properties $G(\mathbf{x}) \geq 0$, $\int_{-\infty}^{+\infty} G(\mathbf{x}) d\mathbf{x} = 1$.

Applying the filtering operation to Eqs. (2.1) yields

$$\frac{\partial \langle u_k \rangle}{\partial x_k} = 0, \quad (2.4a)$$

$$\frac{\partial \langle u_i \rangle}{\partial t} + \frac{\partial \langle u_k \rangle \langle u_i \rangle}{\partial x_k} = -\frac{\partial \langle p \rangle}{\partial x_i} + \nu \frac{\partial^2 \langle u_i \rangle}{\partial x_k \partial x_k} - \frac{\partial \tau(u_k, u_i)}{\partial x_k}, \quad (2.4b)$$

$$\frac{\partial \langle \phi_\alpha \rangle}{\partial t} + \frac{\partial \langle u_k \rangle \langle \phi_\alpha \rangle}{\partial x_k} = \nu \frac{\partial^2 \langle \phi_\alpha \rangle}{\partial x_k \partial x_k} - \frac{\partial \tau(u_k, \phi_\alpha)}{\partial x_k} + \langle S_\alpha \rangle, \quad (2.4c)$$

where the second-order SGS correlations

$$\tau(a, b) = \langle ab \rangle - \langle a \rangle \langle b \rangle, \quad (2.5)$$

are governed by

$$\begin{aligned} \frac{\partial \tau(u_i, u_j)}{\partial t} + \frac{\partial \langle u_k \rangle \tau(u_i, u_j)}{\partial x_k} &= \nu \frac{\partial^2 \tau(u_i, u_j)}{\partial x_k \partial x_k} - \tau(u_k, u_i) \frac{\partial \langle u_j \rangle}{\partial x_k} - \tau(u_k, u_j) \frac{\partial \langle u_i \rangle}{\partial x_k} \\ &- \left[2\nu \tau \left(\frac{\partial u_i}{\partial x_k}, \frac{\partial u_j}{\partial x_k} \right) + \tau \left(u_i, \frac{\partial p}{\partial x_j} \right) + \tau \left(u_j, \frac{\partial p}{\partial x_i} \right) \right] - \frac{\partial \tau(u_k, u_i, u_j)}{\partial x_k}, \end{aligned} \quad (2.6a)$$

$$\begin{aligned} \frac{\partial \tau(u_i, \phi_\alpha)}{\partial t} + \frac{\partial \langle u_k \rangle \tau(u_i, \phi_\alpha)}{\partial x_k} &= \nu \frac{\partial^2 \tau(u_i, \phi_\alpha)}{\partial x_k \partial x_k} - \tau(u_k, u_i) \frac{\partial \langle \phi_\alpha \rangle}{\partial x_k} - \tau(u_k, \phi_\alpha) \frac{\partial \langle u_i \rangle}{\partial x_k} \\ &- \left[2\nu \tau \left(\frac{\partial u_i}{\partial x_k}, \frac{\partial \phi_\alpha}{\partial x_k} \right) + \tau \left(\phi_\alpha, \frac{\partial p}{\partial x_i} \right) \right] + \tau(u_i, S_\alpha) - \frac{\partial \tau(u_k, u_i, \phi_\alpha)}{\partial x_k}, \end{aligned} \quad (2.6b)$$

$$\begin{aligned} \frac{\partial \tau(\phi_\alpha, \phi_\beta)}{\partial t} + \frac{\partial \langle u_k \rangle \tau(\phi_\alpha, \phi_\beta)}{\partial x_k} &= \nu \frac{\partial^2 \tau(\phi_\alpha, \phi_\beta)}{\partial x_k \partial x_k} - \tau(u_k, \phi_\alpha) \frac{\partial \langle \phi_\beta \rangle}{\partial x_k} - \tau(u_k, \phi_\beta) \frac{\partial \langle \phi_\alpha \rangle}{\partial x_k} \\ &- \left[2\nu \tau \left(\frac{\partial \phi_\alpha}{\partial x_k}, \frac{\partial \phi_\beta}{\partial x_k} \right) \right] + \tau(\phi_\alpha, S_\beta) + \tau(\phi_\beta, S_\alpha) - \frac{\partial \tau(u_k, \phi_\alpha, \phi_\beta)}{\partial x_k}. \end{aligned} \quad (2.6c)$$

In this equation, the third order correlations

$$\begin{aligned} \tau(a, b, c) &= \langle abc \rangle - \langle a \rangle \tau(b, c) \\ &- \langle b \rangle \tau(a, c) - \langle c \rangle \tau(a, b) - \langle a \rangle \langle b \rangle \langle c \rangle, \end{aligned} \quad (2.7)$$

are unclosed along with the other terms within square brackets.

2.2 VELOCITY-SCALAR FILTERED DENSITY FUNCTION (VSFDF)

2.2.1 Definitions

The “velocity-scalar filtered density function” (VSFDF), denoted by P , is formally defined as²

$$P(\mathbf{v}, \boldsymbol{\psi}; \mathbf{x}, t) = \int_{-\infty}^{+\infty} \varrho(\mathbf{v}, \boldsymbol{\psi}; \mathbf{u}(\mathbf{x}', t), \boldsymbol{\phi}(\mathbf{x}', t)) G(\mathbf{x}' - \mathbf{x}) d\mathbf{x}', \quad (2.8)$$

$$\varrho(\mathbf{v}, \boldsymbol{\psi}; \mathbf{u}(\mathbf{x}, t), \boldsymbol{\phi}(\mathbf{x}, t)) = \prod_{i=1}^3 \delta(v_i - u_i(\mathbf{x}, t)) \times \prod_{\alpha=1}^{N_s} \delta(\psi_\alpha - \phi_\alpha(\mathbf{x}, t)), \quad (2.9)$$

where δ denotes the delta function, and $\mathbf{v}, \boldsymbol{\psi}$ are the velocity vector and the scalar array in the sample space. The term ϱ is the “fine-grained” density,^{44,50} hence Eq. (2.8) defines VSFDF as the spatially filtered value of the fine-grained density. With the condition of a positive filter kernel,⁵¹ P has all of the properties of the PDF.⁴⁴ For further developments it is useful to define the “conditional filtered value” of the variable $Q(\mathbf{x}, t)$ as

$$\begin{aligned} \langle Q(\mathbf{x}, t) \mid \mathbf{u}(\mathbf{x}, t) = \mathbf{v}, \boldsymbol{\phi}(\mathbf{x}, t) = \boldsymbol{\psi} \rangle &\equiv \langle Q \mid \mathbf{v}, \boldsymbol{\psi} \rangle \\ &= \frac{\int_{-\infty}^{+\infty} Q(\mathbf{x}', t) \varrho(\mathbf{v}, \boldsymbol{\psi}; \mathbf{u}(\mathbf{x}', t), \boldsymbol{\phi}(\mathbf{x}', t)) G(\mathbf{x}' - \mathbf{x}) d\mathbf{x}'}{P(\mathbf{v}, \boldsymbol{\psi}; \mathbf{x}, t)}. \end{aligned} \quad (2.10)$$

Equation (2.10) implies the following:

$$(i) \quad \text{for } Q(\mathbf{x}, t) = c, \quad \langle Q(\mathbf{x}, t) \mid \mathbf{v}, \boldsymbol{\psi} \rangle = c, \quad (2.11a)$$

$$(ii) \quad \text{for } Q(\mathbf{x}, t) \equiv \hat{Q}(\mathbf{u}(\mathbf{x}, t), \boldsymbol{\phi}(\mathbf{x}, t)) \quad \langle Q(\mathbf{x}, t) \mid \mathbf{v}, \boldsymbol{\psi} \rangle = \hat{Q}(\mathbf{v}, \boldsymbol{\psi}), \quad (2.11b)$$

$$(iii) \quad \text{Integral properties:} \quad \langle Q(\mathbf{x}, t) \rangle = \quad (2.11c)$$

$$\int_{-\infty}^{+\infty} \int_{-\infty}^{+\infty} \langle Q(\mathbf{x}, t) \mid \mathbf{v}, \boldsymbol{\psi} \rangle P(\mathbf{v}, \boldsymbol{\psi}; \mathbf{x}, t) d\mathbf{v} d\boldsymbol{\psi}. \quad (2.11d)$$

From Eqs. (2.11) it follows that the filtered value of any function of the velocity and/or scalar variables is obtained by its integration over the velocity and scalar sample spaces

$$\langle Q(\mathbf{x}, t) \rangle = \int_{-\infty}^{+\infty} \int_{-\infty}^{+\infty} \hat{Q}(\mathbf{v}, \boldsymbol{\psi}) P(\mathbf{v}, \boldsymbol{\psi}; \mathbf{x}, t) d\mathbf{v} d\boldsymbol{\psi}. \quad (2.12)$$

2.2.2 VSFDF Transport Equations

To develop the VSFDF transport equation, we consider the time derivative of the fine-grained density function (Eq. (2.9))

$$\frac{\partial \varrho}{\partial t} = - \left(\frac{\partial u_k}{\partial t} \frac{\partial \varrho}{\partial v_k} + \frac{\partial \phi_\alpha}{\partial t} \frac{\partial \varrho}{\partial \psi_\alpha} \right). \quad (2.13)$$

Substituting Eqs. (2.1b), (2.1c), and Eqs. (2.2a), (2.2b) into Eq. (2.13) we obtain

$$\frac{\partial \varrho}{\partial t} + \frac{\partial u_k \varrho}{\partial x_k} = \left(\frac{\partial p}{\partial x_i} - \nu \frac{\partial^2 u_i}{\partial x_k \partial x_k} \right) \frac{\partial \varrho}{\partial v_i} - \left(\nu \frac{\partial^2 \phi_\alpha}{\partial x_k \partial x_k} + S_\alpha(\phi) \right) \frac{\partial \varrho}{\partial \psi_\alpha}. \quad (2.14)$$

Integration of this according to Eq. (2.8), while employing Eq. (2.10) results in

$$\begin{aligned} \frac{\partial P}{\partial t} + \frac{\partial v_k P}{\partial x_k} &= \frac{\partial \langle p \rangle}{\partial x_k} \frac{\partial P}{\partial v_k} - \frac{\partial}{\partial \psi_\alpha} [S_\alpha(\psi) P] \\ &+ \frac{\partial}{\partial v_k} \left[\left(\left\langle \frac{\partial p}{\partial x_k} \middle| \mathbf{v}, \boldsymbol{\psi} \right\rangle - \frac{\partial \langle p \rangle}{\partial x_k} \right) P \right], \\ &- \frac{\partial}{\partial v_i} \left(\left\langle \nu \frac{\partial^2 u_i}{\partial x_k \partial x_k} \middle| \mathbf{v}, \boldsymbol{\psi} \right\rangle P \right), \\ &- \frac{\partial}{\partial \psi_\alpha} \left(\left\langle \nu \frac{\partial^2 \phi_\alpha}{\partial x_k \partial x_k} \middle| \mathbf{v}, \boldsymbol{\psi} \right\rangle P \right). \end{aligned} \quad (2.15)$$

This is an exact transport equation for the VSFDF. It is observed that the effects of convection (second term on LHS) and chemical reaction (the second term on RHS) appear in closed forms. The unclosed terms denote convective effects in the velocity-scalar sample space. Alternatively, the VSFDF equation can be expressed as

$$\begin{aligned} \frac{\partial P}{\partial t} + \frac{\partial v_k P}{\partial x_k} &= \nu \frac{\partial^2 P}{\partial x_k \partial x_k} + \frac{\partial \langle p \rangle}{\partial x_k} \frac{\partial P}{\partial v_k} - \frac{\partial}{\partial \psi_\alpha} [S_\alpha(\psi) P] \\ &+ \frac{\partial}{\partial v_k} \left[\left(\left\langle \frac{\partial p}{\partial x_k} \middle| \mathbf{v}, \boldsymbol{\psi} \right\rangle - \frac{\partial \langle p \rangle}{\partial x_k} \right) P \right] \\ &- \frac{\partial^2}{\partial v_i \partial v_j} \left[\left\langle \nu \frac{\partial u_i}{\partial x_k} \frac{\partial u_j}{\partial x_k} \middle| \mathbf{v}, \boldsymbol{\psi} \right\rangle P \right] \\ &- 2 \frac{\partial^2}{\partial v_i \partial \psi_\alpha} \left[\left\langle \nu \frac{\partial u_i}{\partial x_k} \frac{\partial \phi_\alpha}{\partial x_k} \middle| \mathbf{v}, \boldsymbol{\psi} \right\rangle P \right] \\ &- \frac{\partial^2}{\partial \psi_\alpha \partial \psi_\beta} \left[\left\langle \nu \frac{\partial \phi_\alpha}{\partial x_k} \frac{\partial \phi_\beta}{\partial x_k} \middle| \mathbf{v}, \boldsymbol{\psi} \right\rangle P \right]. \end{aligned} \quad (2.16)$$

This is also an exact equation, but the unclosed terms are exhibited by the conditional filtered values of the dissipation fields as shown by the last three terms on the RHS.

2.2.3 Modeled VSFDF Transport Equation

For closure of the VSFDF transport equation, we consider the general diffusion process,⁵² given by the system of stochastic differential equations (SDEs):

$$\begin{aligned} dX_i^+(t) &= D_i^X(\mathbf{X}^+, \mathbf{U}^+, \phi^+; t)dt + B_{ij}^X(\mathbf{X}^+, \mathbf{U}^+, \phi^+; t)dW_j^X(t) \\ &+ F_{ij}^{XU}(\mathbf{X}^+, \mathbf{U}^+, \phi^+; t)dW_j^U(t) + F_{ij}^{X\phi}(\mathbf{X}^+, \mathbf{U}^+, \phi^+; t)dW_j^\phi(t), \end{aligned} \quad (2.17a)$$

$$\begin{aligned} dU_i^+(t) &= D_i^U(\mathbf{X}^+, \mathbf{U}^+, \phi^+; t)dt + B_{ij}^U(\mathbf{X}^+, \mathbf{U}^+, \phi^+; t)dW_j^U(t) \\ &+ F_{ij}^{UX}(\mathbf{X}^+, \mathbf{U}^+, \phi^+; t)dW_j^X(t) + F_{ij}^{U\phi}(\mathbf{X}^+, \mathbf{U}^+, \phi^+; t)dW_j^\phi(t), \end{aligned} \quad (2.17b)$$

$$\begin{aligned} d\phi_\alpha^+(t) &= D_\alpha^\phi(\mathbf{X}^+, \mathbf{U}^+, \phi^+; t)dt + B_{\alpha j}^\phi(\mathbf{X}^+, \mathbf{U}^+, \phi^+; t)dW_j^\phi(t) \\ &+ F_{\alpha j}^{\phi X}(\mathbf{X}^+, \mathbf{U}^+, \phi^+; t)dW_j^X(t) + F_{\alpha j}^{\phi U}(\mathbf{X}^+, \mathbf{U}^+, \phi^+; t)dW_j^U(t). \end{aligned} \quad (2.17c)$$

where $X_i^+, U_i^+, \phi_\alpha^+$ are probabilistic representations of position, velocity vector, and scalar variables, respectively. The D terms denote drift in the composition space, the B terms denote diffusion, the F terms denote diffusion couplings, and the W terms denote the Wiener-Lévy processes.^{53,54} Following Refs.,^{9,11,55,56} we consider the generalized Langevin model (GLM) and the linear mean square estimation (LMSE) model⁵⁰

$$dX_i^+ = U_i^+ dt + \sqrt{\nu_1} dW_i^X, \quad (2.18a)$$

$$\begin{aligned} dU_i^+ &= \left[-\frac{\partial \langle p \rangle}{\partial x_i} + \nu_2 \frac{\partial^2 \langle u_i \rangle}{\partial x_k \partial x_k} + G_{ij} (U_j^+ - \langle u_j \rangle) \right] dt \\ &+ \sqrt{\nu_3} \frac{\partial \langle u_i \rangle}{\partial x_k} dW_k^X + \sqrt{C_0 \epsilon} dW_i^U, \end{aligned} \quad (2.18b)$$

$$\begin{aligned} d\phi_\alpha^+ &= \left[\nu_{S1} \frac{\partial^2 \langle \phi_\alpha \rangle}{\partial x_k \partial x_k} - C_\phi \omega (\phi_\alpha^+ - \langle \phi_\alpha \rangle) + S_\alpha(\psi) \right] dt \\ &+ \sqrt{\nu_{S2}} \frac{\partial \langle \phi_\alpha \rangle}{\partial x_k} dW_k^X, \end{aligned} \quad (2.18c)$$

where the variables ν_1, ν_2, \dots are all diffusion coefficients (to be specified), and

$$\begin{aligned} G_{ij} &= -\omega \left(\frac{1}{2} + \frac{3}{4} C_0 \right) \delta_{ij}, \quad \omega = \frac{\epsilon}{k}, \\ \epsilon &= C_\epsilon \frac{k^{3/2}}{\Delta_L}, \quad k = \frac{1}{2} \tau (u_k, u_k). \end{aligned} \quad (2.19)$$

Here ω is the SGS mixing frequency, ϵ is the SGS dissipation rate, k is the SGS kinetic energy, and Δ_L is the LES filter size. The parameters C_0 , C_ϕ and C_ϵ are model constants

and need to be specified. The limit $\nu_1 = \nu_3 = \nu_{S_1} = \nu_{S_2} = 0$ is the standard high Reynolds number GLM-LMSE closure.⁴⁴

The Fokker-Planck equation⁵⁷ for $f(\mathbf{v}, \boldsymbol{\psi}, \mathbf{x}, t)$, the joint PDF of $\mathbf{X}^+, \mathbf{U}^+, \boldsymbol{\phi}^+$, evolving by the diffusion process as given by Eq. (2.18) is:

$$\begin{aligned}
\frac{\partial f}{\partial t} + \frac{\partial}{\partial x_k} (v_k f) &= \left[\frac{\partial \langle p \rangle}{\partial x_i} - (\nu_2 - \sqrt{\nu_1 \nu_3}) \frac{\partial^2 \langle u_i \rangle}{\partial x_k \partial x_k} \right] \frac{\partial f}{\partial v_i} - \frac{\partial}{\partial v_i} [G_{ij} (v_j - \langle u_j \rangle) f] \\
&- [\nu_{S_1} - \sqrt{\nu_1 \nu_{S_2}}] \frac{\partial^2 \langle \phi_\alpha \rangle}{\partial x_k \partial x_k} \frac{\partial f}{\partial \psi_\alpha} + \frac{\partial}{\partial \psi_\alpha} [C_{\phi\omega} (\psi_\alpha - \langle \phi_\alpha \rangle) f] - \frac{\partial}{\partial \psi_\alpha} [S_\alpha(\boldsymbol{\psi}) f] \\
&+ \frac{\nu_1}{2} \frac{\partial^2 f}{\partial x_k \partial x_k} + \sqrt{\nu_1 \nu_3} \frac{\partial \langle u_j \rangle}{\partial x_i} \frac{\partial^2 f}{\partial x_i \partial v_j} + \sqrt{\nu_1 \nu_{S_2}} \frac{\partial \langle \phi_\alpha \rangle}{\partial x_i} \frac{\partial^2 f}{\partial x_i \partial \psi_\alpha} \\
&+ \frac{\nu_3}{2} \frac{\partial \langle u_i \rangle}{\partial x_k} \frac{\partial \langle u_j \rangle}{\partial x_k} \frac{\partial^2 f}{\partial v_i \partial v_j} + \frac{1}{2} C_0 \epsilon \frac{\partial^2 f}{\partial v_k \partial v_k} + \sqrt{\nu_3 \nu_{S_2}} \frac{\partial \langle u_i \rangle}{\partial x_k} \frac{\partial \langle \phi_\alpha \rangle}{\partial x_k} \frac{\partial^2 f}{\partial v_i \partial \psi_\alpha} \\
&+ \frac{\nu_{S_2}}{2} \frac{\partial \langle \phi_\alpha \rangle}{\partial x_k} \frac{\partial \langle \phi_\beta \rangle}{\partial x_k} \frac{\partial^2 f}{\partial \psi_\alpha \partial \psi_\beta}, \tag{2.20}
\end{aligned}$$

The transport equations for the filtered variables are obtained by integration of Eq. (2.20) according to Eq. (2.12):

$$\frac{\partial \langle u_k \rangle}{\partial x_k} = 0, \tag{2.21a}$$

$$\frac{\partial \langle u_i \rangle}{\partial t} + \frac{\partial \langle u_k \rangle \langle u_i \rangle}{\partial x_k} = -\frac{\partial \langle p \rangle}{\partial x_i} + \left(\frac{\nu_1}{2} + \nu_2 - \sqrt{\nu_1 \nu_3} \right) \frac{\partial^2 \langle u_i \rangle}{\partial x_k \partial x_k} - \frac{\partial \tau(u_k, u_i)}{\partial x_k}, \tag{2.21b}$$

$$\frac{\partial \langle \phi_\alpha \rangle}{\partial t} + \frac{\partial \langle u_k \rangle \langle \phi_\alpha \rangle}{\partial x_k} = \left(\nu_{S_1} - \sqrt{\nu_1 \nu_{S_2}} + \frac{\nu_1}{2} \right) \frac{\partial^2 \langle \phi_\alpha \rangle}{\partial x_k \partial x_k} + \langle S_\alpha(\boldsymbol{\phi}) \rangle - \frac{\partial \tau(u_k, \phi_\alpha)}{\partial x_k}. \tag{2.21c}$$

The transport equations for the second order SGS moments are

$$\begin{aligned}
\frac{\partial \tau(u_i, u_j)}{\partial t} + \frac{\partial \langle u_k \rangle \tau(u_i, u_j)}{\partial x_k} &= \frac{\nu_1}{2} \frac{\partial^2 \tau(u_i, u_j)}{\partial x_k \partial x_k} - \tau(u_k, u_i) \frac{\partial \langle u_j \rangle}{\partial x_k} - \tau(u_k, u_j) \frac{\partial \langle u_i \rangle}{\partial x_k} \\
&+ (\nu_1 - 2\sqrt{\nu_1 \nu_3} + \nu_3) \frac{\partial \langle u_i \rangle}{\partial x_k} \frac{\partial \langle u_j \rangle}{\partial x_k} \\
&+ [G_{ik} \tau(u_k, u_j) + G_{jk} \tau(u_k, u_i) + C_0 \epsilon \delta_{ij}] - \frac{\partial \tau(u_k, u_i, u_j)}{\partial x_k}, \tag{2.22a}
\end{aligned}$$

$$\begin{aligned}
\frac{\partial \tau(u_i, \phi_\alpha)}{\partial t} + \frac{\partial \langle u_k \rangle \tau(u_i, \phi_\alpha)}{\partial x_k} &= \frac{\nu_1}{2} \frac{\partial^2 \tau(u_i, \phi_\alpha)}{\partial x_k \partial x_k} - \tau(u_k, u_i) \frac{\partial \langle \phi_\alpha \rangle}{\partial x_k} - \tau(u_k, \phi_\alpha) \frac{\partial \langle u_i \rangle}{\partial x_k} \\
&+ (\nu_1 - \sqrt{\nu_1 \nu_3} - \sqrt{\nu_1 \nu_{S_2}} + \sqrt{\nu_3 \nu_{S_2}}) \frac{\partial \langle u_i \rangle}{\partial x_k} \frac{\partial \langle \phi_\alpha \rangle}{\partial x_k} \\
&+ [G_{ik} \tau(u_k, \phi_\alpha) - C_{\phi\omega} \tau(u_i, \phi_\alpha)] + \tau(u_i, S_\alpha) - \frac{\partial \tau(u_k, u_i, \phi_\alpha)}{\partial x_k},
\end{aligned} \tag{2.22b}$$

$$\begin{aligned}
\frac{\partial \tau(\phi_\alpha, \phi_\beta)}{\partial t} + \frac{\partial \langle u_k \rangle \tau(\phi_\alpha, \phi_\beta)}{\partial x_k} &= \frac{\nu_1}{2} \frac{\partial^2 \tau(\phi_\alpha, \phi_\beta)}{\partial x_k \partial x_k} - \tau(u_k, \phi_\alpha) \frac{\partial \langle \phi_\beta \rangle}{\partial x_k} - \tau(u_k, \phi_\beta) \frac{\partial \langle \phi_\alpha \rangle}{\partial x_k} \\
&+ (\nu_1 - 2\sqrt{\nu_1 \nu_{S_2}} + \nu_{S_2}) \frac{\partial \langle \phi_\alpha \rangle}{\partial x_k} \frac{\partial \langle \phi_\beta \rangle}{\partial x_k} \\
&- [2C_{\phi\omega} \tau(\phi_\alpha, \phi_\beta)] + \tau(\phi_\alpha, S_\beta) + \tau(\phi_\beta, S_\alpha) - \frac{\partial \tau(u_k, \phi_\alpha, \phi_\beta)}{\partial x_k}.
\end{aligned} \tag{2.22c}$$

A term-by-term comparison of the exact moment transport equations (Eqs. (2.4), (2.6)), with the modeled equations (Eqs. (2.21), (2.22)), suggests $\nu_1 = \nu_2 = \nu_3 = \nu_{S_1} = \nu_{S_2} = 2\nu$. However, this violates the realizability of the scalar field. A set of coefficients yielding a realizable stochastic model requires: $\nu_1 = \nu_2 = \nu_3 = 2\nu$ and $\nu_{S_1} = \nu_{S_2} = 0$. That is,

$$dX_i^+ = U_i^+ dt + \sqrt{2\nu} dW_i^X, \tag{2.23a}$$

$$\begin{aligned}
dU_i^+ &= \left[-\frac{\partial \langle p \rangle}{\partial x_i} + 2\nu \frac{\partial^2 \langle u_i \rangle}{\partial x_k \partial x_k} + G_{ij} (U_j^+ - \langle u_j \rangle) \right] dt \\
&+ \sqrt{2\nu} \frac{\partial \langle u_i \rangle}{\partial x_k} dW_k^X + \sqrt{C_0 \epsilon} dW_i^U,
\end{aligned} \tag{2.23b}$$

$$d\phi_\alpha^+ = -C_{\phi\omega} (\phi_\alpha^+ - \langle \phi_\alpha \rangle) dt. \tag{2.23c}$$

The Fokker-Planck equation for this system is

$$\begin{aligned}
\frac{\partial f}{\partial t} + \frac{\partial}{\partial x_k} (v_k f) &= \frac{\partial \langle p \rangle}{\partial x_i} \frac{\partial f}{\partial v_i} - \frac{\partial}{\partial v_i} [G_{ij} (v_j - \langle u_j \rangle) f] + \frac{\partial}{\partial \psi_\alpha} [C_{\phi\omega} (\psi_\alpha - \langle \phi_\alpha \rangle) f] \\
&+ \nu \frac{\partial^2 f}{\partial x_k \partial x_k} + 2\nu \frac{\partial \langle u_j \rangle}{\partial x_i} \frac{\partial^2 f}{\partial x_i \partial v_j} + \nu \frac{\partial \langle u_i \rangle}{\partial x_k} \frac{\partial \langle u_j \rangle}{\partial x_k} \frac{\partial^2 f}{\partial v_i \partial v_j} + \frac{1}{2} C_0 \epsilon \frac{\partial^2 f}{\partial v_k \partial v_k},
\end{aligned} \tag{2.24}$$

and the corresponding equations for the moments are:

$$\frac{\partial \langle u_k \rangle}{\partial x_k} = 0, \quad (2.25a)$$

$$\frac{\partial \langle u_i \rangle}{\partial t} + \frac{\partial \langle u_k \rangle \langle u_i \rangle}{\partial x_k} = -\frac{\partial \langle p \rangle}{\partial x_i} + \nu \frac{\partial^2 \langle u_i \rangle}{\partial x_k \partial x_k} - \frac{\partial \tau(u_k, u_i)}{\partial x_k}, \quad (2.25b)$$

$$\frac{\partial \langle \phi_\alpha \rangle}{\partial t} + \frac{\partial \langle u_k \rangle \langle \phi_\alpha \rangle}{\partial x_k} = \nu \frac{\partial^2 \langle \phi_\alpha \rangle}{\partial x_k \partial x_k} - \frac{\partial \tau(u_k, \phi_\alpha)}{\partial x_k}, \quad (2.25c)$$

$$\begin{aligned} \frac{\partial \tau(u_i, u_j)}{\partial t} + \frac{\partial \langle u_k \rangle \tau(u_i, u_j)}{\partial x_k} &= \nu \frac{\partial^2 \tau(u_i, u_j)}{\partial x_k \partial x_k} - \tau(u_k, u_i) \frac{\partial \langle u_j \rangle}{\partial x_k} - \tau(u_k, u_j) \frac{\partial \langle u_i \rangle}{\partial x_k} \\ &+ [G_{ik} \tau(u_k, u_j) + G_{jk} \tau(u_k, u_i) + C_0 \epsilon \delta_{ij}] - \frac{\partial \tau(u_k, u_i, u_j)}{\partial x_k}, \end{aligned} \quad (2.26a)$$

$$\begin{aligned} \frac{\partial \tau(u_i, \phi_\alpha)}{\partial t} + \frac{\partial \langle u_k \rangle \tau(u_i, \phi_\alpha)}{\partial x_k} &= \nu \frac{\partial^2 \tau(u_i, \phi_\alpha)}{\partial x_k \partial x_k} - \tau(u_k, u_i) \frac{\partial \langle \phi_\alpha \rangle}{\partial x_k} - \tau(u_k, \phi_\alpha) \frac{\partial \langle u_i \rangle}{\partial x_k} \\ &+ [G_{ik} \tau(u_k, \phi_\alpha) - C_\phi \omega \tau(u_i, \phi_\alpha)] + \tau(u_i, S_\alpha) - \frac{\partial \tau(u_k, u_i, \phi_\alpha)}{\partial x_k}, \end{aligned} \quad (2.26b)$$

$$\begin{aligned} \frac{\partial \tau(\phi_\alpha, \phi_\beta)}{\partial t} + \frac{\partial \langle u_k \rangle \tau(\phi_\alpha, \phi_\beta)}{\partial x_k} &= \nu \frac{\partial^2 \tau(\phi_\alpha, \phi_\beta)}{\partial x_k \partial x_k} - \tau(u_k, \phi_\alpha) \frac{\partial \langle \phi_\beta \rangle}{\partial x_k} - \tau(u_k, \phi_\beta) \frac{\partial \langle \phi_\alpha \rangle}{\partial x_k} \\ &+ \left[2\nu \frac{\partial \langle \phi_\alpha \rangle}{\partial x_k} \frac{\partial \langle \phi_\beta \rangle}{\partial x_k} - 2C_\phi \omega \tau(\phi_\alpha, \phi_\beta) \right] + \tau(\phi_\alpha, S_\beta) + \tau(\phi_\beta, S_\alpha) \\ &- \frac{\partial \tau(u_k, \phi_\alpha, \phi_\beta)}{\partial x_k}, \end{aligned} \quad (2.26c)$$

which may be compared to Eqs. (2.4) and (2.6). Therefore, the stochastic diffusion process described by the SDEs (2.23) implies the following closure for the VSFDF:

$$\begin{aligned} &\frac{\partial}{\partial v_k} \left[\left(\left\langle \frac{\partial p}{\partial x_k} \middle| \mathbf{v}, \boldsymbol{\psi} \right\rangle - \frac{\partial \langle p \rangle}{\partial x_k} \right) P \right] - \nu \frac{\partial^2}{\partial v_i \partial v_j} \left[\left\langle \frac{\partial u_i}{\partial x_k} \frac{\partial u_j}{\partial x_k} \middle| \mathbf{v}, \boldsymbol{\psi} \right\rangle P \right] \\ &- 2\nu \frac{\partial^2}{\partial v_i \partial \psi_\alpha} \left[\left\langle \frac{\partial u_i}{\partial x_k} \frac{\partial \psi_\alpha}{\partial x_k} \middle| \mathbf{v}, \boldsymbol{\psi} \right\rangle P \right] - \nu \frac{\partial^2}{\partial \psi_\alpha \partial \psi_\beta} \left[\left\langle \frac{\partial \psi_\alpha}{\partial x_k} \frac{\partial \psi_\beta}{\partial x_k} \middle| \mathbf{v}, \boldsymbol{\psi} \right\rangle P \right] \\ &\approx \nu \frac{\partial \langle u_i \rangle}{\partial x_k} \frac{\partial \langle u_j \rangle}{\partial x_k} \frac{\partial^2 f}{\partial v_i \partial v_j} + \frac{1}{2} C_0 \epsilon \frac{\partial^2 f}{\partial v_k \partial v_k} + 2\nu \frac{\partial \langle u_i \rangle}{\partial x_k} \frac{\partial^2 f}{\partial x_k \partial v_i} \\ &\quad - \frac{\partial}{\partial v_i} [G_{ij} (v_j - \langle u_j \rangle) f] + \frac{\partial}{\partial \psi_\alpha} [C_\phi \omega (\psi_\alpha - \langle \phi_\alpha \rangle) f], \end{aligned} \quad (2.27)$$

which yields the closures at the second order levels:

$$\begin{aligned}
- \left[2\nu \tau \left(\frac{\partial u_i}{\partial x_k}, \frac{\partial u_j}{\partial x_k} \right) + \tau \left(u_i, \frac{\partial p}{\partial x_j} \right) + \tau \left(u_j, \frac{\partial p}{\partial x_i} \right) \right] &= G_{ik} \tau(u_k, u_j) + G_{jk} \tau(u_k, u_i) + C_0 \epsilon \delta_{ij} \\
&= -\omega \left(1 + \frac{3}{2} C_0 \right) \left[\tau(u_i, u_j) - \frac{2}{3} k \delta_{ij} \right] - \frac{2}{3} \epsilon \delta_{ij}, \quad (2.28a)
\end{aligned}$$

$$\begin{aligned}
- \left[2\nu \tau \left(\frac{\partial u_i}{\partial x_k}, \frac{\partial \phi_\alpha}{\partial x_k} \right) + \tau \left(\phi_\alpha, \frac{\partial p}{\partial x_i} \right) \right] &= G_{ik} \tau(u_k, \phi_\alpha) - C_\phi \omega \tau(u_i, \phi_\alpha) \\
&= -\omega \left(\frac{1}{2} + \frac{3}{4} C_0 + C_\phi \right) \tau(u_i, \phi_\alpha), \quad (2.28b)
\end{aligned}$$

$$- 2\nu \tau \left(\frac{\partial \phi_\alpha}{\partial x_k}, \frac{\partial \phi_\beta}{\partial x_k} \right) = -2C_\phi \omega \tau(\phi_\alpha, \phi_\beta) + 2\nu \frac{\partial \langle \phi_\alpha \rangle}{\partial x_k} \frac{\partial \langle \phi_\beta \rangle}{\partial x_k}. \quad (2.28c)$$

This indicates a spurious source term in the scalar covariance equation, which is negligible at high Reynolds number flows.

2.3 NUMERICAL SOLUTION PROCEDURE

Numerical solution of the modeled VSFDF transport equation is obtained by a hybrid finite difference-Monte Carlo procedure. The basis is similar to those in RAS^{58,59} and in previous FDF simulations,⁹⁻¹¹ with some differences which are described here. For simulations, the FDF is represented by an ensemble of N_p statistically identical Monte Carlo (MC) particles. Each particle carries information pertaining to its position, $\mathbf{X}^{(n)}(t)$, velocity, $\mathbf{U}^{(n)}(t)$, and scalar value, $\phi^{(n)}(t)$, $n = 1, \dots, N_p$. This information is updated via temporal integration of the SDEs. The simplest way of performing this integration is via Euler-Maruyama approximation.⁶⁰ For example, for Eq. (2.17a),

$$\begin{aligned}
X_i^n(t_{k+1}) &= X_i^n(t_k) + (D_i^X(t_k))^n \Delta t + (B_{ij}^X(t_k))^n (\Delta t)^{1/2} (\zeta_j^X(t_k))^n \\
&+ (F_{ij}^{XU}(t_k))^n (\Delta t)^{1/2} (\zeta_j^U(t_k))^n + (F_{ij}^{X\phi}(t_k))^n (\Delta t)^{1/2} (\zeta_j^\phi(t_k))^n, \quad (2.29)
\end{aligned}$$

where $D_i(t_k) = D_i(\mathbf{X}^{(n)}(t_k), \mathbf{U}^{(n)}(t_k), \phi^{(n)}(t_k); t_k), \dots$, and $\zeta(t_k)$'s are independent standardized Gaussian random variables. This scheme preserves the Itô character of the SDEs.⁶¹

The computational domain is discretized on equally spaced finite-difference grid points. These points are used for two purposes: (1) to identify the regions where the statistical information from the MC simulations are obtained, (2) to perform a set of complementary LES primarily by the finite-difference methodology for assessing the consistency and convergence of the MC results. The LES procedure via the finite-difference discretization is referred to as LES-FD and will be further discussed below. Statistical information is obtained by considering an ensemble of N_E computational particles residing within an ensemble domain of characteristic length Δ_E centered around each of the finite-difference grid points. This is illustrated schematically in Fig. 1. For reliable statistics with minimal numerical dispersion, it is desired to minimize the size of ensemble domain and maximize the number of the MC particles.⁴⁴ In this way, the ensemble statistics would tend to the desired filtered values:

$$\begin{aligned} \langle a \rangle_E &\equiv \frac{1}{N_E} \sum_{n \in \Delta_E} a^{(n)} \xrightarrow[\Delta_E \rightarrow 0]{N_E \rightarrow \infty} \langle a \rangle, \\ \tau_E(a, b) &\equiv \frac{1}{N_E} \sum_{n \in \Delta_E} (a^{(n)} - \langle a \rangle_E) (b^{(n)} - \langle b \rangle_E) \xrightarrow[\Delta_E \rightarrow 0]{N_E \rightarrow \infty} \tau(a, b), \end{aligned} \quad (2.30)$$

where $a^{(n)}$ denotes the information carried by n^{th} MC particle pertaining to transport variable a .

The LES-FD solver is based on the compact parameter finite-difference scheme.^{62,63} This is a variant of the MacCormack scheme in which fourth-order compact differencing schemes are used to approximate the spatial derivatives, and second-order symmetric predictor-corrector sequence is employed for time discretization. All of the finite-difference operations are conducted on fixed grid points. The transfer of information from the grid points to the MC particles is accomplished via a second-order interpolation. The transfer of information from the particles to the grid points is accomplished via ensemble averaging as described above.

The LES-FD procedure determines the pressure field which is used in the MC solver. The LES-FD also determines the filtered velocity and scalar fields. That is, there is a

“redundancy” in the determination of the first filtered moments as both the LES-FD and the MC procedures provides the solution of this field. This redundancy is actually very useful in monitoring the accuracy of the simulated results as shown in previous works. [10,11,58,59](#) To establish consistency and convergence of the MC solver, the modeled transport equations for the generalized second order SGS moments (Eq. (2.26)) are also solved via LES-FD. In doing so, the unclosed third order correlations are taken from the MC solver. The comparison of the first and second order moments as obtained by LES-FD with those obtained by the MC solver is useful to establish the accuracy of the MC solver. These simulations are referred to as VSFDF-C. Attributes of all the simulation procedures are summarized in Table 1. In this table and hereinafter, VSFDF simulations refer to the hybrid MC/LES-FD procedure in which the LES-FD is used for only the first order filtered variables. In VSFDF-C, the LES-FD procedure is used for both first and second order filtered values. Further discussions about the simulation methods are available in Refs. [9,11,58,59](#)

Table 1: Attributes of the computational methods.

	LES-FD variables	VSFDF variables	VSFDF quantities used by the LES-FD system	LES-FD quantities used by the VSFDF system	Redundant quantities
VSFDF	$\langle p \rangle, \langle u_i \rangle$ $\langle \phi_\alpha \rangle$	X_i^+ U_i^+ ϕ_α^+	$\tau(u_i, u_j)$ $\tau(u_i, \phi_\alpha)$ $\langle S_\alpha(\phi) \rangle$	$\langle u_i \rangle, \frac{\partial \langle p \rangle}{\partial x_i}$ $\frac{\partial \langle u_i \rangle}{\partial x_k}, \frac{\partial^2 \langle u_i \rangle}{\partial x_k \partial x_k}$ $\langle \phi_\alpha \rangle$	$\langle u_i \rangle$ $\langle \phi_\alpha \rangle$
VSFDF-C	$\langle p \rangle, \langle u_i \rangle$ $\langle \phi_\alpha \rangle$ $\tau(u_i, u_j)$ $\tau(u_i, \phi_\alpha)$ $\tau(\phi_\alpha, \phi_\beta)$	X_i^+ U_i^+ ϕ_α^+	$\tau(u_i, u_j)$ $\tau(u_i, \phi_\alpha)$ $\tau(u_i, u_j, u_k)$ $\tau(u_i, u_j, \phi_\alpha)$ $\tau(u_i, \phi_\alpha, \phi_\beta)$	$\langle u_i \rangle, \frac{\partial \langle p \rangle}{\partial x_i}$ $\frac{\partial \langle u_i \rangle}{\partial x_k}, \frac{\partial^2 \langle u_i \rangle}{\partial x_k \partial x_k}$ $\langle \phi_\alpha \rangle, k$	$\langle u_i \rangle, \langle \phi_\alpha \rangle$ $\tau(u_i, u_j)$ $\tau(u_i, \phi_\alpha)$ $\tau(\phi_\alpha, \phi_\beta)$

2.4 FLOWS SIMULATED

Simulations are conducted of a two-dimensional (2D) and a three-dimensional (3D) temporally developing mixing layer involving transport of a passive scalar variable. The 2D simulations are performed to establish and demonstrate the consistency of the MC solver. The 3D simulations are used to assess the overall predictive capabilities of the VSFDF methodology. These predictions are compared with data obtained by direct numerical simulation (DNS) of the same layer.

The temporal mixing layer consists of two parallel streams travelling in opposite directions with the same speed.^{64–66} In the representation below, x, y (and z) denote the streamwise, the cross-stream, (and the span-wise) directions (in 3D), respectively. The velocity components along these directions are denoted by u, v , (and w) in the x, y , (and z) directions, respectively. Both the filtered streamwise velocity and the scalar fields are initialized with a hyperbolic tangent profiles with $\langle u \rangle = 1, \langle \phi \rangle = 1$ on the top stream and $\langle u \rangle = -1, \langle \phi \rangle = 0$ on the bottom stream. The length L is specified such that $L = 2^{N_P} \lambda_u$, where N_P is the desired number of successive vortex pairings and λ_u is the wavelength of the most unstable mode corresponding to the mean streamwise velocity profile imposed at the initial time. The flow variables are normalized with respect to the half initial vorticity thickness, $L_r = \frac{\delta_v(t=0)}{2}$, ($\delta_v = \frac{\Delta U}{|\partial \langle u \rangle / \partial y|_{max}}$, where $\overline{\langle u \rangle}$ is the Reynolds-averaged value of the filtered streamwise velocity and ΔU is the velocity difference across the layer). The reference velocity is $U_r = \Delta U/2$.

All 2D simulations are conducted for $0 \leq x \leq L$, and $-\frac{2L}{3} \leq y \leq \frac{2L}{3}$. The formation of large scale structures is facilitated by introducing small harmonic, phase-shifted, disturbances containing sub-harmonics of the most unstable mode into the stream-wise and cross-stream velocity profiles. For $N_p = 1$, this results in formation of two large vortices and one subsequent pairing of these vortices. The 3D simulations are conducted for a cubic box, $0 \leq x \leq L, -\frac{L}{2} \leq y \leq \frac{L}{2}, (0 \leq z \leq L)$. The 3D field is parameterized in a procedure somewhat similar to that by Vreman et al.⁶⁷ The formation of the large scale structures are expedited through eigenfunction based initial perturbations.^{68,69} This includes

two-dimensional^{65,67,70} and three-dimensional^{65,71} perturbations with a random phase shift between the 3D modes. This results in the formation of two successive vortex pairings and strong three-dimensionality.

2.5 NUMERICAL SPECIFICATIONS

Simulations are conducted on equally-spaced grid points with grid spacings $\Delta x = \Delta y = \Delta z$ (for 3D) $= \Delta$. All 2D simulations are performed on 32×41 grid points. The 3D simulations are conducted on 193^3 and 33^3 points for DNS and LES, respectively. The Reynolds number is $Re = \frac{U_r L_r}{\nu} = 50$. To filter the DNS data, a top-hat function of the form below is used

$$G(\mathbf{x}' - \mathbf{x}) = \prod_{i=1}^3 \tilde{G}(x'_i - x_i), \quad (2.31)$$

$$\tilde{G}(x'_i - x_i) = \begin{cases} \frac{1}{\Delta_L} & |x'_i - x_i| \leq \frac{\Delta_L}{2}, \\ 0 & |x'_i - x_i| > \frac{\Delta_L}{2}. \end{cases}$$

No attempt is made to investigate the sensitivity of the results to the filter function⁵¹ or the size of the filter.⁷²

The MC particles are initially distributed throughout the computational region. All simulations are performed with a uniform “weight”⁴⁴ of the particles. Due to flow periodicity in the streamwise (and spanwise in 3D) direction(s), if the particle leaves the domain at one of these boundaries new particles are introduced at the other boundary with the same velocity and compositional values. In the cross-stream directions, the free-slip boundary condition is satisfied by the mirror-reflection of the particles leaving through these boundaries. The density of the MC particles is determined by the average number of particles N_E within the ensemble domain of size $\Delta_E \times \Delta_E (\times \Delta_E)$. The effects of both of these parameters are assessed to ensure the consistency and the statistical accuracy of the VSFDF simulations. All results are analyzed both “instantaneously” and “statistically.” In the former, the instantaneous contours (snap-shots) and scatter plots of the variables of interest are analyzed. In the latter,

the “Reynolds-averaged” statistics constructed from the instantaneous data are considered. These are constructed by spatial averaging over x (and z in 3D). All Reynolds averaged results are denoted by an overbar.

2.6 CONSISTENCY AND CONVERGENCE ASSESSMENTS

The objective of this section is to demonstrate the consistency of the VSFDF formulation and the convergence of its MC simulation procedure. For this purpose, the results via MC and LES-FD are compared against each other in VSFDF-C simulations. Since the accuracy of the FD procedure is well-established (at least for the first order filtered quantities), such a comparative assessment provides a good means of assessing the performance of the MC solution. No attempt is made to determine the appropriate values of the model constants; the values suggested in the literature are adopted⁷³ $C_0 = 2.1$, $C_\epsilon = 1$ and $C_\phi = 1$. The influence of these parameters are assessed in Section (2.7).

The uniformity of the MC particles is checked by monitoring their distributions at all times, as the particle number density must be proportional to fluid density. The Reynolds averaged density field as obtained by both LES-FD and MC are shown in Fig. 2. Close to unity values for the density at all times is the first measure of the accuracy of simulations. Figures 3, 4 show the instantaneous contour plots of the filtered scalar and vorticity fields at several times. These figures provide a visual demonstration of the consistency of the VSFDF. This consistency is observed for all first order moments without any statistical variability. Also, all of these moments show very little dependence on the values of Δ_E and N_E consistent with previous FDF simulations.⁹⁻¹¹ In the presentation below we only focus on second order moments. Specifically, the scalar-velocity correlations are shown since all other second order SGS moments behave similarly.

Figures 5, 6 show the statistical variability of the results for simulations with $N_E = 40$. It is observed that these moments exhibit spreads with variances decreasing as the size of the ensemble domain is reduced. Figures 7-10 show the sensitivity to N_E and Δ_E . All these results clearly display convergence suggested by Eq. (2.30). As the ensemble domain size

decreases, the VSFDF results converge to those of LES-FD. Ideally, the LES-FD results should become independent of the MC results, as the latter become more reliable, *i.e.* when $N_E \rightarrow \infty$, $\Delta_E \rightarrow 0$). It is observed that best match is achieved with $\Delta_E \leq \Delta/2$ and $N_E \geq 40$. This conclusion is consistent with previous assessment studies on the scalar FDF,^{9,10} and the velocity FDF.¹¹ All the subsequent simulations are conducted with $\Delta_E = \Delta/2$ and $N_E = 40$.

2.7 COMPARATIVE ASSESSMENTS OF THE VSFDF

The objective of this section is to analyze some of the characteristics of the VSFDF via comparative assessments against DNS data. In addition, comparisons are also made with LES via the “conventional” Smagorinsky^{42,74} model

$$\begin{aligned}
\tau_L(u_i, u_j) - \frac{2}{3} k \delta_{ij} &= -2 \nu_t S_{ij}, \\
\tau_L(u_i, \phi) &= -\Gamma_t \frac{\partial \langle \phi \rangle}{\partial x_i}, \\
S_{ij} &= \frac{1}{2} \left(\frac{\partial \langle u_i \rangle}{\partial x_j} + \frac{\partial \langle u_j \rangle}{\partial x_i} \right), \\
\nu_t &= C_\nu \Delta_L^2 S, \quad \Gamma_t = \frac{\nu_t}{Sc_t}.
\end{aligned} \tag{2.32}$$

$C_\nu = 0.04$, $Sc_t = 1$, $S = \sqrt{S_{ij} S_{ij}}$ and Δ_L is the characteristic length of the filter. This model considers the anisotropic part of the SGS stress tensor $a_{ij} = \tau_L(u_i, u_j) - 2/3 k \delta_{ij}$. The isotropic components are absorbed in the pressure field.

For comparison, the DNS data are transposed from the original high resolution 193^3 points to the coarse 33^3 points. In the comparisons, we also consider the “resolved” and the “total” components of the Reynolds averaged moments. The former are denoted by $\overline{R(a, b)}$ with $R(a, b) = \left(\langle a \rangle - \overline{\langle a \rangle} \right) \left(\langle b \rangle - \overline{\langle b \rangle} \right)$; and the latter is $\overline{r(a, b)}$ with $r(a, b) = (a - \bar{a}) (b - \bar{b})$. In DNS, the “total” SGS components are directly available, while in LES they are approximated by $\overline{r(a, b)} \approx \overline{R(a, b)} + \overline{\tau(a, b)}$.⁶⁷ Unless indicated otherwise, the values of the model

constants are $C_0 = 2.1$, $C_\epsilon = 1$, $C_\phi = 1$; but the effects of these parameters on the predicted results are assessed.

Figure 11 shows the iso-surface of the instantaneous filtered passive scalar fields at $t = 80$. By this time, the flow has gone through pairings and exhibits strong 3D effects. This is evident by the formation of large scale span-wise rollers with presence of mushroom like structures in streamwise planes.⁶⁸ Similar to previous results,¹¹ the amount of SGS diffusion with the Smagorinsky model is significant. Thus, the predicted results are overly smooth. The Reynolds averaged values of the filtered scalar field at $t = 80$ are shown in Fig. 12, and the temporal variation of the “scalar thickness,”

$$\delta_s(t) = |y(\overline{\langle\phi\rangle} = 0.9)| + |y(\overline{\langle\phi\rangle} = 0.1)|, \quad (2.33)$$

is shown in Fig. 13. The filtered and unfiltered DNS data yield virtually indistinguishable results. The dissipative nature of the Smagorinsky model at initial times resulting in a slow growth of the layer is shown. All VSFDF predictions compare well with DNS data in predicting the spread of the layer.

Several components of the planar averaged values of the second order SGS moments are compared with DNS data in Figs. 14, 15 for several values of the model constants. In general, the VSFDF results are in better agreement with DNS data than those predicted by the Smagorinsky model. In this regard, therefore, the VSFDF is expected to be more effective than the Smagorinsky type closures for LES of reacting flows since the extent of SGS mixing is heavily influenced by these SGS moments.^{5,75} However, it is not possible to suggest “optimum” values for the model constants, except that at small C_ϵ and C_ϕ values, the SGS energy is very large.

Several components of the resolved second order moments are presented in Figs. 16, 17. As expected, the performance of the Smagorinsky model is not very good as it does not predict the spread and the peak value accurately. The VSFDF yields reasonable predictions except for small C_ϕ values. However, the total values of these moments are fairly independent of the model constants and yield very good agreement with DNS data as shown in Figs. 18, 19. It is also noted that while the SGS moments and/or the resolved moments may be over- and/or under-estimated depending on the values of the model coefficients, the total values

of the moments are fairly independent of these coefficients, at least in the range of values as considered. But low values of C_ϕ, C_ϵ are not recommended as they would result into too much SGS energy in comparison to the resolved energy.

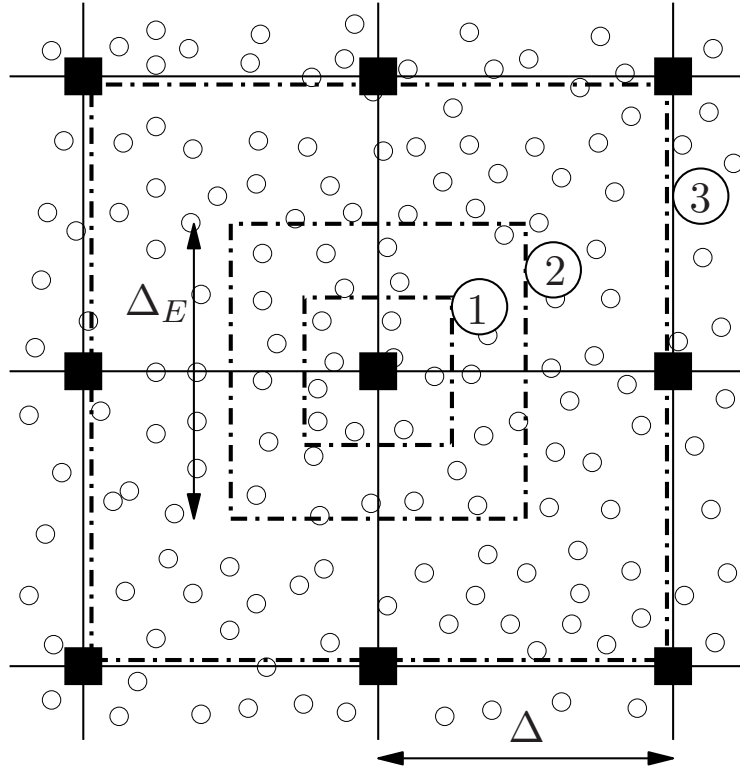


Figure 1: Concept of ensemble-averaging. Shown are three different ensemble domains: $1(\Delta_E = \Delta/2, N_E \approx 10)$, $2(\Delta_E = \Delta, N_E \approx 40)$, $3(\Delta_E = 2\Delta, N_E \approx 160)$. Black squares denote the finite-difference grid points, and the circles denote the MC particles.

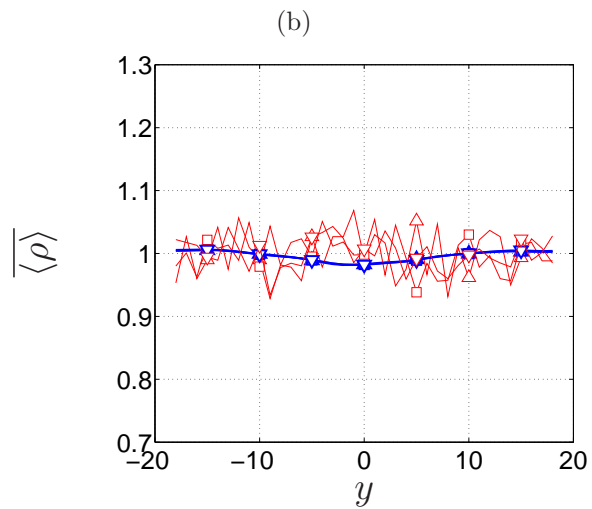
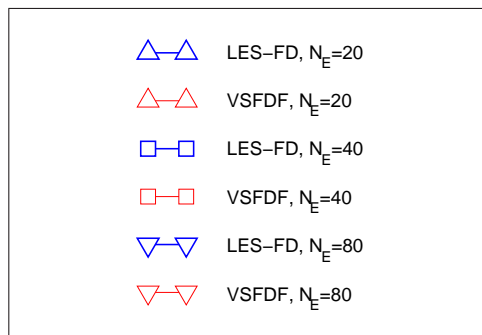
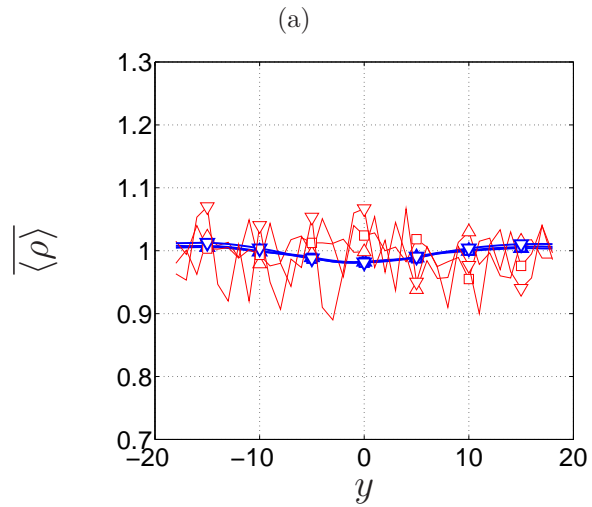
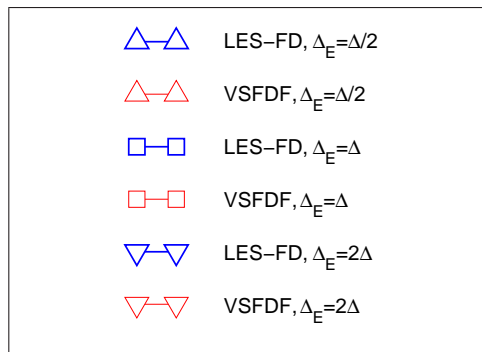


Figure 2: Cross-stream variations of the Reynolds-averaged values of $\langle \rho \rangle$ at $t=34.3$: (a) $N_E = 40$, (b) $\Delta_E = \Delta/2$.

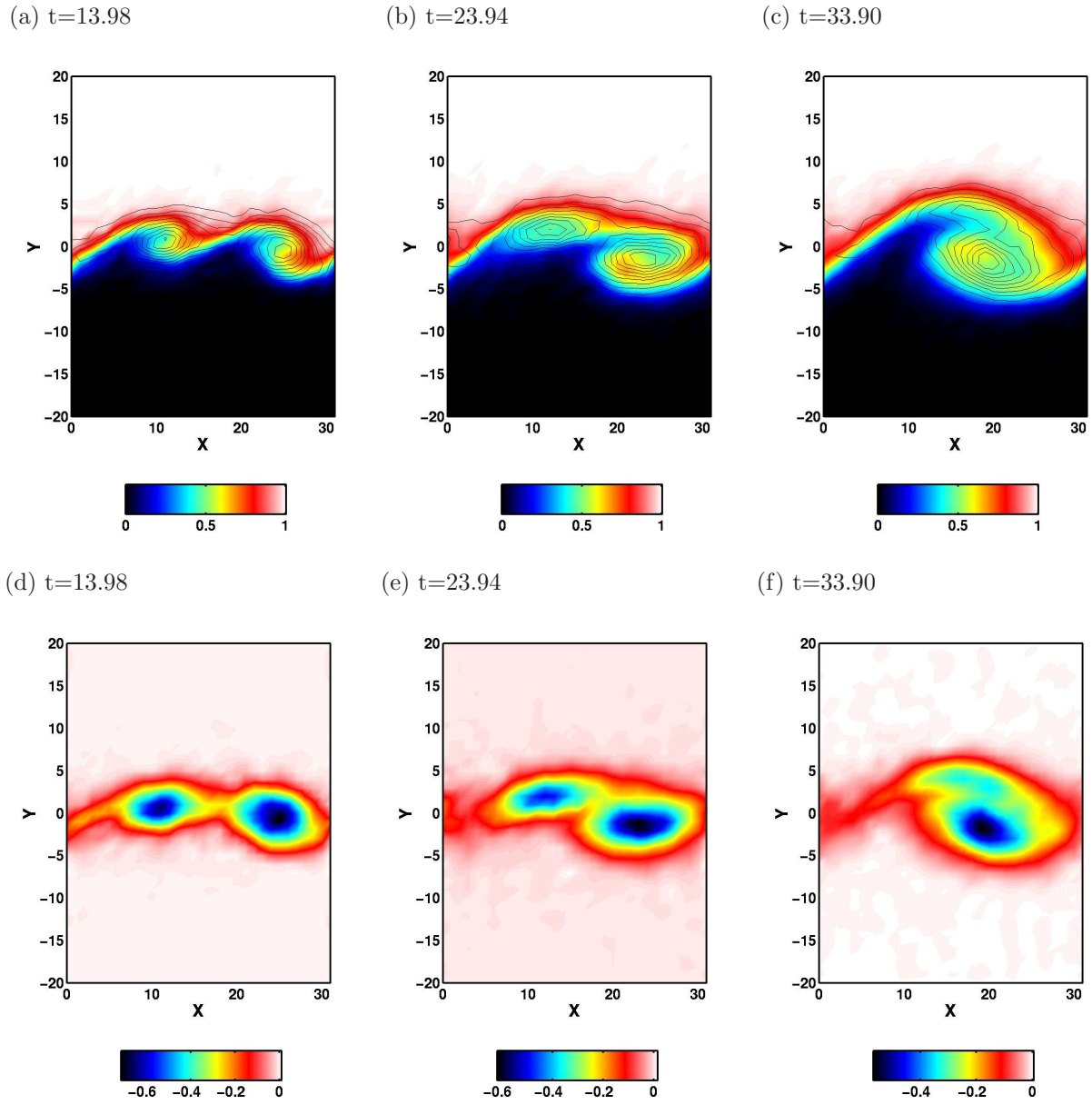


Figure 3: Temporal evolution of the scalar (with superimposed vorticity iso-lines) (top) and the vorticity (bottom) fields for LES-FD, with $\Delta_E = \Delta/2$ and $N_E = 40$ at several times.

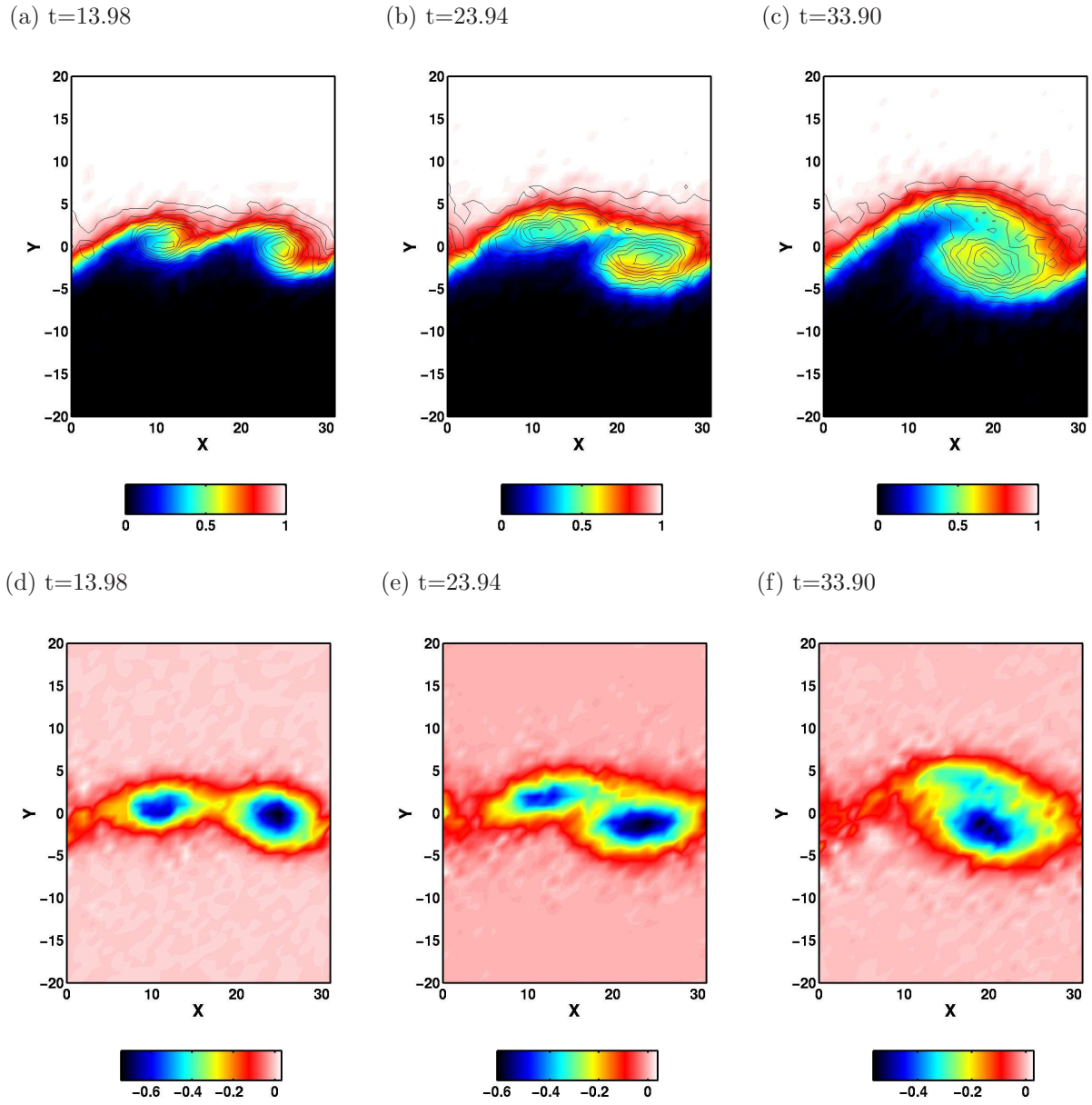


Figure 4: Temporal evolution of the scalar (with superimposed vorticity iso-lines) (top) and the vorticity (bottom) fields for VSFDF with $\Delta_E = \Delta/2$ and $N_E = 40$ at several times.

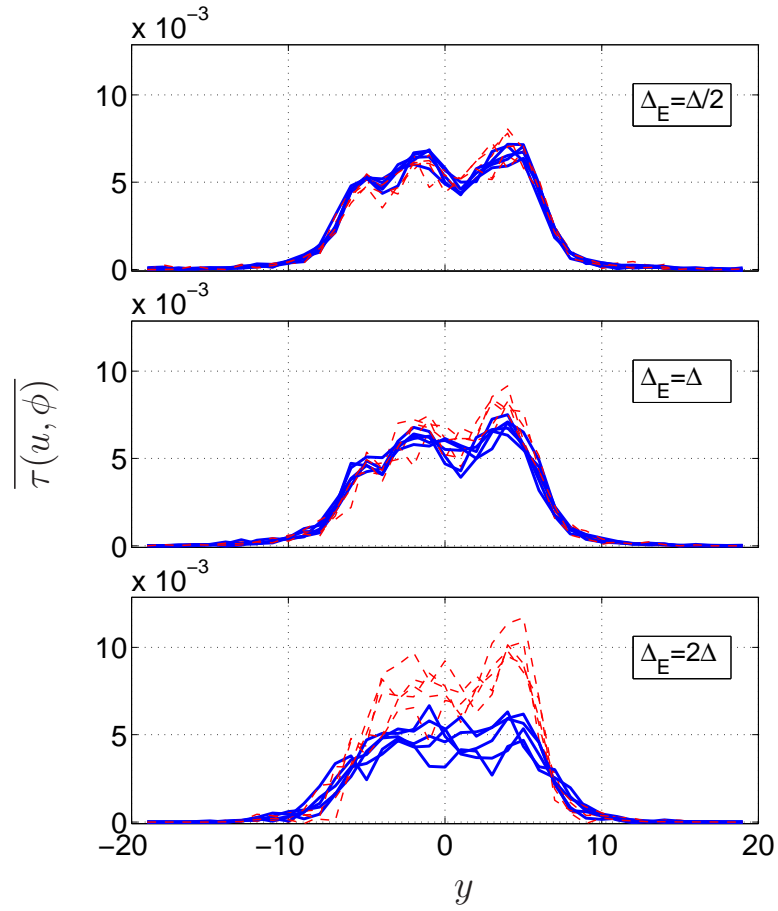


Figure 5: Statistical variability of LES-FD and VSFDF-C simulations with $N_E = 40$ for Reynolds-averaged values of $\tau(u, \phi)$ at $t=34.4$. Solid lines: LES-FD, dashed lines: VSFDF-C.

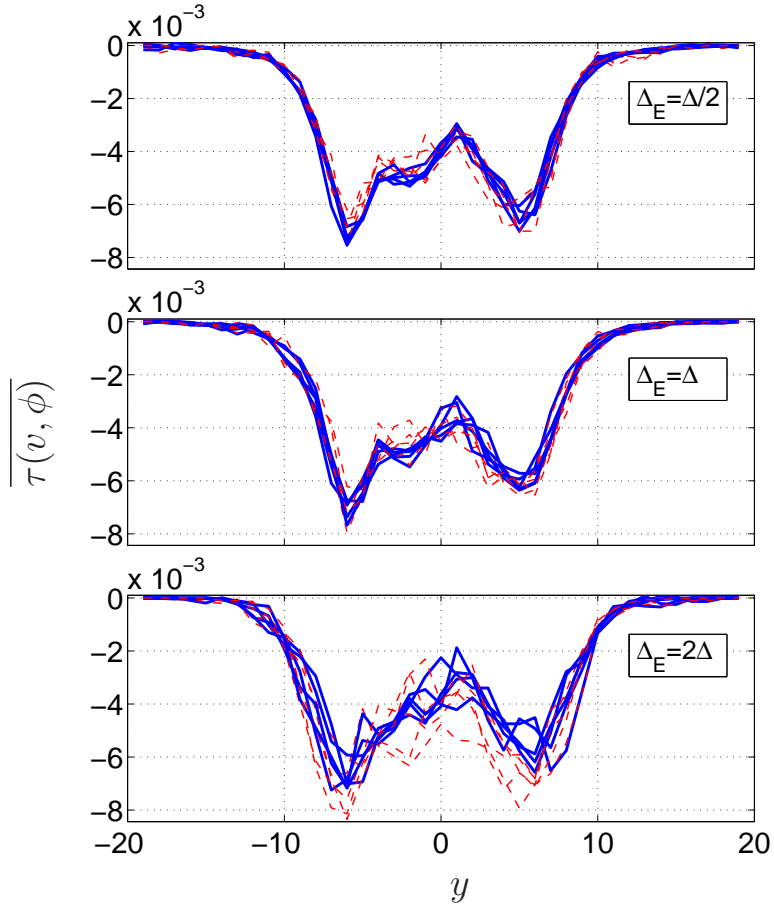


Figure 6: Statistical variability of LES-FD and VSFDF-C simulations with $N_E = 40$ for Reynolds-averaged values of $\tau(v, \phi)$ at $t=34.4$. Solid lines: LES-FD, dashed lines: VSFDF-C.

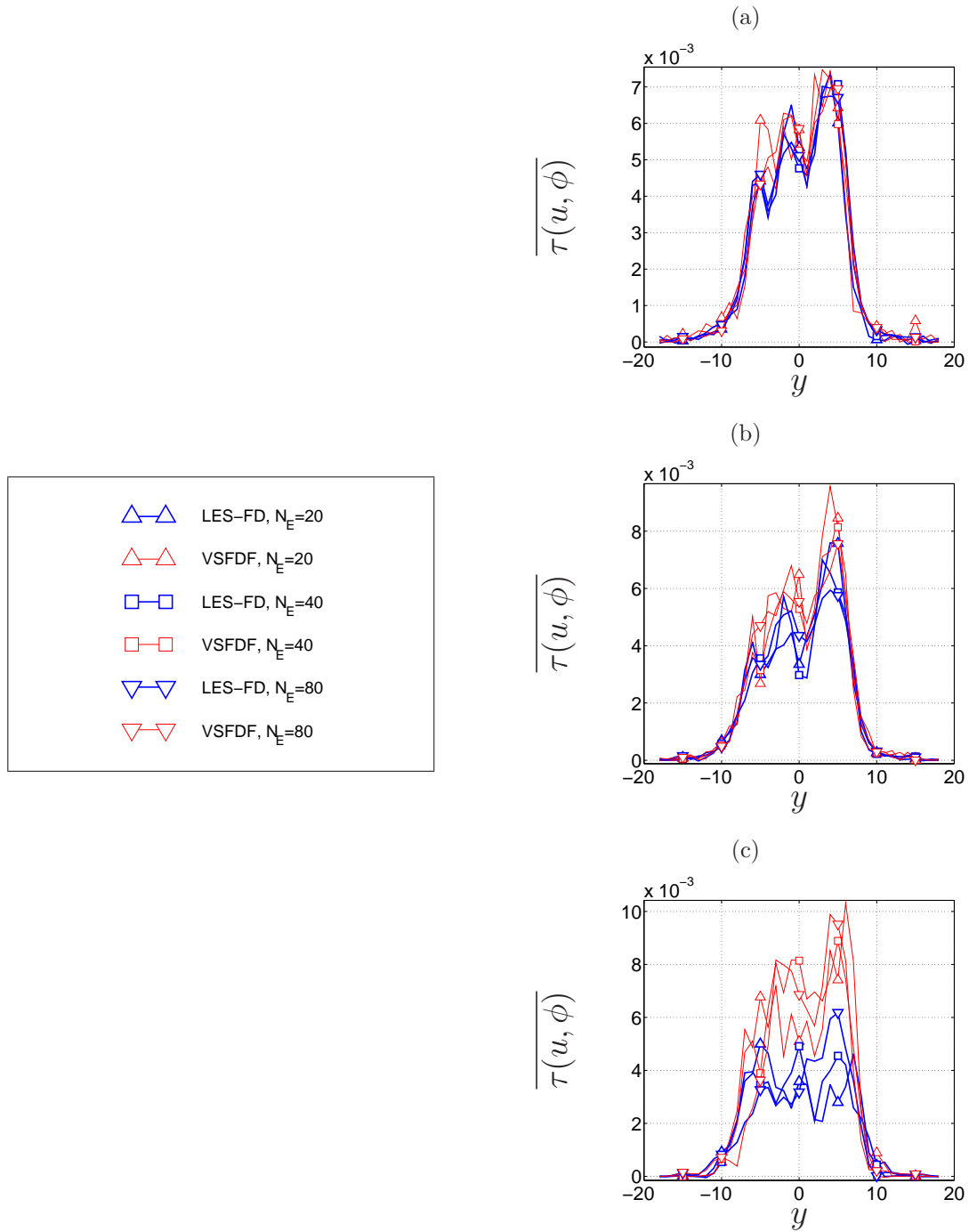


Figure 7: Cross-stream variations of the Reynolds-averaged values of $\tau(u, \phi)$ (a) $\Delta_E = \Delta/2$, (b) $\Delta_E = \Delta$, (c) $\Delta_E = 2\Delta$.

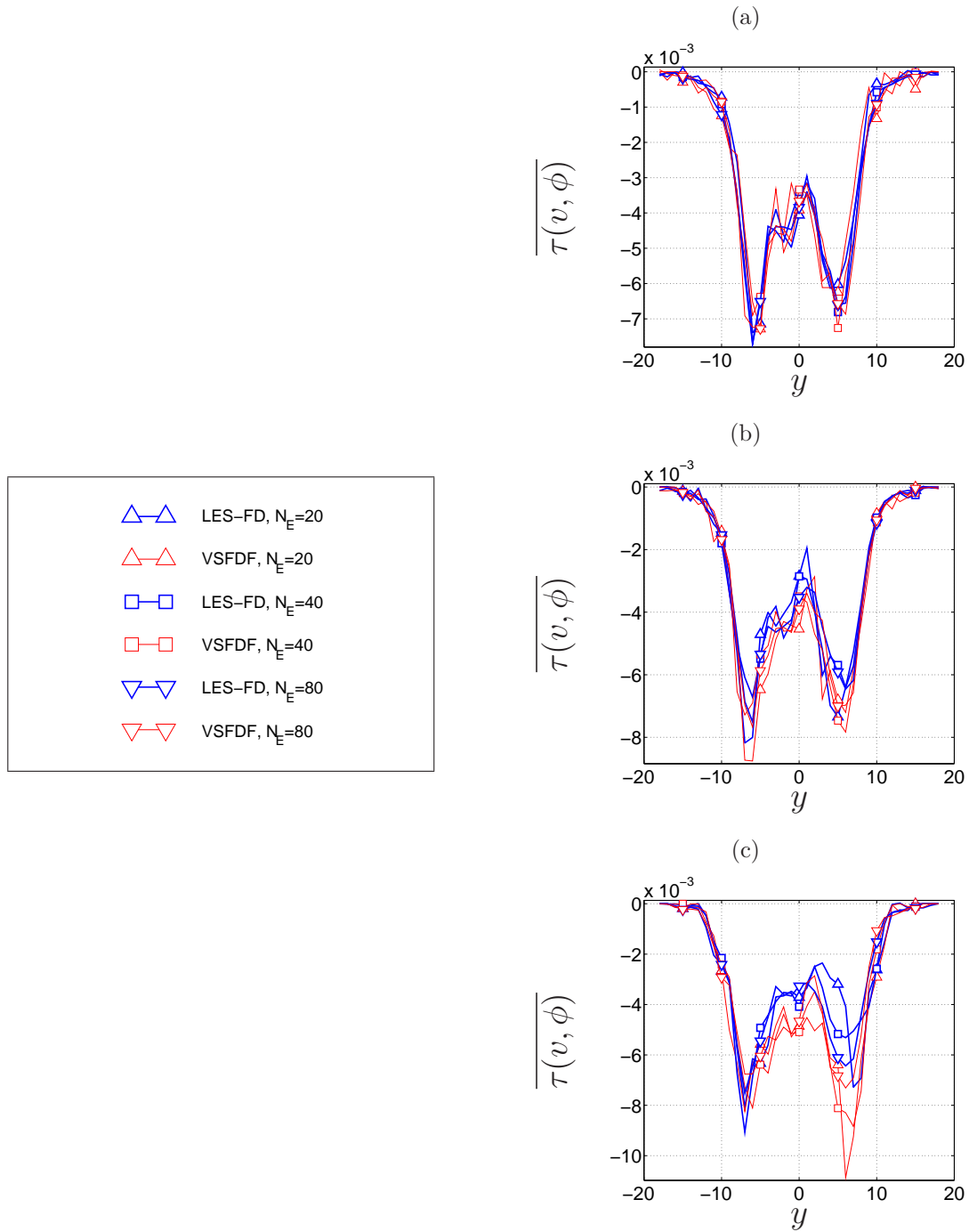


Figure 8: Cross-stream variations of the Reynolds-averaged values of $\tau(v, \phi)$ (a) $\Delta_E = \Delta/2$, (b) $\Delta_E = \Delta$, (c) $\Delta_E = 2\Delta$.

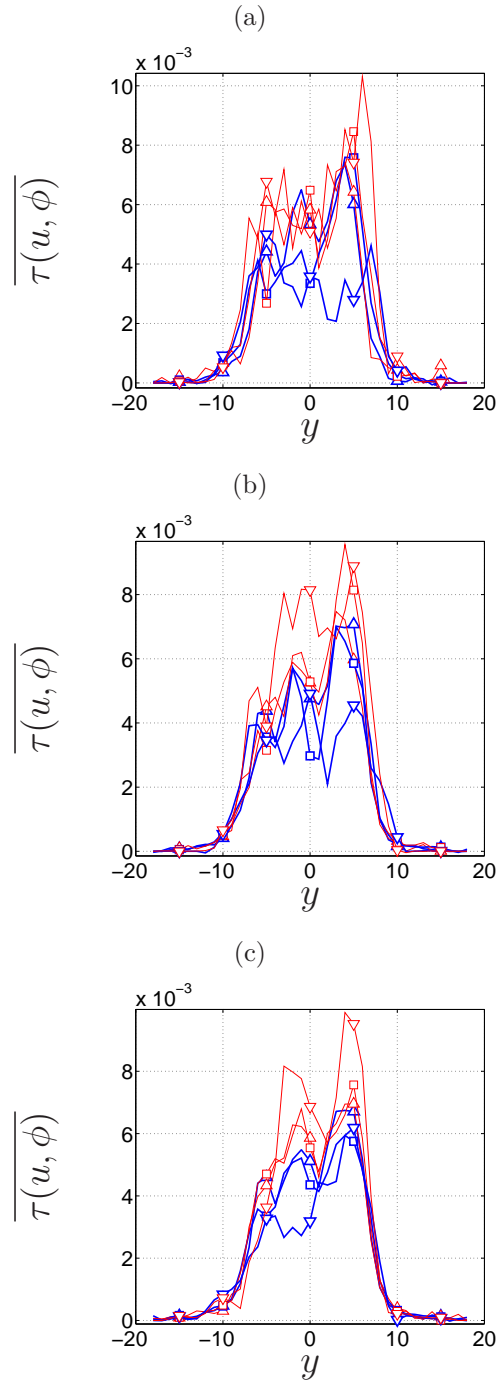
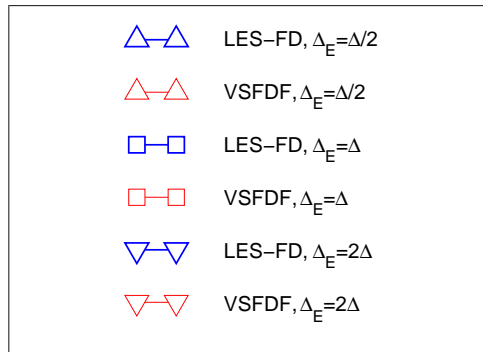


Figure 9: Cross-stream variations of the Reynolds-averaged values of $\tau(u, \phi)$ (a) $N_E = 20$, (b) $N_E = 40$, (c) $N_E = 80$.

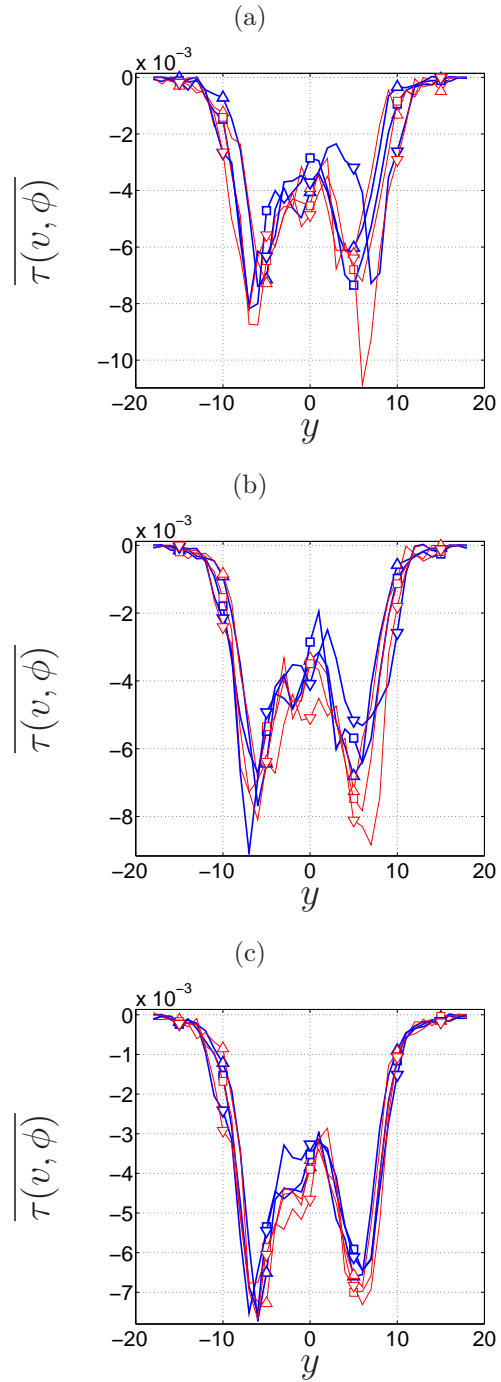
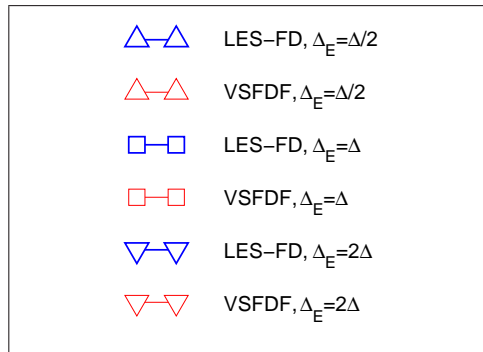


Figure 10: Cross-stream variations of the Reynolds-averaged values of $\tau(v, \phi)$ (a) $N_E = 20$, (b) $N_E = 40$, (c) $N_E = 80$.

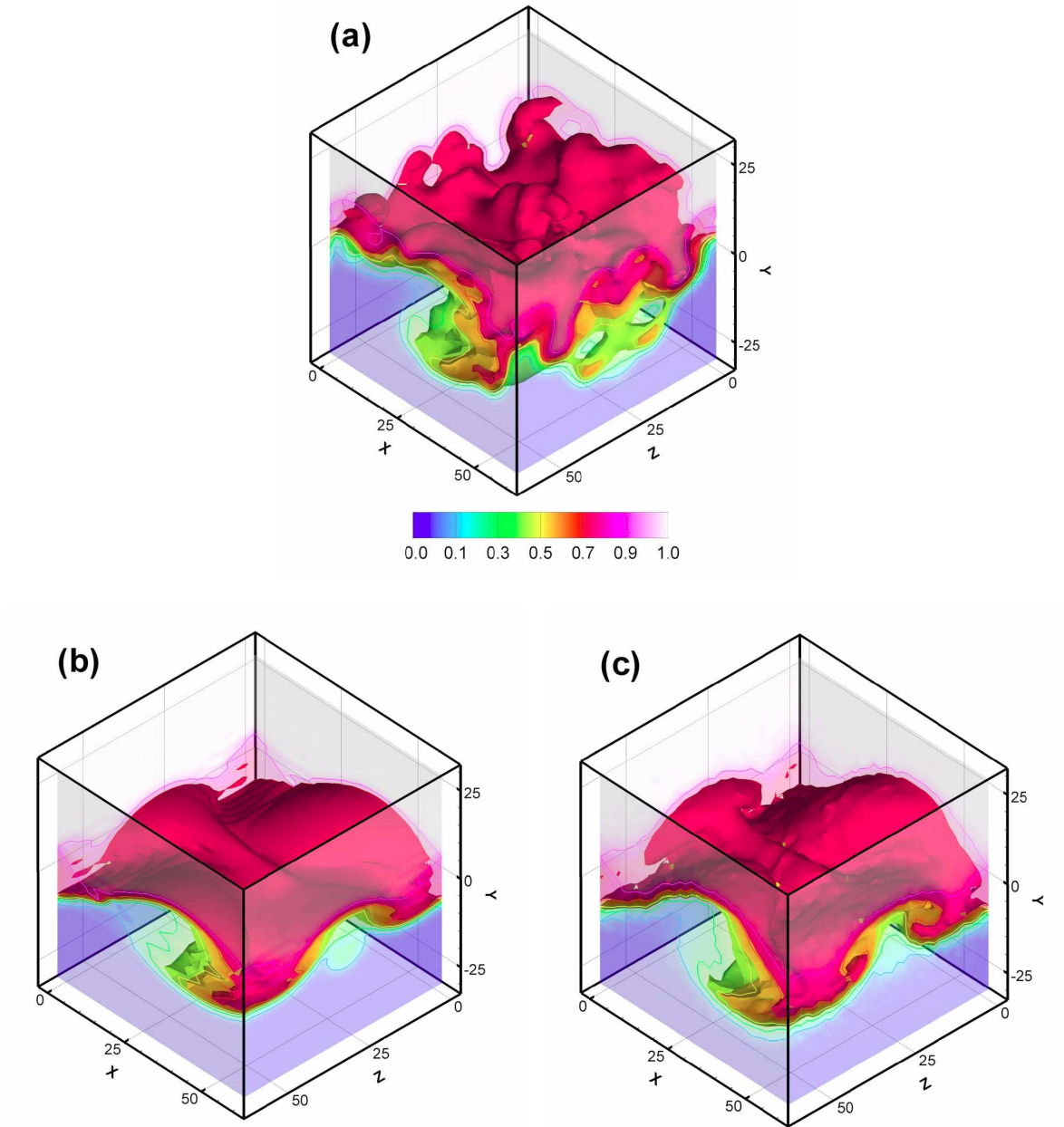


Figure 11: Contour surfaces of the $\langle \phi \rangle$ field in the 3D mixing layer at $t = 80$ as obtained by: (a) DNS, (b) Smagorinsky, (c) VSFDF.

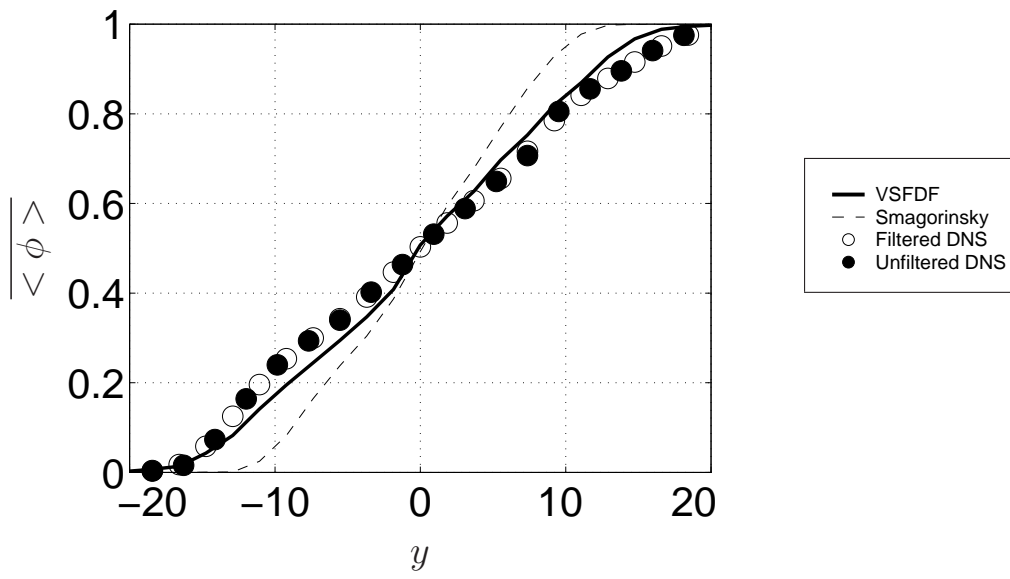


Figure 12: Cross-stream variations of the Reynolds-averaged values of the filtered scalar field at $t = 80$.

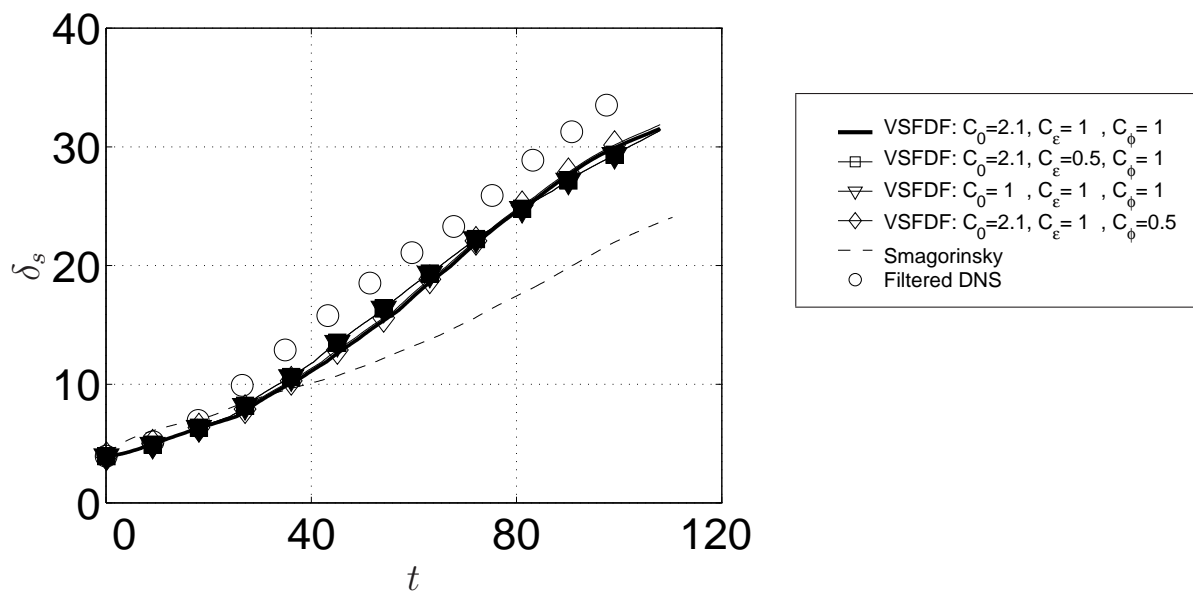


Figure 13: Temporal variations of the scalar thickness.

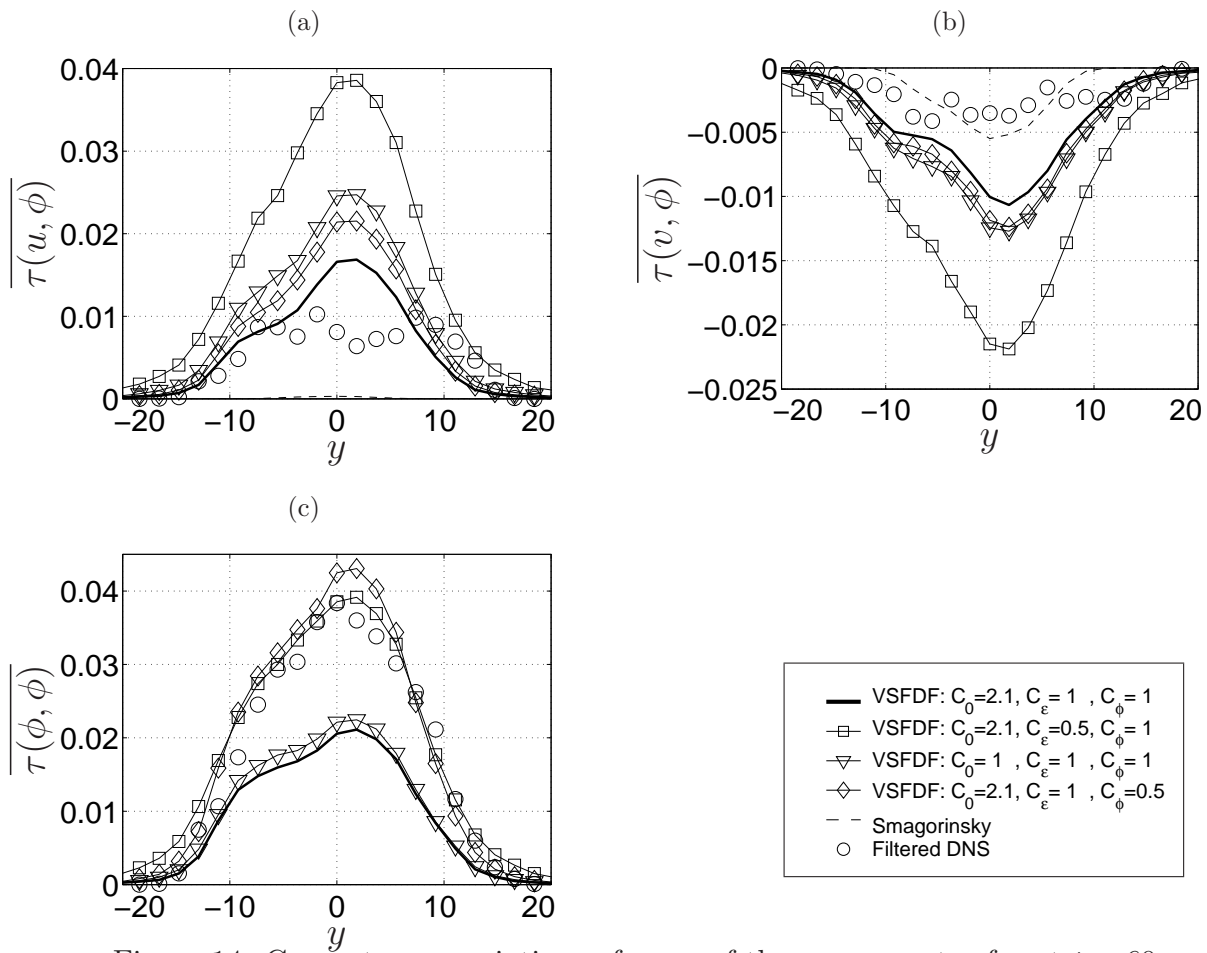


Figure 14: Cross stream variations of some of the components of τ at $t = 60$.

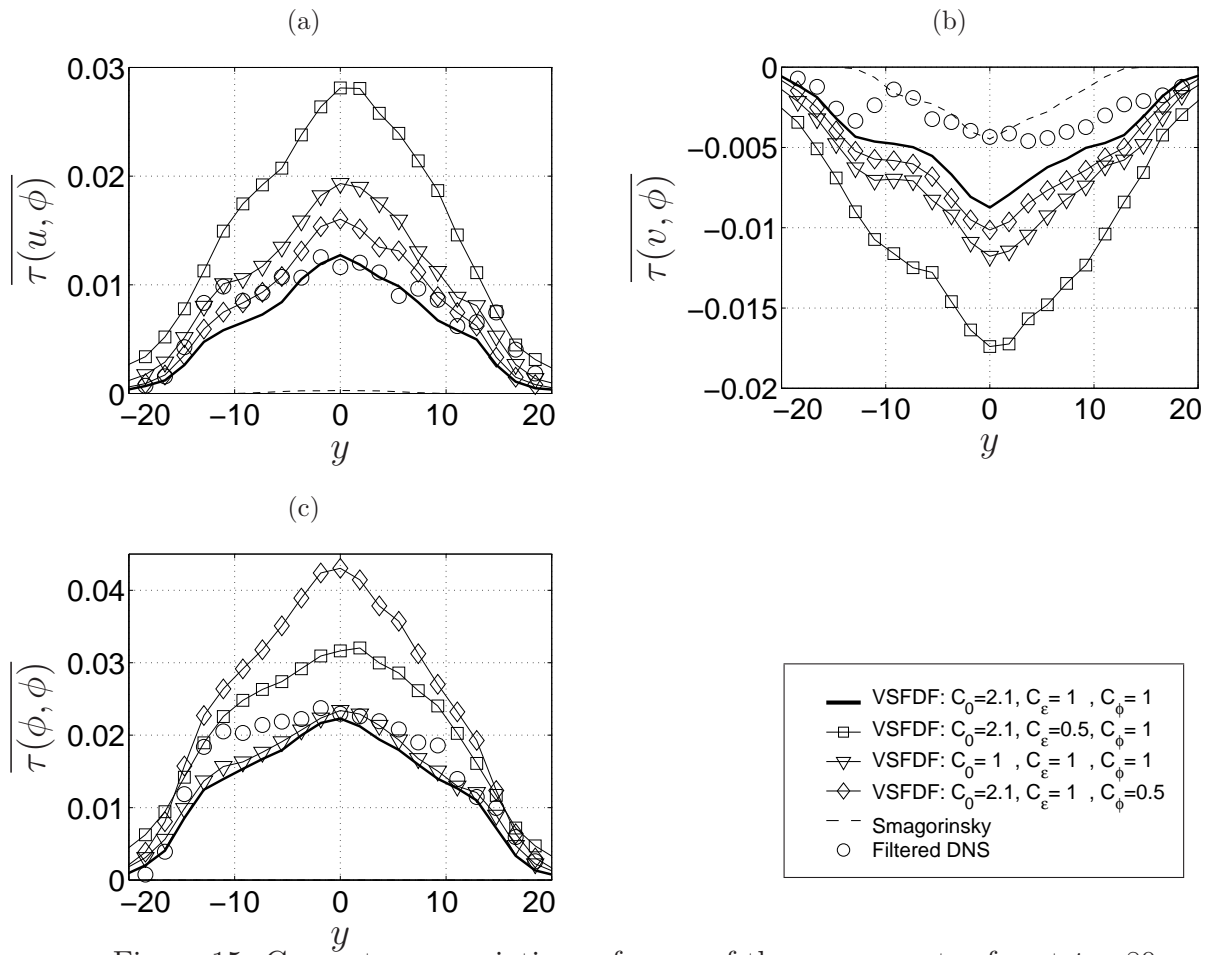


Figure 15: Cross stream variations of some of the components of τ at $t = 80$.

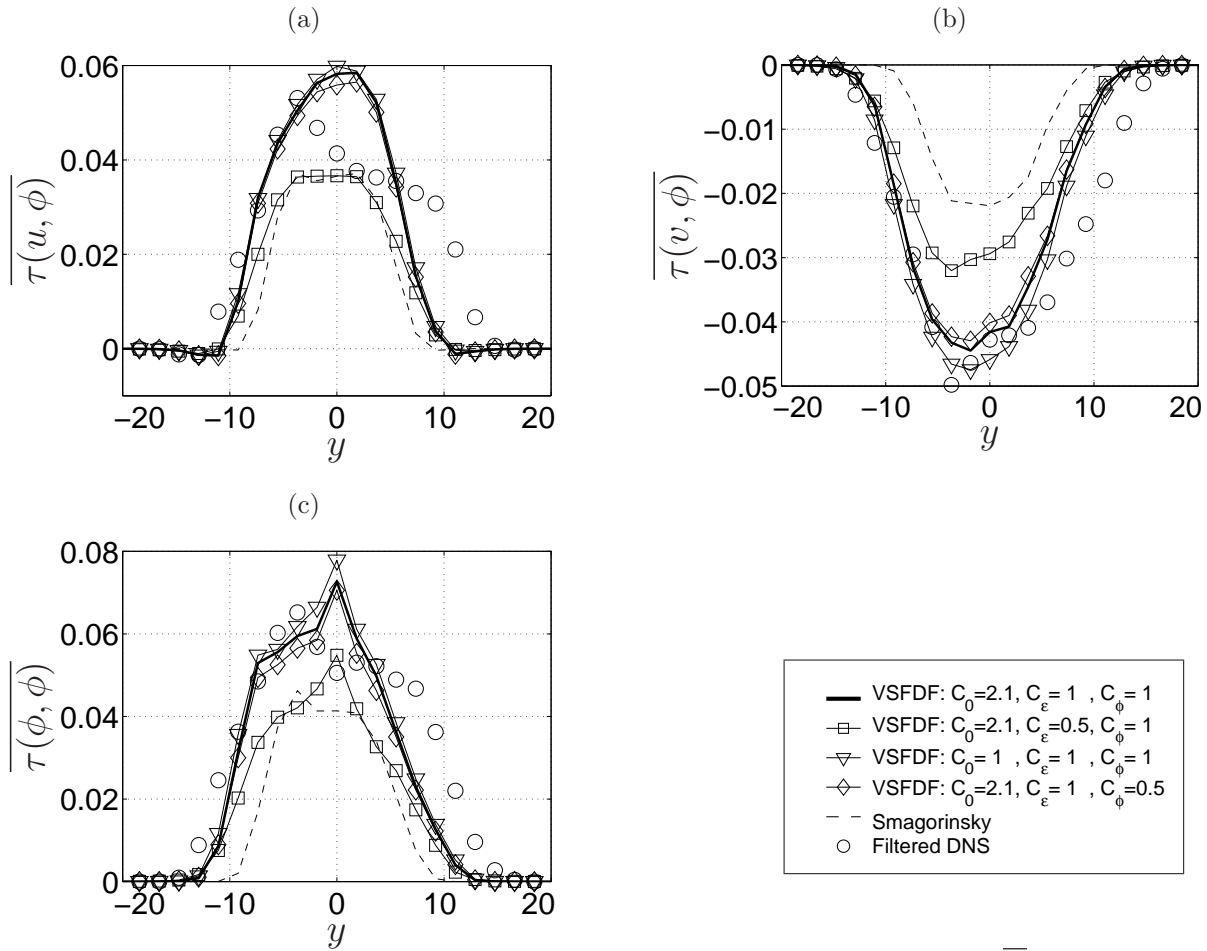


Figure 16: Cross-stream variations of some of the components of \bar{R} at $t = 60$.

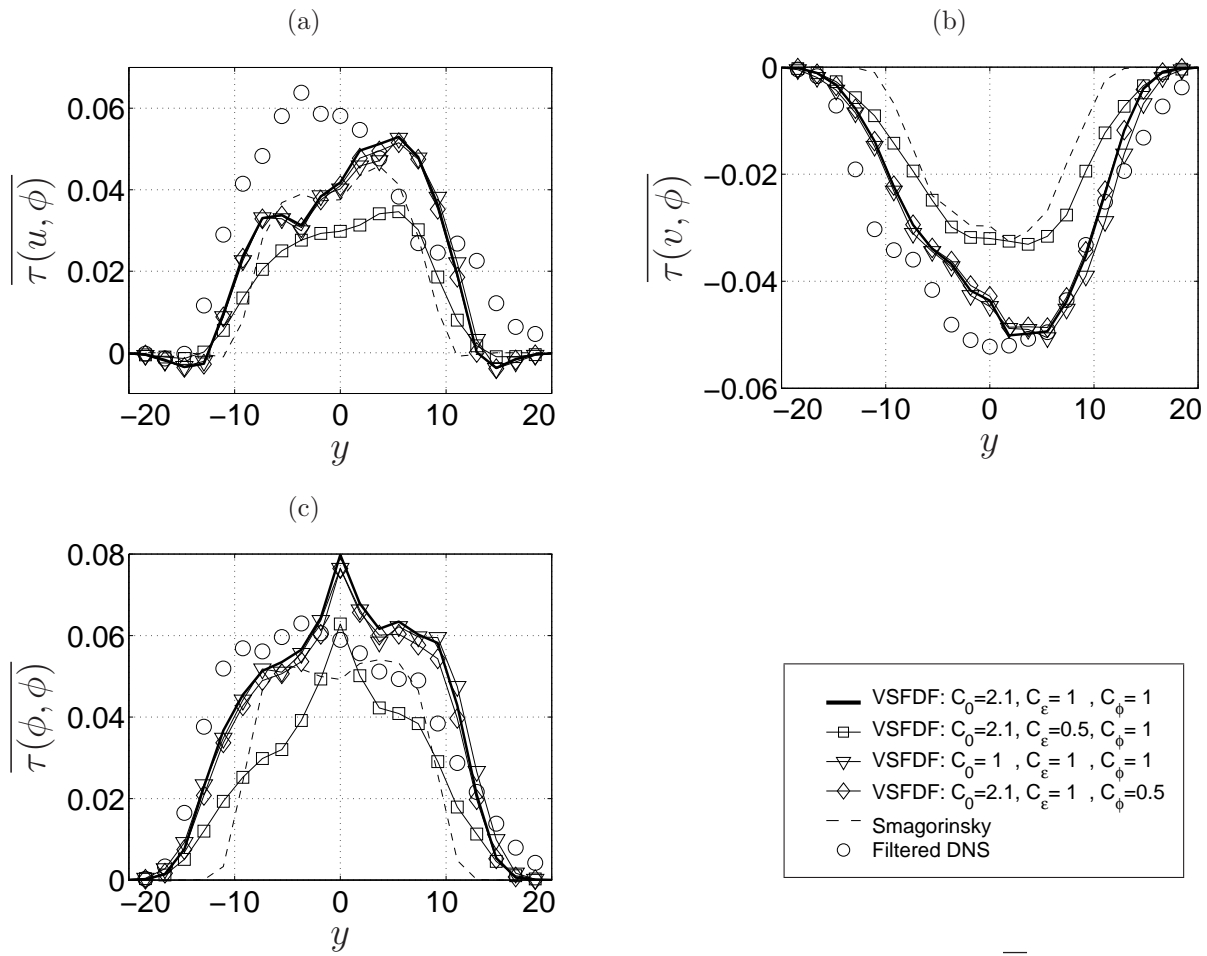


Figure 17: Cross-stream variations of some of the components of \bar{R} at $t = 80$.

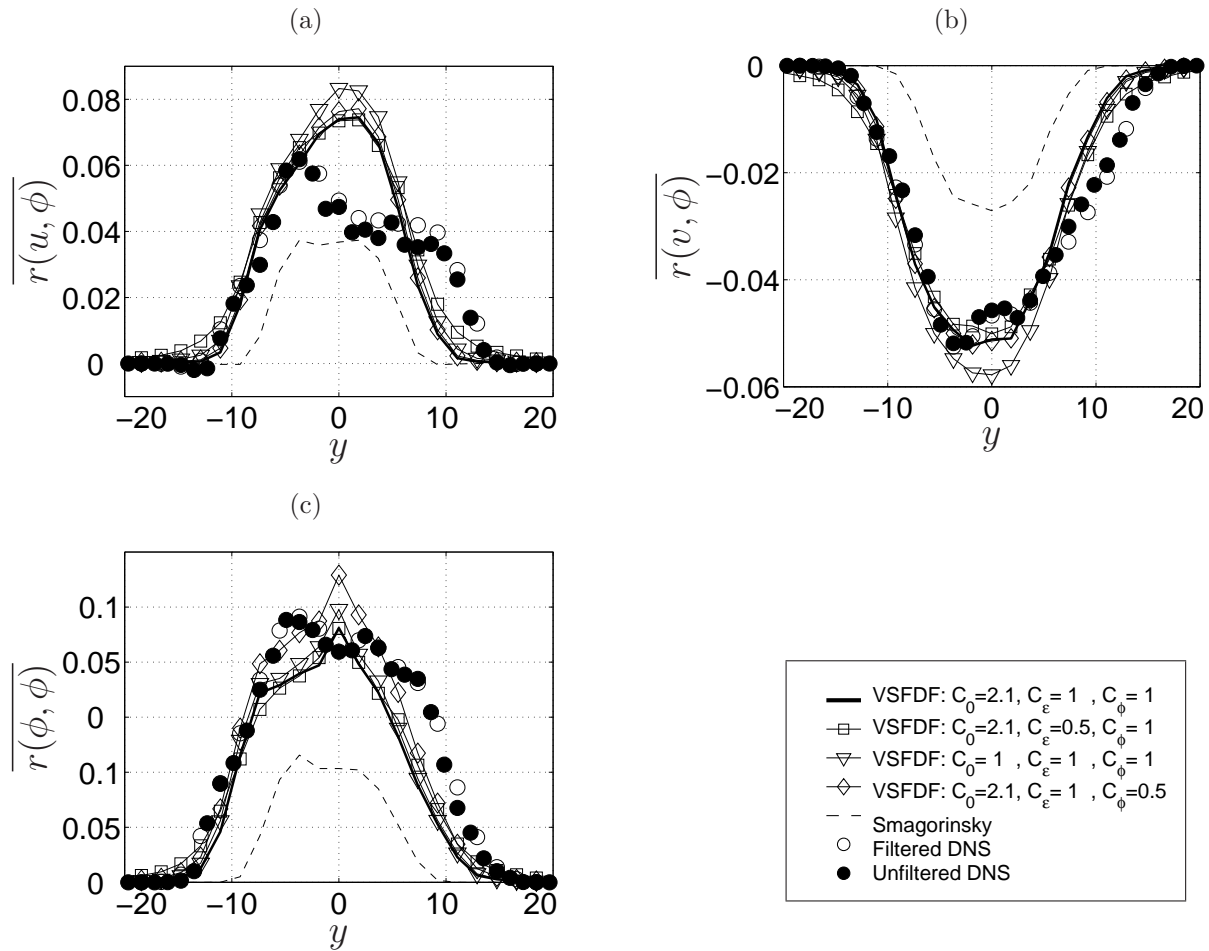


Figure 18: Cross-stream variations of some of the components of \bar{r} at $t = 60$.

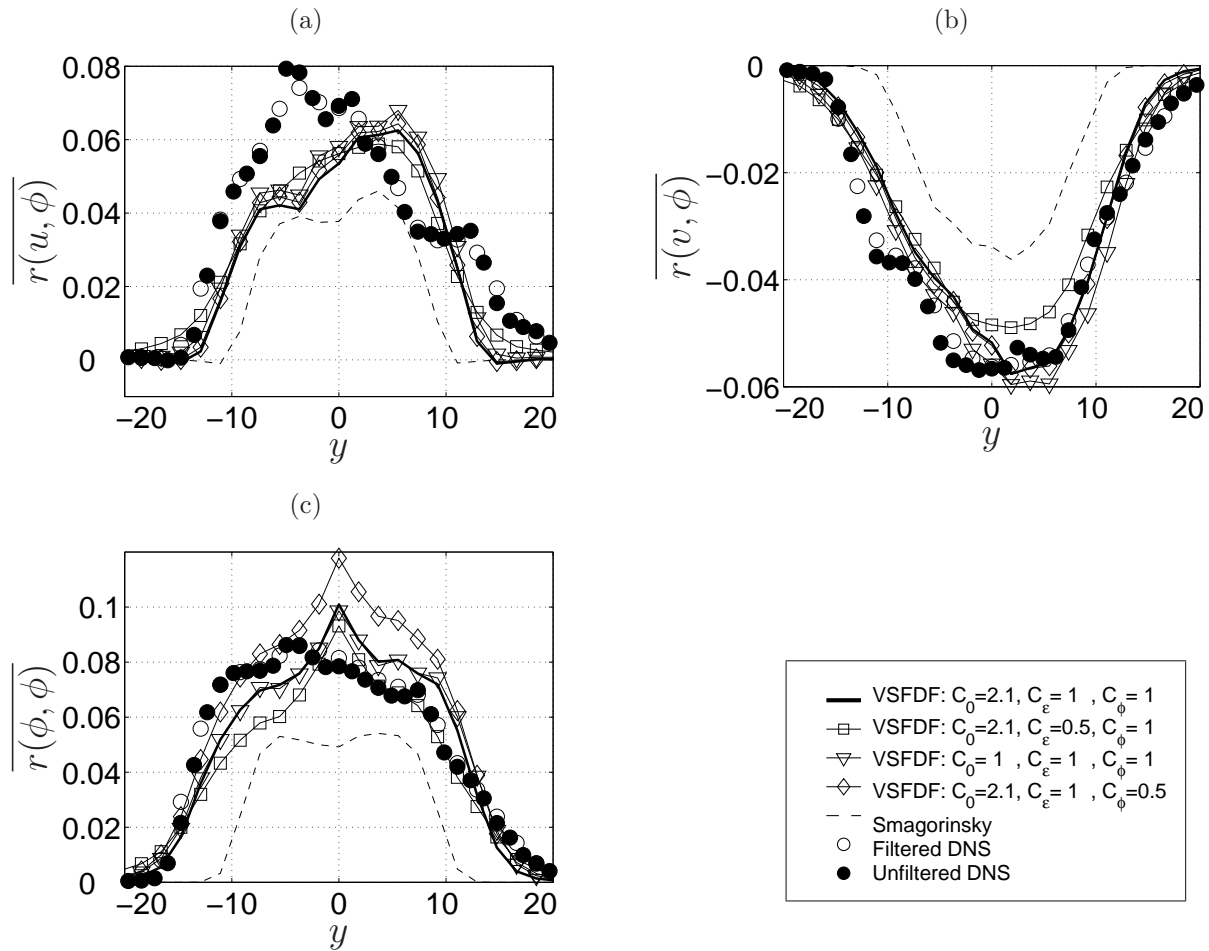


Figure 19: Cross-stream variations of some of the components of \bar{r} at $t = 80$.

3.0 JOINT VELOCITY SCALAR FILTERED MASS DENSITY FUNCTION FOR VARIABLE-DENSITY FLOWS

In this chapter, the VSFDF methodology is extended for variable-density turbulent reacting flows, by considering the joint “velocity-scalar filtered mass density function” (VSFMDF). Following its mathematical definition, an exact transport equation is derived for the VSFMDF. This equation is modeled in a probabilistic manner. Two models, in the form of systems of stochastic differential equations are considered, each containing different forms of the fluid density. The procedure for numerical solution of the VSFMDF is based on a hybrid Eulerian/Lagrangian procedure. The Eulerian part involves finite-difference solution of the transport equations. The Lagrangian part involves Monte Carlo solution of the modeled VSFMDF transport equation. The unclosed moments in the Eulerian part are obtained from the Monte Carlo solver. The consistency and accuracy of this procedure are established in the simulation of a three-dimensional mixing layer involving the transport of a passive scalar. These simulations are assessed by comparing the VSFMDF results with those of direct numerical simulation (DNS), and those predicted by a conventional LES via the Smagorinsky⁴² SGS closure. In addition, the predictive capabilities of VSFMDF is demonstrated by LES of a reacting shear layer. The predicted results are compared with experimental data.⁷⁶

3.1 FORMULATION

In a compressible flow undergoing chemical reaction involving N_s species, the primary transport variables are the density $\rho(\mathbf{x}, t)$, the velocity vector $u_i(\mathbf{x}, t)$ ($i = 1, 2, 3$), the pressure $p(\mathbf{x}, t)$, the total specific enthalpy $h(\mathbf{x}, t)$ and the species’ mass fractions $Y_\alpha(\mathbf{x}, t)$

($\alpha = 1, 2, \dots, N_s$). The equations which govern the transport of these variables in space (x_i) ($i = 1, 2, 3$) and time (t) are the continuity, momentum, enthalpy (energy) and species' mass fraction equations, along with an equation of state

$$\frac{\partial \rho}{\partial t} + \frac{\partial \rho u_j}{\partial x_j} = 0, \quad (3.1a)$$

$$\frac{\partial \rho u_i}{\partial t} + \frac{\partial \rho u_j u_i}{\partial x_j} = -\frac{\partial p}{\partial x_i} + \frac{\partial \tau_{ji}}{\partial x_j}, \quad (3.1b)$$

$$\frac{\partial \rho \phi_\alpha}{\partial t} + \frac{\partial \rho u_j \phi_\alpha}{\partial x_j} = -\frac{\partial J_j^\alpha}{\partial x_j} + \rho S_\alpha, \quad \alpha = 1, 2, \dots, \sigma = N_s + 1, \quad (3.1c)$$

$$p = \rho R^0 T \sum_{\alpha=1}^{N_s} Y_\alpha / M_\alpha = \rho R T, \quad (3.1d)$$

where R^0 and R are the universal and mixture gas constants and M_α denotes the molecular weight of species α . The chemical reaction source terms $S_\alpha \equiv \hat{S}_\alpha(\boldsymbol{\phi}(\mathbf{x}, t))$ are functions of compositional scalars ($\boldsymbol{\phi} \equiv [\phi_1, \phi_2, \dots, \phi_{N_s+1}]$). Equation (3.1c) represents the transport of species' mass fraction and enthalpy in a common form with

$$\phi_\alpha \equiv Y_\alpha, \quad \alpha = 1, 2, \dots, N_s, \quad \phi_\sigma \equiv h = \sum_{\alpha=1}^{N_s} h_\alpha \phi_\alpha, \quad (3.2)$$

and

$$h_\alpha = h_\alpha^0 + \int_{T_0}^T c_{p_\alpha}(T') dT'. \quad (3.3)$$

Here T and T_0 denote the temperature field and the reference temperature, respectively. In this equation, h_α^0 and c_{p_α} denote the absolute enthalpy at T_0 and the specific heat at constant pressure for species α . For a Newtonian fluid, with Fick's law of diffusion, the viscous stress tensor τ_{ij} and the scalar flux J_j^α are represented by

$$\tau_{ij} = \mu \left(\frac{\partial u_i}{\partial x_j} + \frac{\partial u_j}{\partial x_i} - \frac{2}{3} \frac{\partial u_k}{\partial x_k} \delta_{ij} \right), \quad (3.4a)$$

$$J_j^\alpha = -\gamma \frac{\partial \phi_\alpha}{\partial x_j}, \quad (3.4b)$$

where μ is the fluid dynamic viscosity and $\gamma = \rho \Gamma$ denote the thermal and mass molecular diffusivity coefficients for all the scalars. We assume a constant value for $\mu = \gamma$; *i.e.* unity Schmidt(Sc) and Lewis (Le) numbers. In reactive flows, molecular processes are much more complicated than portrayed by Eq. (3.4). Since the molecular diffusion is typically less

important than that of SGS, this simple model is adopted with justifications and caveats given in Refs. [43–45](#)

Large eddy simulation involves the spatial filtering operation [1,46–49](#)

$$\langle f(\mathbf{x}, t) \rangle_l = \int_{-\infty}^{+\infty} f(\mathbf{x}', t) G(\mathbf{x}', \mathbf{x}) d\mathbf{x}', \quad (3.5)$$

where $G(\mathbf{x}', \mathbf{x})$ denotes a filter function, and $\langle f(\mathbf{x}, t) \rangle_l$ is the filtered value of the transport variable $f(\mathbf{x}, t)$. In variable-density flows it is convenient to use the Favre-filtered quantity $\langle f(\mathbf{x}, t) \rangle_L = \langle \rho f \rangle_l / \langle \rho \rangle_l$. We consider a filter function that is spatially and temporally invariant and localized, thus: $G(\mathbf{x}', \mathbf{x}) \equiv G(\mathbf{x}' - \mathbf{x})$ with the properties $G(\mathbf{x}) \geq 0$, $\int_{-\infty}^{+\infty} G(\mathbf{x}) d\mathbf{x} = 1$. Applying the filtering operation to Eqs. [\(3.1\)](#) yields

$$\frac{\partial \langle \rho \rangle_l}{\partial t} + \frac{\partial \langle \rho \rangle_l \langle u_j \rangle_L}{\partial x_j} = 0, \quad (3.6a)$$

$$\begin{aligned} \frac{\partial \langle \rho \rangle_l \langle u_i \rangle_L}{\partial t} + \frac{\partial \langle \rho \rangle_l \langle u_j \rangle_L \langle u_i \rangle_L}{\partial x_j} &= -\frac{\partial \langle p \rangle_l}{\partial x_i} + \frac{\partial}{\partial x_j} \left[\mu \left(\frac{\partial \langle u_i \rangle_l}{\partial x_j} + \frac{\partial \langle u_j \rangle_l}{\partial x_i} \right) \right] \\ &\quad - \frac{2}{3} \frac{\partial}{\partial x_i} \left(\mu \frac{\partial \langle u_j \rangle_l}{\partial x_j} \right) - \frac{\partial \langle \rho \rangle_l \tau_L(u_i, u_j)}{\partial x_j}, \end{aligned} \quad (3.6b)$$

$$\frac{\partial \langle \rho \rangle_l \langle \phi_\alpha \rangle_L}{\partial t} + \frac{\partial \langle \rho \rangle_l \langle u_j \rangle_L \langle \phi_\alpha \rangle_L}{\partial x_j} = \frac{\partial}{\partial x_j} \left(\mu \frac{\partial \langle \phi_\alpha \rangle_l}{\partial x_j} \right) - \frac{\partial \langle \rho \rangle_l \tau_L(u_j, \phi_\alpha)}{\partial x_j} + \langle \rho S_\alpha \rangle_l, \quad (3.6c)$$

where the second-order SGS correlations

$$\tau_L(a, b) = \langle ab \rangle_L - \langle a \rangle_L \langle b \rangle_L \quad (3.7)$$

are governed by

$$\begin{aligned}
& \frac{\partial \langle \rho \rangle_l \tau_L(u_i, u_j)}{\partial t} + \frac{\partial \langle \rho \rangle_l \langle u_k \rangle_L \tau_L(u_i, u_j)}{\partial x_k} = - \frac{\partial \langle \rho \rangle_l \tau_L(u_k, u_i, u_j)}{\partial x_k} \\
& - \langle \rho \rangle_l \tau_L(u_i, u_k) \frac{\partial \langle u_j \rangle_L}{\partial x_k} - \langle \rho \rangle_l \tau_L(u_j, u_k) \frac{\partial \langle u_i \rangle_L}{\partial x_k} \\
& + \left[\frac{\partial}{\partial x_k} \left(\mu \frac{\partial \langle u_i u_j \rangle_l}{\partial x_k} \right) - \langle u_j \rangle_L \frac{\partial}{\partial x_k} \left(\mu \frac{\partial \langle u_i \rangle_l}{\partial x_k} \right) - \langle u_i \rangle_L \frac{\partial}{\partial x_k} \left(\mu \frac{\partial \langle u_j \rangle_l}{\partial x_k} \right) \right] \\
& + \left[\left\langle u_j \frac{\partial}{\partial x_k} \left(\mu \frac{\partial u_k}{\partial x_i} \right) \right\rangle_l - \langle u_j \rangle_L \frac{\partial}{\partial x_k} \left(\mu \frac{\partial \langle u_k \rangle_l}{\partial x_i} \right) \right] \\
& + \left[\left\langle u_i \frac{\partial}{\partial x_k} \left(\mu \frac{\partial u_k}{\partial x_j} \right) \right\rangle_l - \langle u_i \rangle_L \frac{\partial}{\partial x_k} \left(\mu \frac{\partial \langle u_k \rangle_l}{\partial x_j} \right) \right] \\
& - \frac{2}{3} \left[\left\langle u_j \frac{\partial}{\partial x_i} \left(\mu \frac{\partial u_k}{\partial x_k} \right) \right\rangle_l - \langle u_j \rangle_L \frac{\partial}{\partial x_i} \left(\mu \frac{\partial \langle u_k \rangle_l}{\partial x_k} \right) \right] \\
& - \frac{2}{3} \left[\left\langle u_i \frac{\partial}{\partial x_j} \left(\mu \frac{\partial u_k}{\partial x_k} \right) \right\rangle_l - \langle u_i \rangle_L \frac{\partial}{\partial x_j} \left(\mu \frac{\partial \langle u_k \rangle_l}{\partial x_k} \right) \right] \\
& - \left[\left\langle u_j \frac{\partial p}{\partial x_i} \right\rangle_l - \langle u_j \rangle_L \frac{\partial \langle p \rangle_l}{\partial x_i} \right] - \left[\left\langle u_i \frac{\partial p}{\partial x_j} \right\rangle_l - \langle u_i \rangle_L \frac{\partial \langle p \rangle_l}{\partial x_j} \right] - \left[2\mu \left\langle \frac{\partial u_i}{\partial x_k} \frac{\partial u_j}{\partial x_k} \right\rangle_l \right],
\end{aligned} \tag{3.8a}$$

$$\begin{aligned}
& \frac{\partial \langle \rho \rangle_l \tau_L(u_i, \phi_\alpha)}{\partial t} + \frac{\partial \langle \rho \rangle_l \langle u_j \rangle_L \tau_L(u_i, \phi_\alpha)}{\partial x_j} = - \frac{\partial \langle \rho \rangle_l \tau_L(u_j, u_i, \phi_\alpha)}{\partial x_j} \\
& - \langle \rho \rangle_l \tau_L(u_i, u_j) \frac{\partial \langle \phi_\alpha \rangle_L}{\partial x_j} - \langle \rho \rangle_l \tau_L(u_j, \phi_\alpha) \frac{\partial \langle u_i \rangle_L}{\partial x_j} \\
& + \left[\frac{\partial}{\partial x_j} \left(\mu \frac{\partial \langle u_i \phi_\alpha \rangle_l}{\partial x_j} \right) - \langle \phi_\alpha \rangle_L \frac{\partial}{\partial x_j} \left(\mu \frac{\partial \langle u_i \rangle_l}{\partial x_j} \right) - \langle u_i \rangle_L \frac{\partial}{\partial x_j} \left(\mu \frac{\partial \langle \phi_\alpha \rangle_l}{\partial x_j} \right) \right] \\
& + \left[\left\langle \phi_\alpha \frac{\partial}{\partial x_j} \left(\mu \frac{\partial u_j}{\partial x_i} \right) \right\rangle_l - \langle \phi_\alpha \rangle_L \frac{\partial}{\partial x_j} \left(\mu \frac{\partial \langle u_j \rangle_l}{\partial x_i} \right) \right] \\
& - \frac{2}{3} \left[\left\langle \phi_\alpha \frac{\partial}{\partial x_i} \left(\mu \frac{\partial u_j}{\partial x_j} \right) \right\rangle_l - \langle \phi_\alpha \rangle_L \frac{\partial}{\partial x_i} \left(\mu \frac{\partial \langle u_j \rangle_l}{\partial x_j} \right) \right] \\
& - \left[\left\langle \phi_\alpha \frac{\partial p}{\partial x_i} \right\rangle_l - \langle \phi_\alpha \rangle_L \frac{\partial \langle p \rangle_l}{\partial x_i} \right] - \left[2\mu \left\langle \frac{\partial u_i}{\partial x_j} \frac{\partial \phi_\alpha}{\partial x_j} \right\rangle_l \right] \\
& + [\langle \rho \rangle_l \tau_L(u_i, S_\alpha(\phi))],
\end{aligned} \tag{3.8b}$$

$$\begin{aligned}
& \frac{\partial \langle \rho \rangle_l \tau_L(\phi_\alpha, \phi_\beta)}{\partial t} + \frac{\partial \langle \rho \rangle_l \langle u_j \rangle_L \tau_L(\phi_\alpha, \phi_\beta)}{\partial x_j} = - \frac{\partial \langle \rho \rangle_l \tau_L(u_j, \phi_\alpha, \phi_\beta)}{\partial x_j} \\
& - \langle \rho \rangle_l \tau_L(\phi_\alpha, u_j) \frac{\partial \langle \phi_\beta \rangle_L}{\partial x_j} - \langle \rho \rangle_l \tau_L(\phi_\beta, u_j) \frac{\partial \langle \phi_\alpha \rangle_L}{\partial x_j} \\
& + \left[\frac{\partial}{\partial x_j} \left(\mu \frac{\partial \langle \phi_\alpha \phi_\beta \rangle_l}{\partial x_j} \right) - \langle \phi_\alpha \rangle_L \frac{\partial}{\partial x_j} \left(\mu \frac{\partial \langle \phi_\beta \rangle_l}{\partial x_j} \right) - \langle \phi_\beta \rangle_L \frac{\partial}{\partial x_j} \left(\mu \frac{\partial \langle \phi_\alpha \rangle_l}{\partial x_j} \right) \right] \\
& - \left[2\mu \left\langle \frac{\partial \phi_\alpha}{\partial x_j} \frac{\partial \phi_\beta}{\partial x_j} \right\rangle_l \right] \\
& + \langle \rho \rangle_l [\tau_L(\phi_\alpha, S_\beta(\phi)) + \tau_L(\phi_\beta, S_\alpha(\phi))]. \tag{3.8c}
\end{aligned}$$

In this equation, the third order correlations

$$\begin{aligned}
\tau_L(a, b, c) &= \langle abc \rangle_L - \langle a \rangle_L \tau_L(b, c) \\
&\quad - \langle b \rangle_L \tau_L(a, c) - \langle c \rangle_L \tau_L(a, b) - \langle a \rangle_L \langle b \rangle_L \langle c \rangle_L \tag{3.9}
\end{aligned}$$

along with the other terms within square brackets are unclosed. Equations (3.6), (3.8) provide an “exact” form of the transport equations. Applying the conventional LES approximation ($\langle f \rangle_l \approx \langle f \rangle_L$) to diffusion terms in these equations, we obtain

$$\begin{aligned}
\frac{\partial \langle \rho \rangle_l \langle u_i \rangle_L}{\partial t} + \frac{\partial \langle \rho \rangle_l \langle u_j \rangle_L \langle u_i \rangle_L}{\partial x_j} &= - \frac{\partial \langle \rho \rangle_l}{\partial x_i} + \frac{\partial}{\partial x_j} \left[\mu \left(\frac{\partial \langle u_i \rangle_L}{\partial x_j} + \frac{\partial \langle u_j \rangle_L}{\partial x_i} \right) \right] \\
&\quad - \frac{2}{3} \frac{\partial}{\partial x_i} \left(\mu \frac{\partial \langle u_j \rangle_L}{\partial x_j} \right) - \frac{\partial \langle \rho \rangle_l \tau_L(u_i, u_j)}{\partial x_j}, \tag{3.10a}
\end{aligned}$$

$$\begin{aligned}
\frac{\partial \langle \rho \rangle_l \langle \phi_\alpha \rangle_L}{\partial t} + \frac{\partial \langle \rho \rangle_l \langle u_j \rangle_L \langle \phi_\alpha \rangle_L}{\partial x_j} &= \frac{\partial}{\partial x_j} \left(\mu \frac{\partial \langle \phi_\alpha \rangle_L}{\partial x_j} \right) - \frac{\partial \langle \rho \rangle_l \tau_L(u_j, \phi_\alpha)}{\partial x_j} + \langle \rho S_\alpha \rangle_l, \tag{3.10b}
\end{aligned}$$

$$\begin{aligned}
& \frac{\partial \langle \rho \rangle_l \tau_L(u_i, u_j)}{\partial t} + \frac{\partial \langle \rho \rangle_l \langle u_k \rangle_L \tau_L(u_i, u_j)}{\partial x_k} = - \frac{\partial \langle \rho \rangle_l \tau_L(u_k, u_i, u_j)}{\partial x_k} \\
& - \langle \rho \rangle_l \tau_L(u_i, u_k) \frac{\partial \langle u_j \rangle_L}{\partial x_k} - \langle \rho \rangle_l \tau_L(u_j, u_k) \frac{\partial \langle u_i \rangle_L}{\partial x_k} + \frac{\partial}{\partial x_k} \left(\mu \frac{\partial \tau_L(u_i, u_j)}{\partial x_k} \right) \\
& + \tau_L \left(u_j, \frac{\partial}{\partial x_k} \left(\mu \frac{\partial u_k}{\partial x_i} \right) \right) + \tau_L \left(u_i, \frac{\partial}{\partial x_k} \left(\mu \frac{\partial u_k}{\partial x_j} \right) \right) \\
& - \frac{2}{3} \tau_L \left(u_j, \frac{\partial}{\partial x_i} \left(\mu \frac{\partial u_k}{\partial x_k} \right) \right) - \frac{2}{3} \tau_L \left(u_i, \frac{\partial}{\partial x_j} \left(\mu \frac{\partial u_k}{\partial x_k} \right) \right) \\
& - \left[\left\langle u_j \frac{\partial p}{\partial x_i} \right\rangle_l - \langle u_j \rangle_L \frac{\partial \langle p \rangle_l}{\partial x_i} \right] - \left[\left\langle u_i \frac{\partial p}{\partial x_j} \right\rangle_l - \langle u_i \rangle_L \frac{\partial \langle p \rangle_l}{\partial x_j} \right] - 2\mu \tau_L \left(\frac{\partial u_i}{\partial x_k}, \frac{\partial u_j}{\partial x_k} \right),
\end{aligned} \tag{3.11a}$$

$$\begin{aligned}
& \frac{\partial \langle \rho \rangle_l \tau_L(u_i, \phi_\alpha)}{\partial t} + \frac{\partial \langle \rho \rangle_l \langle u_j \rangle_L \tau_L(u_i, \phi_\alpha)}{\partial x_j} = - \frac{\partial \langle \rho \rangle_l \tau_L(u_j, u_i, \phi_\alpha)}{\partial x_j} \\
& - \langle \rho \rangle_l \tau_L(u_i, u_j) \frac{\partial \langle \phi_\alpha \rangle_L}{\partial x_j} - \langle \rho \rangle_l \tau_L(u_j, \phi_\alpha) \frac{\partial \langle u_i \rangle_L}{\partial x_j} + \frac{\partial}{\partial x_j} \left(\mu \frac{\partial \tau_L(u_i, \phi_\alpha)}{\partial x_j} \right) \\
& + \tau_L \left(\phi_\alpha, \frac{\partial}{\partial x_j} \left(\mu \frac{\partial u_j}{\partial x_i} \right) \right) - \frac{2}{3} \tau_L \left(\phi_\alpha, \frac{\partial}{\partial x_i} \left(\mu \frac{\partial u_j}{\partial x_j} \right) \right) \\
& - \left[\left\langle \phi_\alpha \frac{\partial p}{\partial x_i} \right\rangle_l - \langle \phi_\alpha \rangle_L \frac{\partial \langle p \rangle_l}{\partial x_i} \right] - 2\mu \tau_L \left(\frac{\partial u_i}{\partial x_j}, \frac{\partial \phi_\alpha}{\partial x_j} \right) \\
& + [\langle \rho \rangle_l \tau_L(u_i, S_\alpha(\phi))],
\end{aligned} \tag{3.11b}$$

$$\begin{aligned}
& \frac{\partial \langle \rho \rangle_l \tau_L(\phi_\alpha, \phi_\beta)}{\partial t} + \frac{\partial \langle \rho \rangle_l \langle u_j \rangle_L \tau_L(\phi_\alpha, \phi_\beta)}{\partial x_j} = - \frac{\partial \langle \rho \rangle_l \tau_L(u_j, \phi_\alpha, \phi_\beta)}{\partial x_j} \\
& - \langle \rho \rangle_l \tau_L(\phi_\alpha, u_j) \frac{\partial \langle \phi_\beta \rangle_L}{\partial x_j} - \langle \rho \rangle_l \tau_L(\phi_\beta, u_j) \frac{\partial \langle \phi_\alpha \rangle_L}{\partial x_j} + \frac{\partial}{\partial x_j} \left(\mu \frac{\partial \tau_L(\phi_\alpha, \phi_\beta)}{\partial x_j} \right) \\
& - 2\mu \tau_L \left(\frac{\partial \phi_\alpha}{\partial x_j}, \frac{\partial \phi_\beta}{\partial x_j} \right) + \langle \rho \rangle_l [\tau_L(\phi_\alpha, S_\beta(\phi)) + \tau_L(\phi_\beta, S_\alpha(\phi))].
\end{aligned} \tag{3.11c}$$

3.2 VELOCITY-SCALAR FILTERED MASS DENSITY FUNCTION (VSFMDf)

3.2.1 Definitions

The “velocity-scalar filtered mass density function” (VSFMDf), denoted by P_L , is formally defined as²

$$P_L(\mathbf{v}, \boldsymbol{\psi}; \mathbf{x}, t) = \int_{-\infty}^{+\infty} \rho(\mathbf{x}', t) \zeta(\mathbf{v}, \boldsymbol{\psi}; \mathbf{u}(\mathbf{x}', t), \boldsymbol{\phi}(\mathbf{x}', t)) G(\mathbf{x}' - \mathbf{x}) d\mathbf{x}', \quad (3.12)$$

where

$$\zeta(\mathbf{v}, \boldsymbol{\psi}; \mathbf{u}(\mathbf{x}, t), \boldsymbol{\phi}(\mathbf{x}, t)) = \prod_{i=1}^3 \delta(v_i - u_i(\mathbf{x}, t)) \times \prod_{\alpha=1}^{N_s+1} \delta(\psi_\alpha - \phi_\alpha(\mathbf{x}, t)). \quad (3.13)$$

In this equation, δ denotes the Dirac delta function, and $\mathbf{v}, \boldsymbol{\psi}$ are the velocity vector and the scalar array in the sample space. The term ζ is the “fine-grained” density.^{44,50} Eq. (3.12) defines VSFMDf as the spatially filtered value of the fine-grained density. With the condition of a positive filter kernel,⁵¹ P_L has all of the properties of a mass density function (mdf).⁴⁴ For further developments it is useful to define the “conditional filtered value” of the variable $Q(\mathbf{x}, t)$ as

$$\left\langle Q(\mathbf{x}, t) \mid \mathbf{u}(\mathbf{x}, t) = \mathbf{v}, \boldsymbol{\phi}(\mathbf{x}, t) = \boldsymbol{\psi} \right\rangle_l \equiv \left\langle Q \mid \mathbf{v}, \boldsymbol{\psi} \right\rangle_l = \frac{\int_{-\infty}^{+\infty} Q(\mathbf{x}', t) \rho(\mathbf{x}', t) \zeta(\mathbf{v}, \boldsymbol{\psi}; \mathbf{u}(\mathbf{x}', t), \boldsymbol{\phi}(\mathbf{x}', t)) G(\mathbf{x}' - \mathbf{x}) d\mathbf{x}'}{P_L(\mathbf{v}, \boldsymbol{\psi}; \mathbf{x}, t)}. \quad (3.14)$$

Equation (3.14) implies the following:

$$(i) \quad \text{for } Q(\mathbf{x}, t) = c, \quad \left\langle Q(\mathbf{x}, t) \middle| \mathbf{v}, \boldsymbol{\psi} \right\rangle_l = c, \quad (3.15a)$$

$$(ii) \quad \text{for } Q(\mathbf{x}, t) \equiv \hat{Q}(\mathbf{u}(\mathbf{x}, t), \boldsymbol{\phi}(\mathbf{x}, t)), \quad \left\langle Q(\mathbf{x}, t) \middle| \mathbf{v}, \boldsymbol{\psi} \right\rangle_l = \hat{Q}(\mathbf{v}, \boldsymbol{\psi}). \quad (3.15b)$$

$$(iii) \quad \text{Integral properties:} \quad \begin{aligned} \langle \rho(\mathbf{x}, t) \rangle_l \langle Q(\mathbf{x}, t) \rangle_L &= \langle \rho(\mathbf{x}, t) Q(\mathbf{x}, t) \rangle_l = \\ &= \int_{-\infty}^{+\infty} \int_{-\infty}^{+\infty} \left\langle Q(\mathbf{x}, t) \middle| \mathbf{v}, \boldsymbol{\psi} \right\rangle_l P_L(\mathbf{v}, \boldsymbol{\psi}; \mathbf{x}, t) d\mathbf{v} d\boldsymbol{\psi}. \end{aligned} \quad (3.15c)$$

From Eqs. (3.15) it follows that the filtered value of any function of the velocity and/or scalar variables is obtained by its integration over the velocity and scalar sample spaces

$$\langle \rho(\mathbf{x}, t) \rangle_l \langle Q(\mathbf{x}, t) \rangle_L = \int_{-\infty}^{+\infty} \int_{-\infty}^{+\infty} \hat{Q}(\mathbf{v}, \boldsymbol{\psi}) P_L(\mathbf{v}, \boldsymbol{\psi}; \mathbf{x}, t) d\mathbf{v} d\boldsymbol{\psi}. \quad (3.16)$$

3.2.2 VSF MDF Transport Equations

To develop the VSF MDF transport equation, we consider the time derivative of the fine-grained density function (Eq. (3.13))

$$\frac{\partial \zeta}{\partial t} = - \left(\frac{\partial u_k}{\partial t} \frac{\partial \zeta}{\partial v_k} + \frac{\partial \phi_\alpha}{\partial t} \frac{\partial \zeta}{\partial \psi_\alpha} \right). \quad (3.17)$$

Substituting Eqs. (3.1b), (3.1c), and Eqs. (3.4a), (3.4b) into Eq. (3.17) we obtain

$$\frac{\partial \rho \zeta}{\partial t} + \frac{\partial u_j \rho \zeta}{\partial x_j} = \left(\frac{\partial p}{\partial x_j} - \frac{\partial \tau_{kj}}{\partial x_k} \right) \frac{\partial \zeta}{\partial v_j} + \left(\frac{\partial J_j^\alpha}{\partial x_j} - \rho S_\alpha(\boldsymbol{\phi}) \right) \frac{\partial \zeta}{\partial \psi_\alpha}. \quad (3.18)$$

Integration of this equation according to Eq. (3.12), while employing Eq. (3.14) results in

$$\begin{aligned} \frac{\partial P_L}{\partial t} + \frac{\partial v_i P_L}{\partial x_i} &= - \frac{\partial}{\partial \psi_\alpha} [S_\alpha(\boldsymbol{\psi}) P_L] \\ &+ \frac{\partial}{\partial v_i} \left(\left\langle \frac{1}{\rho(\boldsymbol{\phi})} \frac{\partial p}{\partial x_i} \middle| \mathbf{v}, \boldsymbol{\psi} \right\rangle_l P_L \right) \\ &- \frac{\partial}{\partial v_i} \left(\left\langle \frac{1}{\rho(\boldsymbol{\phi})} \frac{\partial \tau_{ji}}{\partial x_j} \middle| \mathbf{v}, \boldsymbol{\psi} \right\rangle_l P_L \right) \\ &+ \frac{\partial}{\partial \psi_\alpha} \left(\left\langle \frac{1}{\rho(\boldsymbol{\phi})} \frac{\partial J_i^\alpha}{\partial x_i} \middle| \mathbf{v}, \boldsymbol{\psi} \right\rangle_l P_L \right). \end{aligned} \quad (3.19)$$

This is an exact transport equation and indicates that the effects of convection (second term on LHS) and chemical reaction (the first term on RHS) appear in closed forms. The unclosed terms denote convective effects in the velocity-scalar sample space. Alternatively, the VSF MDF equation can be expressed as

$$\begin{aligned}
& \frac{\partial P_L}{\partial t} + \frac{\partial v_i P_L}{\partial x_i} = \frac{\partial}{\partial x_i} \left[\mu \frac{\partial (P_L / \rho(\boldsymbol{\psi}))}{\partial x_i} \right] - \frac{\partial}{\partial \psi_\alpha} [S_\alpha(\boldsymbol{\psi}) P_L] \\
& + \frac{\partial}{\partial v_i} \left[\left\langle \frac{1}{\rho(\boldsymbol{\phi})} \frac{\partial p}{\partial x_i} \middle| \mathbf{v}, \boldsymbol{\psi} \right\rangle_l P_L \right] - \frac{\partial^2}{\partial v_i \partial v_j} \left[\left\langle \frac{\mu}{\rho(\boldsymbol{\phi})} \frac{\partial u_i}{\partial x_k} \frac{\partial u_j}{\partial x_k} \middle| \mathbf{v}, \boldsymbol{\psi} \right\rangle_l P_L \right] \\
& - \frac{\partial}{\partial v_i} \left[\left\langle \frac{1}{\rho(\boldsymbol{\phi})} \frac{\partial}{\partial x_j} \left(\mu \frac{\partial u_j}{\partial x_i} \right) \middle| \mathbf{v}, \boldsymbol{\psi} \right\rangle_l P_L \right] + \frac{\partial}{\partial v_i} \left[\left\langle \frac{1}{\rho(\boldsymbol{\phi})} \frac{\partial}{\partial x_i} \left(\frac{2}{3} \mu \frac{\partial u_j}{\partial x_j} \right) \middle| \mathbf{v}, \boldsymbol{\psi} \right\rangle_l P_L \right] \\
& - 2 \frac{\partial^2}{\partial v_i \partial \psi_\alpha} \left[\left\langle \frac{\mu}{\rho(\boldsymbol{\phi})} \frac{\partial u_i}{\partial x_j} \frac{\partial \phi_\alpha}{\partial x_j} \middle| \mathbf{v}, \boldsymbol{\psi} \right\rangle_l P_L \right] - \frac{\partial^2}{\partial \psi_\alpha \partial \psi_\beta} \left[\left\langle \frac{\mu}{\rho(\boldsymbol{\phi})} \frac{\partial \phi_\alpha}{\partial x_i} \frac{\partial \phi_\beta}{\partial x_i} \middle| \mathbf{v}, \boldsymbol{\psi} \right\rangle_l P_L \right].
\end{aligned} \tag{3.20}$$

This is also an exact equation. The unclosed terms are exhibited by the conditional filtered values as shown by the last six terms on the RHS.

3.2.3 Modeled VSF MDF Transport Equation

For closure of the VSF MDF transport equation, we consider the general diffusion process,⁵² given by the system of stochastic differential equations (SDEs):

$$\begin{aligned}
dX_i^+(t) &= D_i^X(\mathbf{X}^+, \mathbf{U}^+, \boldsymbol{\phi}^+; t) dt + B_{ij}^X(\mathbf{X}^+, \mathbf{U}^+, \boldsymbol{\phi}^+; t) dW_j^X(t) \\
&+ F_{ij}^{XU}(\mathbf{X}^+, \mathbf{U}^+, \boldsymbol{\phi}^+; t) dW_j^U(t) + F_{ij}^{X\phi}(\mathbf{X}^+, \mathbf{U}^+, \boldsymbol{\phi}^+; t) dW_j^\phi(t), \tag{3.21a}
\end{aligned}$$

$$\begin{aligned}
dU_i^+(t) &= D_i^U(\mathbf{X}^+, \mathbf{U}^+, \boldsymbol{\phi}^+; t) dt + B_{ij}^U(\mathbf{X}^+, \mathbf{U}^+, \boldsymbol{\phi}^+; t) dW_j^U(t) \\
&+ F_{ij}^{UX}(\mathbf{X}^+, \mathbf{U}^+, \boldsymbol{\phi}^+; t) dW_j^X(t) + F_{ij}^{U\phi}(\mathbf{X}^+, \mathbf{U}^+, \boldsymbol{\phi}^+; t) dW_j^\phi(t), \tag{3.21b}
\end{aligned}$$

$$\begin{aligned}
d\phi_\alpha^+(t) &= D_\alpha^\phi(\mathbf{X}^+, \mathbf{U}^+, \boldsymbol{\phi}^+; t) dt + B_{\alpha j}^\phi(\mathbf{X}^+, \mathbf{U}^+, \boldsymbol{\phi}^+; t) dW_j^\phi(t) \\
&+ F_{\alpha j}^{\phi X}(\mathbf{X}^+, \mathbf{U}^+, \boldsymbol{\phi}^+; t) dW_j^X(t) + F_{\alpha j}^{\phi U}(\mathbf{X}^+, \mathbf{U}^+, \boldsymbol{\phi}^+; t) dW_j^U(t), \tag{3.21c}
\end{aligned}$$

where $X_i^+, U_i^+, \phi_\alpha^+$ are probabilistic representations of position, velocity vector, and scalar variables, respectively. The D terms denote drift coefficient, the B terms denote diffusion, the F terms denote diffusion couplings, and the W terms denote the Wiener-Lévy processes.^{53,54} To model these coefficients, we utilize the generalized Langevin model (GLM) and the linear

mean square estimation (LMSE) model,⁵⁰ following Refs.^{9,11,55,56} To account for fluid density variations, two stochastic models in the form of Eq. (3.21) are constructed:

3.2.3.1 Model 1 (M1): In this model the fluctuations of density within the SGS are taken into account.

$$dX_i^+ = U_i^+ dt + \sqrt{\frac{2\mu}{\rho(\phi^+)}} dW_i, \quad (3.22a)$$

$$dU_i^+ = \left[-\frac{1}{\rho(\phi^+)} \frac{\partial \langle p \rangle_l}{\partial x_i} + \frac{2\mu}{\rho(\phi^+)} \frac{\partial^2 \langle u_i \rangle_L}{\partial x_j \partial x_j} + \frac{\mu}{\rho(\phi^+)} \frac{\partial^2 \langle u_j \rangle_L}{\partial x_j \partial x_i} - \frac{2}{3} \frac{\mu}{\rho(\phi^+)} \frac{\partial^2 \langle u_j \rangle_L}{\partial x_i \partial x_j} \right] dt \\ + G_{ij} (U_j^+ - \langle u_j \rangle_L) dt + \sqrt{C_0 \epsilon} dW_i' + \sqrt{\frac{2\mu}{\rho(\phi^+)}} \frac{\partial \langle u_i \rangle_L}{\partial x_j} dW_j, \quad (3.22b)$$

$$d\phi_\alpha^+ = -C_\phi \omega (\phi_\alpha^+ - \langle \phi_\alpha \rangle_L) dt + S_\alpha(\phi^+) dt, \quad (3.22c)$$

where

$$G_{ij} = -\omega \left(\frac{1}{2} + \frac{3}{4} C_0 \right) \delta_{ij} \quad \omega = \frac{\epsilon}{k} \\ \epsilon = C_\epsilon \frac{k^3}{\Delta_L} \quad k = \frac{1}{2} \tau(u_k, u_k). \quad (3.23)$$

Here ω is the SGS mixing frequency, ϵ is the SGS dissipation rate, k is the SGS kinetic energy, and Δ_L is the LES filter size. The parameters C_0 , C_ϕ and C_ϵ are model constants and need to be specified. The Fokker-Planck equation⁵⁷ for $F_L(\mathbf{v}, \boldsymbol{\psi}, \mathbf{x}; t)$, the joint PDF of \mathbf{X}^+ , \mathbf{U}^+ , $\boldsymbol{\phi}^+$, evolving by the diffusion process as given by Eq. (3.22) is

$$\frac{\partial F_L}{\partial t} + \frac{\partial v_i F_L}{\partial x_i} = \frac{1}{\rho(\boldsymbol{\psi})} \frac{\partial \langle p \rangle_l}{\partial x_i} \frac{\partial F_L}{\partial v_i} - \frac{2\mu}{\rho(\boldsymbol{\psi})} \frac{\partial^2 \langle u_i \rangle_L}{\partial x_j \partial x_j} \frac{\partial F_L}{\partial v_i} - \frac{\mu}{\rho(\boldsymbol{\psi})} \frac{\partial^2 \langle u_j \rangle_L}{\partial x_i \partial x_j} \frac{\partial F_L}{\partial v_i} \\ + \frac{2}{3} \frac{\mu}{\rho(\boldsymbol{\psi})} \frac{\partial^2 \langle u_j \rangle_L}{\partial x_j \partial x_i} \frac{\partial F_L}{\partial v_i} - G_{ij} \frac{\partial [(v_j - \langle u_j \rangle_L) F_L]}{\partial v_i} + \frac{\mu}{\rho(\boldsymbol{\psi})} \frac{\partial^2 F_L}{\partial x_j \partial x_j} \\ + \frac{2\mu}{\rho(\boldsymbol{\psi})} \frac{\partial}{\partial x_j} \left(\frac{\partial \langle u_i \rangle_L}{\partial x_j} \frac{\partial F_L}{\partial v_i} \right) + \frac{\mu}{\rho(\boldsymbol{\psi})} \frac{\partial \langle u_i \rangle_L}{\partial x_k} \frac{\partial \langle u_j \rangle_L}{\partial x_k} \frac{\partial^2 F_L}{\partial v_i \partial v_j} + \frac{1}{2} C_0 \epsilon \frac{\partial^2 F_L}{\partial v_j \partial v_j} \\ + C_\phi \omega \frac{\partial [(\psi_\alpha - \langle \phi_\alpha \rangle_L) F_L]}{\partial \psi_\alpha} - \frac{\partial [S_\alpha(\boldsymbol{\psi}) F_L]}{\partial \psi_\alpha}. \quad (3.24)$$

The transport equations for the filtered variables are obtained by integration of Eq. (3.24) according to Eq. (3.16)

$$\frac{\partial \langle \rho \rangle_l}{\partial t} + \frac{\partial \langle \rho \rangle_l \langle u_j \rangle_L}{\partial x_j} = 0, \quad (3.25a)$$

$$\begin{aligned} \frac{\partial \langle \rho \rangle_l \langle u_i \rangle_L}{\partial t} + \frac{\partial \langle \rho \rangle_l \langle u_j \rangle_L \langle u_i \rangle_L}{\partial x_j} &= -\frac{\partial \langle p \rangle_l}{\partial x_i} + \frac{\partial}{\partial x_j} \left(\mu \frac{\partial \langle u_i \rangle_l}{\partial x_j} \right) + \frac{\partial}{\partial x_j} \left(\mu \frac{\partial \langle u_j \rangle_L}{\partial x_i} \right) \\ &\quad - \frac{2}{3} \frac{\partial}{\partial x_i} \left(\mu \frac{\partial \langle u_j \rangle_L}{\partial x_j} \right) - \frac{\partial \langle \rho \rangle_l \tau_L(u_i, u_j)}{\partial x_j}, \end{aligned} \quad (3.25b)$$

$$\begin{aligned} \frac{\partial \langle \rho \rangle_l \langle \phi_\alpha \rangle_L}{\partial t} + \frac{\partial \langle \rho \rangle_l \langle u_j \rangle_L \langle \phi_\alpha \rangle_L}{\partial x_j} &= \frac{\partial}{\partial x_j} \left(\mu \frac{\partial \langle \phi_\alpha \rangle_l}{\partial x_j} \right) - \frac{\partial \langle \rho \rangle_l \tau_L(\phi_\alpha, u_j)}{\partial x_j} \\ &\quad + \langle \rho \rangle_l \langle S_\alpha(\phi) \rangle_L. \end{aligned} \quad (3.25c)$$

The transport equations for the second order SGS moments are

$$\begin{aligned} \frac{\partial \langle \rho \rangle_l \tau_L(u_i, u_j)}{\partial t} + \frac{\partial \langle \rho \rangle_l \langle u_k \rangle_L \tau_L(u_i, u_j)}{\partial x_k} &= -\frac{\partial \langle \rho \rangle_l \tau_L(u_k, u_i, u_j)}{\partial x_k} \\ &\quad - \langle \rho \rangle_l \tau_L(u_i, u_k) \frac{\partial \langle u_j \rangle_L}{\partial x_k} - \langle \rho \rangle_l \tau_L(u_j, u_k) \frac{\partial \langle u_i \rangle_L}{\partial x_k} \\ &\quad + \left[\frac{\partial}{\partial x_k} \left(\mu \frac{\partial \langle u_i u_j \rangle_l}{\partial x_k} \right) - \langle u_j \rangle_L \frac{\partial}{\partial x_k} \left(\mu \frac{\partial \langle u_i \rangle_l}{\partial x_k} \right) - \langle u_i \rangle_L \frac{\partial}{\partial x_k} \left(\mu \frac{\partial \langle u_j \rangle_l}{\partial x_k} \right) \right] \\ &\quad + (\langle u_j \rangle_l - \langle u_j \rangle_L) \left[\frac{\partial}{\partial x_k} \left(\mu \frac{\partial \langle u_k \rangle_L}{\partial x_i} \right) - \frac{2}{3} \frac{\partial}{\partial x_i} \left(\mu \frac{\partial \langle u_k \rangle_L}{\partial x_k} \right) \right] \\ &\quad + (\langle u_i \rangle_l - \langle u_i \rangle_L) \left[\frac{\partial}{\partial x_k} \left(\mu \frac{\partial \langle u_k \rangle_L}{\partial x_j} \right) - \frac{2}{3} \frac{\partial}{\partial x_j} \left(\mu \frac{\partial \langle u_k \rangle_L}{\partial x_k} \right) \right] \\ &\quad - (\langle u_j \rangle_l - \langle u_j \rangle_L) \left(\frac{\partial \langle p \rangle_l}{\partial x_i} \right) \\ &\quad - (\langle u_i \rangle_l - \langle u_i \rangle_L) \left(\frac{\partial \langle p \rangle_l}{\partial x_j} \right) \\ &\quad + \langle \rho \rangle_l G_{ik} \tau_L(u_j, u_k) + \langle \rho \rangle_l G_{jk} \tau_L(u_i, u_k) + \langle \rho \rangle_l C_0 \epsilon \delta_{ij} \\ &\quad - 2\mu \left(\frac{\partial \langle u_i \rangle_l}{\partial x_k} \frac{\partial \langle u_j \rangle_L}{\partial x_k} + \frac{\partial \langle u_j \rangle_l}{\partial x_k} \frac{\partial \langle u_i \rangle_L}{\partial x_k} - \frac{\partial \langle u_i \rangle_L}{\partial x_k} \frac{\partial \langle u_j \rangle_L}{\partial x_k} \right), \end{aligned} \quad (3.26a)$$

$$\begin{aligned}
& \frac{\partial \langle \rho \rangle_l \tau_L(u_i, \phi_\alpha)}{\partial t} + \frac{\partial \langle \rho \rangle_l \langle u_j \rangle_L \tau_L(u_i, \phi_\alpha)}{\partial x_j} = - \frac{\partial \langle \rho \rangle_l \tau_L(u_j, u_i, \phi_\alpha)}{\partial x_j} - 2\mu \frac{\partial \langle u_i \rangle_L}{\partial x_k} \frac{\partial \langle \phi_\alpha \rangle_l}{\partial x_k} \\
& - \langle \rho \rangle_l \tau_L(u_i, u_j) \frac{\partial \langle \phi_\alpha \rangle_L}{\partial x_j} - \langle \rho \rangle_l \tau_L(u_j, \phi_\alpha) \frac{\partial \langle u_i \rangle_L}{\partial x_j} \\
& + \left[\frac{\partial}{\partial x_j} \left(\mu \frac{\partial \langle u_i \phi_\alpha \rangle_l}{\partial x_j} \right) - \langle \phi_\alpha \rangle_L \frac{\partial}{\partial x_j} \left(\mu \frac{\partial \langle u_i \rangle_l}{\partial x_j} \right) - \langle u_i \rangle_L \frac{\partial}{\partial x_j} \left(\mu \frac{\partial \langle \phi_\alpha \rangle_l}{\partial x_j} \right) \right] \\
& + (\langle \phi_\alpha \rangle_l - \langle \phi_\alpha \rangle_L) \left[\frac{\partial}{\partial x_j} \left(\mu \frac{\partial \langle u_j \rangle_L}{\partial x_i} \right) - \frac{2}{3} \frac{\partial}{\partial x_i} \left(\mu \frac{\partial \langle u_j \rangle_L}{\partial x_j} \right) - \frac{\partial \langle p \rangle_l}{\partial x_i} \right] \\
& + \langle \rho \rangle_l G_{ij} \tau_L(u_j, \phi_\alpha) - \langle \rho \rangle_l C_\phi \omega \tau_L(u_i, \phi_\alpha) + \langle \rho \rangle_l \tau_L(u_i, S_\alpha(\phi)),
\end{aligned} \tag{3.26b}$$

$$\begin{aligned}
& \frac{\partial \langle \rho \rangle_l \tau_L(\phi_\alpha, \phi_\beta)}{\partial t} + \frac{\partial \langle \rho \rangle_l \langle u_i \rangle_L \tau_L(\phi_\alpha, \phi_\beta)}{\partial x_i} = - \frac{\partial \langle \rho \rangle_l \tau_L(u_i, \phi_\alpha, \phi_\beta)}{\partial x_i} \\
& - \langle \rho \rangle_l \tau_L(\phi_\alpha, u_i) \frac{\partial \langle \phi_\beta \rangle_L}{\partial x_i} - \langle \rho \rangle_l \tau_L(\phi_\beta, u_i) \frac{\partial \langle \phi_\alpha \rangle_L}{\partial x_i} \\
& + \left[\frac{\partial}{\partial x_i} \left(\mu \frac{\partial \langle \phi_\alpha \phi_\beta \rangle_l}{\partial x_i} \right) - \langle \phi_\alpha \rangle_L \frac{\partial}{\partial x_i} \left(\mu \frac{\partial \langle \phi_\beta \rangle_l}{\partial x_i} \right) - \langle \phi_\beta \rangle_L \frac{\partial}{\partial x_i} \left(\mu \frac{\partial \langle \phi_\alpha \rangle_l}{\partial x_i} \right) \right] \\
& - 2 \langle \rho \rangle_l C_\phi \omega \tau_L(\phi_\alpha, \phi_\beta) + \langle \rho \rangle_l \tau_L(\phi_\alpha, S_\beta(\phi)) + \langle \rho \rangle_l \tau_L(\phi_\beta, S_\alpha(\phi)).
\end{aligned} \tag{3.26c}$$

The implied closure for the SDEs (3.22) is obtained by comparing the Fokker-Planck equation (Eq. (3.24)) to VSFMD transport equation (Eq. (3.20))

$$\begin{aligned}
& \frac{\partial}{\partial v_i} \left[\left\langle \frac{1}{\rho(\phi)} \frac{\partial p}{\partial x_i} \middle| \mathbf{v}, \boldsymbol{\psi} \right\rangle_l P_L \right] - \frac{\partial^2}{\partial v_i \partial v_j} \left[\left\langle \frac{\mu}{\rho(\phi)} \frac{\partial u_i}{\partial x_k} \frac{\partial u_j}{\partial x_k} \middle| \mathbf{v}, \boldsymbol{\psi} \right\rangle_l P_L \right] \\
& - \frac{\partial}{\partial v_i} \left[\left\langle \frac{1}{\rho(\phi)} \frac{\partial}{\partial x_j} \left(\mu \frac{\partial u_j}{\partial x_i} \right) \middle| \mathbf{v}, \boldsymbol{\psi} \right\rangle_l P_L \right] + \frac{\partial}{\partial v_i} \left[\left\langle \frac{1}{\rho(\phi)} \frac{\partial}{\partial x_i} \left(\frac{2}{3} \mu \frac{\partial u_j}{\partial x_j} \right) \middle| \mathbf{v}, \boldsymbol{\psi} \right\rangle_l P_L \right] \\
& - 2 \frac{\partial^2}{\partial v_i \partial \psi_\alpha} \left[\left\langle \frac{\mu}{\rho(\phi)} \frac{\partial u_i}{\partial x_j} \frac{\partial \phi_\alpha}{\partial x_j} \middle| \mathbf{v}, \boldsymbol{\psi} \right\rangle_l P_L \right] - \frac{\partial^2}{\partial \psi_\alpha \partial \psi_\beta} \left[\left\langle \frac{\mu}{\rho(\phi)} \frac{\partial \phi_\alpha}{\partial x_i} \frac{\partial \phi_\beta}{\partial x_i} \middle| \mathbf{v}, \boldsymbol{\psi} \right\rangle_l P_L \right] = \\
& \frac{1}{\rho(\boldsymbol{\psi})} \frac{\partial \langle p \rangle_l}{\partial x_i} \frac{\partial F_L}{\partial v_i} - \frac{2\mu}{\rho(\boldsymbol{\psi})} \frac{\partial^2 \langle u_i \rangle_L}{\partial x_j \partial x_j} \frac{\partial F_L}{\partial v_i} - \frac{\mu}{\rho(\boldsymbol{\psi})} \frac{\partial^2 \langle u_j \rangle_L}{\partial x_i \partial x_j} \frac{\partial F_L}{\partial v_i} \\
& + \frac{2}{3} \frac{\mu}{\rho(\boldsymbol{\psi})} \frac{\partial^2 \langle u_j \rangle_L}{\partial x_j \partial x_i} \frac{\partial F_L}{\partial v_i} - G_{ij} \frac{\partial [(v_j - \langle u_j \rangle_L) F_L]}{\partial v_i} \\
& + \frac{2\mu}{\rho(\boldsymbol{\psi})} \frac{\partial}{\partial x_j} \left(\frac{\partial \langle u_i \rangle_L}{\partial x_j} \frac{\partial F_L}{\partial v_i} \right) + \frac{\mu}{\rho(\boldsymbol{\psi})} \frac{\partial \langle u_i \rangle_L}{\partial x_k} \frac{\partial \langle u_j \rangle_L}{\partial x_k} \frac{\partial^2 F_L}{\partial v_i \partial v_j} + \frac{1}{2} C_0 \epsilon \frac{\partial^2 F_L}{\partial v_i \partial v_i} \\
& + C_\phi \omega \frac{\partial [(\psi_\alpha - \langle \phi_\alpha \rangle_L) F_L]}{\partial \psi_\alpha}.
\end{aligned} \tag{3.27}$$

The set of Eqs. (3.25), (3.26) may be compared to Eqs. (3.6), (3.8). The closure at the second order level is

$$\begin{aligned}
& - 2\mu \left(\left\langle \frac{\partial u_i}{\partial x_k} \frac{\partial u_j}{\partial x_k} \right\rangle_l - \left(\frac{\partial \langle u_i \rangle_l}{\partial x_k} \frac{\partial \langle u_j \rangle_L}{\partial x_k} + \frac{\partial \langle u_i \rangle_L}{\partial x_k} \frac{\partial \langle u_j \rangle_l}{\partial x_k} \right) + \frac{\partial \langle u_i \rangle_L}{\partial x_k} \frac{\partial \langle u_j \rangle_L}{\partial x_k} \right) \\
& + \left[\left\langle u_j \frac{\partial}{\partial x_k} \left(\mu \frac{\partial u_k}{\partial x_i} \right) \right\rangle_l - \langle u_j \rangle_L \frac{\partial}{\partial x_k} \left(\mu \frac{\partial \langle u_k \rangle_l}{\partial x_i} \right) - (\langle u_j \rangle_l - \langle u_j \rangle_L) \frac{\partial}{\partial x_k} \left(\mu \frac{\partial \langle u_k \rangle_L}{\partial x_i} \right) \right] \\
& + \left[\left\langle u_i \frac{\partial}{\partial x_k} \left(\mu \frac{\partial u_k}{\partial x_j} \right) \right\rangle_l - \langle u_i \rangle_L \frac{\partial}{\partial x_k} \left(\mu \frac{\partial \langle u_k \rangle_l}{\partial x_j} \right) - (\langle u_i \rangle_l - \langle u_i \rangle_L) \frac{\partial}{\partial x_k} \left(\mu \frac{\partial \langle u_k \rangle_L}{\partial x_j} \right) \right] \\
& - \frac{2}{3} \left[\left\langle u_j \frac{\partial}{\partial x_i} \left(\mu \frac{\partial u_k}{\partial x_k} \right) \right\rangle_l - \langle u_j \rangle_L \frac{\partial}{\partial x_i} \left(\mu \frac{\partial \langle u_k \rangle_l}{\partial x_k} \right) - (\langle u_j \rangle_l - \langle u_j \rangle_L) \frac{\partial}{\partial x_i} \left(\mu \frac{\partial \langle u_k \rangle_L}{\partial x_k} \right) \right] \\
& - \frac{2}{3} \left[\left\langle u_i \frac{\partial}{\partial x_j} \left(\mu \frac{\partial u_k}{\partial x_k} \right) \right\rangle_l - \langle u_i \rangle_L \frac{\partial}{\partial x_j} \left(\mu \frac{\partial \langle u_k \rangle_l}{\partial x_k} \right) - (\langle u_i \rangle_l - \langle u_i \rangle_L) \frac{\partial}{\partial x_j} \left(\mu \frac{\partial \langle u_k \rangle_L}{\partial x_k} \right) \right] \\
& - \tau_l \left(u_i, \frac{\partial p}{\partial x_j} \right) - \tau_l \left(u_j, \frac{\partial p}{\partial x_i} \right) = \langle \rho \rangle_l G_{ik} \tau_L(u_j, u_k) + \langle \rho \rangle_l G_{jk} \tau_L(u_i, u_k) + \langle \rho \rangle_l C_0 \epsilon \delta_{ij},
\end{aligned} \tag{3.28a}$$

$$\begin{aligned}
& - 2\mu \left(\left\langle \frac{\partial u_i}{\partial x_j} \frac{\partial \phi_\alpha}{\partial x_j} \right\rangle_l - \frac{\partial \langle u_i \rangle_L}{\partial x_j} \frac{\partial \langle \phi_\alpha \rangle_l}{\partial x_j} \right) \\
& + \left[\left\langle \phi_\alpha \frac{\partial}{\partial x_j} \left(\mu \frac{\partial u_j}{\partial x_i} \right) \right\rangle_l - \langle \phi_\alpha \rangle_L \frac{\partial}{\partial x_j} \left(\mu \frac{\partial \langle u_j \rangle_l}{\partial x_i} \right) - (\langle \phi_\alpha \rangle_l - \langle \phi_\alpha \rangle_L) \frac{\partial}{\partial x_j} \left(\mu \frac{\partial \langle u_j \rangle_L}{\partial x_i} \right) \right] \\
& - \frac{2}{3} \left[\left\langle \phi_\alpha \frac{\partial}{\partial x_i} \left(\mu \frac{\partial u_j}{\partial x_j} \right) \right\rangle_l - \langle \phi_\alpha \rangle_L \frac{\partial}{\partial x_i} \left(\mu \frac{\partial \langle u_j \rangle_l}{\partial x_j} \right) - (\langle \phi_\alpha \rangle_l - \langle \phi_\alpha \rangle_L) \frac{\partial}{\partial x_i} \left(\mu \frac{\partial \langle u_j \rangle_L}{\partial x_j} \right) \right] \\
& - \tau_l \left(\phi_\alpha, \frac{\partial p}{\partial x_i} \right) = \langle \rho \rangle_l G_{ij} \tau_L(u_j, \phi_\alpha) - \langle \rho \rangle_l C_\phi \omega \tau_L(u_i, \phi_\alpha),
\end{aligned} \tag{3.28b}$$

$$\mu \tau_l \left(\frac{\partial \phi_\alpha}{\partial x_i}, \frac{\partial \phi_\beta}{\partial x_i} \right) = \langle \rho \rangle_l C_\phi \omega \tau_L(\phi_\alpha, \phi_\beta) - \mu \frac{\partial \langle \phi_\alpha \rangle_l}{\partial x_i} \frac{\partial \langle \phi_\beta \rangle_l}{\partial x_i}, \tag{3.28c}$$

where

$$\tau_l(a, b) = \langle ab \rangle_l - \langle a \rangle_l \langle b \rangle_l. \tag{3.29}$$

It is clear that the transport equations implied by the model 1 (M1) are consistent with the original LES equations without the conventional LES approximation for the diffusion terms (Eqs. (3.6), (3.8)). As indicated in Eq. (3.28c), in scalar covariance equation, there is a spurious source term which is negligible at high Reynolds number flows.

3.2.3.2 Model 2 (M2): In this model, the density fluctuations within the SGS are ignored.

$$dX_i^+ = U_i^+ dt + \sqrt{\frac{2\mu}{\langle \rho \rangle_l}} dW_i, \quad (3.30a)$$

$$dU_i^+ = \left[-\frac{1}{\langle \rho \rangle_l} \frac{\partial \langle p \rangle_l}{\partial x_i} + \frac{2\mu}{\langle \rho \rangle_l} \frac{\partial^2 \langle u_i \rangle_L}{\partial x_j \partial x_j} + \frac{\mu}{\langle \rho \rangle_l} \frac{\partial^2 \langle u_j \rangle_L}{\partial x_j \partial x_i} - \frac{2}{3} \frac{\mu}{\langle \rho \rangle_l} \frac{\partial^2 \langle u_j \rangle_L}{\partial x_i \partial x_j} \right] dt \\ + G_{ij} (U_j^+ - \langle u_j \rangle_L) dt + \sqrt{C_0 \epsilon} dW'_i + \sqrt{\frac{2\mu}{\langle \rho \rangle_l}} \frac{\partial \langle u_i \rangle_L}{\partial x_j} dW_j, \quad (3.30b)$$

$$d\phi_\alpha^+ = -C_{\phi\omega} (\phi_\alpha^+ - \langle \phi_\alpha \rangle_L) dt + S_\alpha (\phi^+) dt, \quad (3.30c)$$

where the parameters are defined in Eq. (3.23). The Fokker-Planck equation for $F_L(\mathbf{v}, \boldsymbol{\psi}, \mathbf{x}; t)$ corresponding to SDE in Eq. (3.30) is given by

$$\frac{\partial F_L}{\partial t} + \frac{\partial v_i F_L}{\partial x_i} = \frac{1}{\langle \rho \rangle_l} \frac{\partial \langle p \rangle_l}{\partial x_i} \frac{\partial F_L}{\partial v_i} - \frac{2\mu}{\langle \rho \rangle_l} \frac{\partial^2 \langle u_i \rangle_L}{\partial x_j \partial x_j} \frac{\partial F_L}{\partial v_i} - \frac{\mu}{\langle \rho \rangle_l} \frac{\partial^2 \langle u_j \rangle_L}{\partial x_i \partial x_j} \frac{\partial F_L}{\partial v_i} \\ + \frac{2}{3} \frac{\mu}{\langle \rho \rangle_l} \frac{\partial^2 \langle u_j \rangle_L}{\partial x_j \partial x_i} \frac{\partial F_L}{\partial v_i} - G_{ij} \frac{\partial [(v_j - \langle u_j \rangle_L) F_L]}{\partial v_i} + \mu \frac{\partial^2 (F_L / \langle \rho \rangle_l)}{\partial x_j \partial x_j} \\ + \frac{\partial}{\partial x_j} \left(\frac{2\mu}{\langle \rho \rangle_l} \frac{\partial \langle u_i \rangle_L}{\partial x_j} \frac{\partial F_L}{\partial v_i} \right) + \frac{\mu}{\langle \rho \rangle_l} \frac{\partial \langle u_i \rangle_L}{\partial x_k} \frac{\partial \langle u_j \rangle_L}{\partial x_k} \frac{\partial^2 F_L}{\partial v_i \partial v_j} + \frac{1}{2} C_0 \epsilon \frac{\partial^2 F_L}{\partial v_j \partial v_j} \\ + C_{\phi\omega} \frac{\partial [(\psi_\alpha - \langle \phi_\alpha \rangle_L) F_L]}{\partial \psi_\alpha} - \frac{\partial [S_\alpha(\boldsymbol{\psi}) F_L]}{\partial \psi_\alpha}. \quad (3.31)$$

The transport equations for the filtered variables are obtained by integration of Eq. (3.31) according to Eq. (3.16)

$$\frac{\partial \langle \rho \rangle_l}{\partial t} + \frac{\partial \langle \rho \rangle_l \langle u_j \rangle_L}{\partial x_j} = 0, \quad (3.32a)$$

$$\frac{\partial \langle \rho \rangle_l \langle u_i \rangle_L}{\partial t} + \frac{\partial \langle \rho \rangle_l \langle u_j \rangle_L \langle u_i \rangle_L}{\partial x_j} = -\frac{\partial \langle p \rangle_l}{\partial x_i} + \frac{\partial}{\partial x_j} \left(\mu \frac{\partial \langle u_i \rangle_L}{\partial x_j} \right) + \frac{\partial}{\partial x_j} \left(\mu \frac{\partial \langle u_j \rangle_L}{\partial x_i} \right) \\ - \frac{2}{3} \frac{\partial}{\partial x_i} \left(\mu \frac{\partial \langle u_j \rangle_L}{\partial x_j} \right) - \frac{\partial \langle \rho \rangle_l \tau_L(u_i, u_j)}{\partial x_j}, \quad (3.32b)$$

$$\frac{\partial \langle \rho \rangle_l \langle \phi_\alpha \rangle_L}{\partial t} + \frac{\partial \langle \rho \rangle_l \langle u_i \rangle_L \langle \phi_\alpha \rangle_L}{\partial x_i} = \frac{\partial}{\partial x_i} \left(\mu \frac{\partial \langle \phi_\alpha \rangle_L}{\partial x_i} \right) - \frac{\partial \langle \rho \rangle_l \tau_L(\phi_\alpha, u_i)}{\partial x_i} + \langle \rho \rangle_l \langle S_\alpha(\boldsymbol{\phi}) \rangle_L. \quad (3.32c)$$

The transport equations for the second order SGS moments are

$$\begin{aligned}
\frac{\partial \langle \rho \rangle_l \tau_L(u_i, u_j)}{\partial t} &+ \frac{\partial \langle \rho \rangle_l \langle u_k \rangle_L \tau_L(u_i, u_j)}{\partial x_k} = - \frac{\partial \langle \rho \rangle_l \tau_L(u_k, u_i, u_j)}{\partial x_k} + \frac{\partial}{\partial x_k} \left(\mu \frac{\partial \tau_L(u_i, u_j)}{\partial x_k} \right) \\
&- \langle \rho \rangle_l \tau_L(u_i, u_k) \frac{\partial \langle u_j \rangle_L}{\partial x_k} - \langle \rho \rangle_l \tau_L(u_j, u_k) \frac{\partial \langle u_i \rangle_L}{\partial x_k} \\
&+ \langle \rho \rangle_l G_{ik} \tau_L(u_j, u_k) + \langle \rho \rangle_l G_{jk} \tau_L(u_i, u_k) + \langle \rho \rangle_l C_0 \epsilon \delta_{ij}, \tag{3.33a}
\end{aligned}$$

$$\begin{aligned}
\frac{\partial \langle \rho \rangle_l \tau_L(u_i, \phi_\alpha)}{\partial t} &+ \frac{\partial \langle \rho \rangle_l \langle u_j \rangle_L \tau_L(u_i, \phi_\alpha)}{\partial x_j} = - \frac{\partial \langle \rho \rangle_l \tau_L(u_j, u_i, \phi_\alpha)}{\partial x_j} + \frac{\partial}{\partial x_j} \left(\mu \frac{\partial \tau_L(u_i, \phi_\alpha)}{\partial x_j} \right) \\
&- \langle \rho \rangle_l \tau_L(u_i, u_j) \frac{\partial \langle \phi_\alpha \rangle_L}{\partial x_j} - \langle \rho \rangle_l \tau_L(u_j, \phi_\alpha) \frac{\partial \langle u_i \rangle_L}{\partial x_j} \\
&+ \langle \rho \rangle_l G_{ij} \tau_L(u_j, \phi_\alpha) - \langle \rho \rangle_l C_\phi \omega \tau_L(u_i, \phi_\alpha) + \langle \rho \rangle_l \tau_L(u_i, S_\alpha(\phi)), \tag{3.33b}
\end{aligned}$$

$$\begin{aligned}
\frac{\partial \langle \rho \rangle_l \tau_L(\phi_\alpha, \phi_\beta)}{\partial t} &+ \frac{\partial \langle \rho \rangle_l \langle u_i \rangle_L \tau_L(\phi_\alpha, \phi_\beta)}{\partial x_i} = - \frac{\partial \langle \rho \rangle_l \tau_L(u_i, \phi_\alpha, \phi_\beta)}{\partial x_i} + \frac{\partial}{\partial x_i} \left(\mu \frac{\partial \tau_L(\phi_\alpha, \phi_\beta)}{\partial x_i} \right) \\
&- \langle \rho \rangle_l \tau_L(\phi_\alpha, u_i) \frac{\partial \langle \phi_\beta \rangle_L}{\partial x_i} - \langle \rho \rangle_l \tau_L(\phi_\beta, u_i) \frac{\partial \langle \phi_\alpha \rangle_L}{\partial x_i} + 2\mu \frac{\partial \langle \phi_\alpha \rangle_L}{\partial x_i} \frac{\partial \langle \phi_\beta \rangle_L}{\partial x_i} \\
&- 2 \langle \rho \rangle_l C_\phi \omega \tau_L(\phi_\alpha, \phi_\beta) + \langle \rho \rangle_l \tau_L(\phi_\alpha, S_\beta(\phi)) + \langle \rho \rangle_l \tau_L(\phi_\beta, S_\alpha(\phi)). \tag{3.33c}
\end{aligned}$$

The implied closure for the SDEs (3.30) is obtained by comparing the Fokker-Planck equation (3.31) to VSFMDf transport Eq. (3.20)

$$\begin{aligned}
&\frac{\partial}{\partial v_i} \left[\left\langle \frac{1}{\rho(\phi)} \frac{\partial p}{\partial x_i} \middle| \mathbf{v}, \boldsymbol{\psi} \right\rangle_l P_L \right] - \frac{\partial^2}{\partial v_i \partial v_j} \left[\left\langle \frac{\mu}{\rho(\phi)} \frac{\partial u_i}{\partial x_k} \frac{\partial u_j}{\partial x_k} \middle| \mathbf{v}, \boldsymbol{\psi} \right\rangle_l P_L \right] \\
&- \frac{\partial}{\partial v_i} \left[\left\langle \frac{1}{\rho(\phi)} \frac{\partial}{\partial x_j} \left(\mu \frac{\partial u_j}{\partial x_i} \right) \middle| \mathbf{v}, \boldsymbol{\psi} \right\rangle_l P_L \right] + \frac{\partial}{\partial v_i} \left[\left\langle \frac{1}{\rho(\phi)} \frac{\partial}{\partial x_i} \left(\frac{2}{3} \mu \frac{\partial u_j}{\partial x_j} \right) \middle| \mathbf{v}, \boldsymbol{\psi} \right\rangle_l P_L \right] \\
&- 2 \frac{\partial^2}{\partial v_i \partial \psi_\alpha} \left[\left\langle \frac{\mu}{\rho(\phi)} \frac{\partial u_i}{\partial x_j} \frac{\partial \phi_\alpha}{\partial x_j} \middle| \mathbf{v}, \boldsymbol{\psi} \right\rangle_l P_L \right] - \frac{\partial^2}{\partial \psi_\alpha \partial \psi_\beta} \left[\left\langle \frac{\mu}{\rho(\phi)} \frac{\partial \phi_\alpha}{\partial x_i} \frac{\partial \phi_\beta}{\partial x_i} \middle| \mathbf{v}, \boldsymbol{\psi} \right\rangle_l P_L \right] = \\
&\frac{1}{\langle \rho \rangle_l} \frac{\partial \langle p \rangle_l}{\partial x_i} \frac{\partial F_L}{\partial v_i} - \frac{2\mu}{\langle \rho \rangle_l} \frac{\partial^2 \langle u_i \rangle_L}{\partial x_j \partial x_j} \frac{\partial F_L}{\partial v_i} - \frac{\mu}{\langle \rho \rangle_l} \frac{\partial^2 \langle u_j \rangle_L}{\partial x_i \partial x_j} \frac{\partial F_L}{\partial v_i} \\
&+ \frac{2}{3} \frac{\mu}{\langle \rho \rangle_l} \frac{\partial^2 \langle u_j \rangle_L}{\partial x_j \partial x_i} \frac{\partial F_L}{\partial v_i} - G_{ij} \frac{\partial [(v_j - \langle u_j \rangle_L) F_L]}{\partial v_i} \\
&+ \frac{\partial}{\partial x_j} \left(\frac{2\mu}{\langle \rho \rangle_l} \frac{\partial \langle u_i \rangle_L}{\partial x_j} \frac{\partial F_L}{\partial v_i} \right) + \frac{\mu}{\langle \rho \rangle_l} \frac{\partial \langle u_i \rangle_L}{\partial x_k} \frac{\partial \langle u_j \rangle_L}{\partial x_k} \frac{\partial^2 F_L}{\partial v_i \partial v_j} + \frac{1}{2} C_0 \epsilon \frac{\partial^2 F_L}{\partial v_i \partial v_i} \\
&+ C_\phi \omega \frac{\partial [(\psi_\alpha - \langle \phi_\alpha \rangle_L) F_L]}{\partial \psi_\alpha}. \tag{3.34}
\end{aligned}$$

The set of Eqs. (3.32), (3.33) may be compared to Eqs. (3.10), (3.11). The closure at the second order level is

$$\begin{aligned}
& - 2\mu\tau_L \left(\frac{\partial u_i}{\partial x_k}, \frac{\partial u_j}{\partial x_k} \right) + \tau_L \left(u_j, \frac{\partial}{\partial x_k} \left(\mu \frac{\partial u_k}{\partial x_i} \right) \right) + \tau_L \left(u_i, \frac{\partial}{\partial x_k} \left(\mu \frac{\partial u_k}{\partial x_j} \right) \right) \\
& - \frac{2}{3}\tau_L \left(u_j, \frac{\partial}{\partial x_i} \left(\mu \frac{\partial u_k}{\partial x_k} \right) \right) - \frac{2}{3}\tau_L \left(u_i, \frac{\partial}{\partial x_j} \left(\mu \frac{\partial u_k}{\partial x_k} \right) \right) \\
& - \left(\left\langle u_j \frac{\partial p}{\partial x_i} \right\rangle_l - \langle u_j \rangle_L \frac{\partial \langle p \rangle_l}{\partial x_i} \right) - \left(\left\langle u_i \frac{\partial p}{\partial x_j} \right\rangle_l - \langle u_i \rangle_L \frac{\partial \langle p \rangle_l}{\partial x_j} \right) = \\
& \langle \rho \rangle_l G_{ik}\tau_L(u_j, u_k) + \langle \rho \rangle_l G_{jk}\tau_L(u_i, u_k) + \langle \rho \rangle_l C_0 \epsilon \delta_{ij}, \tag{3.35a}
\end{aligned}$$

$$\begin{aligned}
& - 2\mu\tau_L \left(\frac{\partial u_i}{\partial x_j}, \frac{\partial \phi_\alpha}{\partial x_j} \right) + \tau_L \left(\phi_\alpha, \frac{\partial}{\partial x_j} \left(\mu \frac{\partial u_j}{\partial x_i} \right) \right) - \frac{2}{3}\tau_L \left(\phi_\alpha, \frac{\partial}{\partial x_i} \left(\mu \frac{\partial u_j}{\partial x_j} \right) \right) \\
& - \left(\left\langle \phi_\alpha \frac{\partial p}{\partial x_i} \right\rangle_l - \langle \phi_\alpha \rangle_L \frac{\partial \langle p \rangle_l}{\partial x_i} \right) = \langle \rho \rangle_l G_{ij}\tau_L(u_j, \phi_\alpha) - \langle \rho \rangle_l C_{\phi\omega}\tau_L(u_i, \phi_\alpha), \tag{3.35b}
\end{aligned}$$

$$\mu\tau_L \left(\frac{\partial \phi_\alpha}{\partial x_i}, \frac{\partial \phi_\beta}{\partial x_i} \right) = \langle \rho \rangle_l C_{\phi\omega}\tau_L(\phi_\alpha, \phi_\beta) - \mu \frac{\partial \langle \phi_\alpha \rangle_L}{\partial x_i} \frac{\partial \langle \phi_\beta \rangle_L}{\partial x_i}. \tag{3.35c}$$

The stochastic model 2 (M2), as shown, results in a much more compact form for the moment transport equations which are also consistent with the conventional LES equations for variable-density flows (Eqs. (3.10), (3.11)).

3.3 NUMERICAL SOLUTION PROCEDURE

Numerical solution of the modeled VSFMDf transport equation is obtained by a hybrid finite-difference/Monte Carlo procedure. The basis is similar to those in RAS,^{58,59} in previous FDF simulations^{9–11} and in VSFDF simulations (Chapter 2), with some differences which are described here. For simulations, the FDF is represented by an ensemble of N_p statistically identical Monte Carlo (MC) particles. Each particle carries information pertaining to its position, $\mathbf{X}^{(n)}(t)$, velocity, $\mathbf{U}^{(n)}(t)$, and scalar value, $\phi^{(n)}(t)$, $n = 1, \dots, N_p$. This information

is updated via temporal integration of the SDEs. The simplest way of performing this integration is via Euler-Maruyama discretization.⁶⁰ For example, for Eq. (3.21a),

$$\begin{aligned} X_i^n(t_{k+1}) &= X_i^n(t_k) + (D_i^X(t_k))^n \Delta t + (B_{ij}^X(t_k))^n (\Delta t)^{1/2} (\zeta_j^X(t_k))^n \\ &+ (F_{ij}^{XU}(t_k))^n (\Delta t)^{1/2} (\zeta_j^U(t_k))^n + (F_{ij}^{X\phi}(t_k))^n (\Delta t)^{1/2} (\zeta_j^\phi(t_k))^n, \end{aligned} \quad (3.36)$$

where $D_i(t_k) = D_i(\mathbf{X}^{(n)}(t_k), \mathbf{U}^{(n)}(t_k), \boldsymbol{\phi}^{(n)}(t_k); t_k), \dots$, and $\zeta(t_k)$'s are independent standardized Gaussian random variables. This scheme preserves the Itô character of the SDEs.⁶¹

The computational domain is discretized on equally spaced finite-difference grid points. These points are used for three purposes: (1) to compute the pressure field, (2) to identify the regions where the statistical information from the MC simulations are obtained and (3) to perform a set of complementary LES primarily by the finite-difference methodology for assessing the consistency and convergence of the MC results. The LES procedure via the finite-difference discretization is referred to as LES-FD and will be further discussed below.

Statistical information is obtained by considering an ensemble of N_E computational particles residing within an ensemble domain of characteristic length Δ_E centered around each of the finite-difference grid points. This is illustrated schematically in Fig. 20. For reliable statistics with minimal numerical dispersion, it is desired to minimize the size of ensemble domain and maximize the number of the MC particles.⁴⁴ In this way, the ensemble statistics would tend to the desired filtered values:

$$\begin{aligned} \langle a \rangle_E &\equiv \frac{1}{N_E} \sum_{n \in \Delta_E} a^{(n)} \xrightarrow[N_E \rightarrow \infty]{\Delta_E \rightarrow 0} \langle a \rangle_L, \\ \tau_E(a, b) &\equiv \frac{1}{N_E} \sum_{n \in \Delta_E} (a^{(n)} - \langle a \rangle_E) (b^{(n)} - \langle b \rangle_E) \xrightarrow[N_E \rightarrow \infty]{\Delta_E \rightarrow 0} \tau_L(a, b), \end{aligned} \quad (3.37)$$

where $a^{(n)}$ denotes the information carried by n^{th} MC particle pertaining to transport variable a .

To reduce the computational cost, a procedure involving the use of non-uniform weights¹⁰ is also considered. This procedure allows a smaller number of particles in regions where a low degree of variability is expected. Conversely, in regions of high variability, a large number

of particles is allowed. It has been shown^{10,44} that the sum of weights within the ensemble domain is related to filtered fluid density as

$$\langle \rho \rangle_l \approx \frac{\Delta m}{V_E} \sum_{n \in \Delta_E} w^{(n)}, \quad (3.38)$$

where V_E is the volume of ensemble domain and Δm is the mass of particle with unit weight. The Favre-filtered value of a transport quantity $Q(\mathbf{v}, \phi)$ is constructed from the weighted average as

$$\langle Q \rangle_L \approx \frac{\sum_{n \in \Delta_E} w^{(n)} Q(\mathbf{v}^{(n)}, \phi^{(n)})}{\sum_{n \in \Delta_E} w^{(n)}}. \quad (3.39)$$

With uniform weights,⁴⁴ the particle number density decreases significantly in regions of low density such as reaction zone. The implementation of variable weight allows the increase in particle density without increasing the particle number density in these regions.

The LES-FD solver is based on the compact parameter finite-difference scheme.^{62,63} This is a variant of the MacCormack scheme in which fourth-order compact differencing schemes are used to approximate the spatial derivatives, and second-order symmetric predictor-corrector sequence is employed for time discretization. All of the finite-difference operations are conducted on fixed grid points. The transfer of information from the grid points to the MC particles is accomplished via a linear interpolation. The transfer of information from the particles to the grid points is accomplished via ensemble averaging as described above.

The LES-FD procedure determines the pressure field which is further used in the MC solver. The transport equations to be solved by the LES-FD solver include unclosed second order moments which are obtained from the MC solver. The LES-FD also determines the filtered velocity and scalar fields. That is, there is a “redundancy” in the determination of the first filtered moments as both the LES-FD and the MC procedures provides the solution of this field. This redundancy is actually very useful in monitoring the accuracy of the simulated results as described in Chapter 2 and in the previous works.^{10,11,58,59}

3.4 FLOWS SIMULATED

The following flow configurations are simulated:

1. A three-dimensional temporally developing mixing layer involving transport of a passive scalar variable.
2. A three-dimensional spatially developing mixing layer involving chemical reaction with non-premixed reactants.

The simulations (1) are used to assess the consistency and the overall capabilities of the VSFMDf methodology. These predictions are compared with data obtained by direct numerical simulation (DNS) of the same layer. The simulations (2) are performed to demonstrate the predictive capabilities of VSFMDf in reacting flows. The appraisal of these simulations is made by comparing with laboratory data. The predictions obtained from both stochastic models are compared in both simulations.

In the representation below, x , y and z denote the streamwise, the cross-stream, and the spanwise directions, respectively. The velocity components along these directions are denoted by u , v and w in the x , y and z directions, respectively. The temporal mixing layer consists of two parallel streams travelling in opposite directions with the same speed.^{64–66} Both the filtered streamwise velocity, scalar and temperature fields are initialized with a hyperbolic tangent profiles with $\langle u \rangle_L = 1$, $\langle \phi \rangle_L = 1$, $\langle T \rangle_L = 1$ on the top stream and $\langle u \rangle_L = -1$, $\langle \phi \rangle_L = 0$, $\langle T \rangle_L = 2$ on the bottom stream. The length L_v is specified such that $L_v = 2^{N_P} \lambda_u$, where N_P is the desired number of successive vortex pairings and λ_u is the wavelength of the most unstable mode corresponding to the mean streamwise velocity profile imposed at the initial time. The flow variables are normalized with respect to the half initial vorticity thickness, $L_r = \frac{\delta_v(t=0)}{2}$, ($\delta_v = \frac{\Delta U}{|\partial \langle u \rangle_L / \partial y|_{max}}$, where $\overline{\langle u \rangle_L}$ is the Reynolds-averaged value of the filtered streamwise velocity and ΔU is the velocity difference across the layer). The reference velocity is $U_r = \Delta U/2$.

The temporal simulations (1) are conducted for a cubic box, $0 \leq x \leq L$, $-\frac{L}{2} \leq y \leq \frac{L}{2}$, $0 \leq z \leq L$ where $L = L_v/L_r$. The 3D field is parameterized in a procedure somewhat similar to that by Vreman et al.⁶⁷ The formation of the large scale structures

are expedited through eigenfunction based initial perturbations.^{68,69} This includes two-dimensional^{65,67,70} and three-dimensional^{65,71} perturbations with a random phase shift between the 3D modes. This results in the formation of two successive vortex pairings and strong three-dimensionality.

The flow configuration in simulations (2) is similar to the one considered in the laboratory experiments of Mungal and Dimotakis⁷⁶. In these experiments, a heat-releasing reacting planar mixing layer consists of a low concentration of hydrogen (H_2) in one stream and a low concentration of fluorine (F_2) in the other stream. Both reactants are diluted in nitrogen (N_2) with the level of dilution determining the extent of heat release. The computational domain extends the region $54.8\text{ cm} \times 36.6\text{ cm} \times 4.6\text{ cm}$ in x , y and z directions, respectively, which covers the whole region considered experimentally including $x = 45.7\text{ cm}$ where the measured data are reported. In order to simulate a ‘naturally’ developing shear layer, a modified variant of the forcing procedure suggested in Ref.⁷⁷ is utilized. The cross-stream velocity component at the inlet is forced at the most unstable mode as well as four (sub- and super-) harmonics of this mode with a random phase shift. In these simulations, the variables are normalized by the values in the high-speed stream. The reference length $L_r = 45.7\text{ cm}$ which is the location in the experiment where the visual width of the layer is 7.4 cm .

3.5 REACTION MECHANISM

The chemical reaction considered in the spatially developing mixing layer simulations (2) involves reaction of hydrogen (H_2) and fluorine (F_2) as represented by Mungal and Dimotakis⁷⁶



where ΔQ is the heat of reaction. This reaction is sufficiently energetic that 1% of F_2 and 1% of H_2 in nitrogen will produce an adiabatic flame temperature of $93^\circ K$ above ambient. Thus, dilute concentrations produce significant temperature rise. The reaction actually consists of two second-order chain reactions with chemical times that are fast compared to the fluid mechanical timescales. Mungal and Dimotakis⁷⁶ indicate that for the conditions

of the experiment, the $H_2 - F_2$ mixture is in a stable region. Thus, for the chain reactions to proceed rapidly, it becomes crucial to provide some means to ensure the presence of F atoms. The technique used in the experiment consists of introducing a small amount of nitric oxide in the hydrogen reactant vessel. While it is necessary to add nitric oxide to initiate the reaction, the addition of excessive amounts would deplete the available F atoms. It was determined experimentally that by keeping the product of nitric oxide and fluorine concentrations at 0.03% the reactions would proceed rapidly. In this regard, it is important to note that the addition of 50% more nitric oxide showed no significant changes in the mean temperature profile. Thus, the chemistry can be considered to be relatively fast. This is also shown by Jaber et al.¹⁰ who considered both finite-rate and fast chemistry models and observed negligible differences. Therefore, the fast chemistry model is considered here.

3.6 NUMERICAL SPECIFICATIONS

Simulations are conducted on equally-spaced grid points. The temporal simulations (1), have grid spacings $\Delta x = \Delta y = \Delta z = \Delta$ with the number of grid points 193^3 and 33^3 for DNS and LES, respectively. In these simulations the Reynolds number is $Re = \frac{U_r L_r}{\nu} = 50$. To filter the DNS data, a top-hat function of the form below is used with $\Delta_L = 2\Delta$,

$$G(\mathbf{x}' - \mathbf{x}) = \prod_{i=1}^3 \tilde{G}(x'_i - x_i) \tag{3.41}$$

$$\tilde{G}(x'_i - x_i) = \begin{cases} \frac{1}{\Delta_L} & |x'_i - x_i| \leq \frac{\Delta_L}{2}, \\ 0 & |x'_i - x_i| > \frac{\Delta_L}{2}, \end{cases}$$

No attempt is made to investigate the sensitivity of the results to the filter function⁵¹ or the size of the filter.^{72,78,79}

The spatial simulations (2) are conducted on $81 \times 81 \times 12$ grid points in x , y and z directions, respectively. The LES filter size in these simulations is $\Delta_L = 2\Delta$ where $\Delta = (\Delta x \Delta y \Delta z)^{\frac{1}{3}}$.

A hyperbolic tangent profile is utilized to assign the velocity, scalar and temperature profiles initially for temporal simulations (1) and at the inlet for spatial simulations (2). The temporal simulations (1) are provided with periodic boundary conditions in homogeneous directions (x and z) and zero-derivative boundary condition in cross-stream direction. In spatial simulations (2), the characteristic boundary condition⁸⁰ is used at the inlet boundary. The pressure boundary condition⁸¹ is used at the outflow boundary and a zero-derivative boundary condition is implemented at cross-stream boundaries. The boundary condition at the spanwise boundaries is considered to be periodic.

All simulations are performed with variable particle weights.¹⁰ In temporal simulations, the MC particles are initially distributed throughout the computational region in a random fashion. Due to flow periodicity in the streamwise and spanwise directions, if the particle leaves the domain at one of these boundaries, new particles are introduced at the other boundary with the same velocity and compositional values. In the cross-stream directions, the free-slip boundary condition is satisfied by the mirror-reflection of the particles leaving through these boundaries. The particle weights are set according to filtered fluid density at the initial time. In spatial evolving mixing layer simulations, the MC particles are initially distributed within region $-0.15L_r \leq y \leq 0.15L_r$. In these simulations, the same spanwise boundary condition is employed for particles as in temporal simulations. At the cross-stream and streamwise boundaries, the leaving particles are disregarded and new particles are introduced at the inlet boundary at a rate according to the desired local particle number density and fluid velocity. The particle weights are set according to the local filtered fluid density at initial time and at the inlet, later on throughout the simulation. The composition and velocity components of the incoming particles are the same as those in the experiment, and consistent with those on LES grid points. The number of particles per grid point is $NPG = 320$ ($N_E = 40$) and the ensemble domain size (Δ_E) is set equal to half the grid spacing in each (x, y or z) direction. The effects of both of these parameters are assessed in the previous works⁹⁻¹¹ and in Chapter 2. All results are analyzed both “instantaneously” and “statistically.” In the former, the instantaneous contours (snap-shots) and scatter plots of the variables of interest are analyzed. In the latter, the “Reynolds-averaged” statistics constructed from the instantaneous data are considered. These are constructed by spa-

tial averaging over homogeneous directions (x and z) in temporal simulations and by time averaging in spatial simulations. All Reynolds-averaged results are denoted by an overbar.

No attempt is made to determine the appropriate values of the model constants; the values suggested in the literature are adopted⁷³ $C_0 = 2.1$, $C_\epsilon = 1$ and $C_\phi = 1$. The influence of these parameters are assessed in Chapter 2. The values of $Sc (=Pr)$ are 1 in all simulations.

3.7 CONSISTENCY ASSESSMENTS

The objective of this section is to demonstrate the consistency of the VSFMDf formulation. Since the accuracy of the LES-FD procedure is well-established (at least for the first order filtered quantities), such a comparative assessment provides a good means of assessing the performance of the MC solution. For obvious reasons, this assessment is done via M2. Figure 21 shows the instantaneous contour plots of the filtered scalar field in temporal mixing layer simulations at $t = 80$ as obtained by LES-FD and MC. This figure provides a visual demonstration of the consistency of the VSFMDf.

The uniformity of the MC particles is checked by monitoring their distributions at all times. The normalized particle number density must vary around unity while the particle weight density should be close to filtered fluid density. The Reynolds-averaged density field as obtained by both LES-FD and MC are shown in Fig. 22. Close to unity values for the particle number density at all times is the first measure of the accuracy of the simulations. As also depicted, the particle weight density (see Eq. (3.38)) and the MC density, defined as

$$\langle \rho \rangle^{MC} \equiv \left(\frac{\sum_{n \in \Delta_E} w^{(n)} (RT^{(n)} / \langle p \rangle_l)}{\sum_{n \in \Delta_E} w^{(n)}} \right)^{-1} \quad (3.42)$$

are in very good agreements with the filtered density obtained from LES-FD.

The consistency is observed for all first order moments. As Fig. 23 shows, the cross-stream variation of filtered scalar is consistently predicted by LES-FD and MC. The same consistency is also observed for all other first moments. The first moments show very little dependence on the values of Δ_E and N_E consistent with previous FDF simulations^{9-11,82} and those in Chapter 2. The consistency of the second order scalar correlation is also shown in

Fig. 23. As depicted, the predictions via MC show close agreements with LES-FD. With N_E and Δ_E chosen, this demonstration is consistent with previous assessment studies.⁹⁻¹¹ All other second order SGS moments behave similarly. In addition, Fig. 23 shows a comparison of the two stochastic models M1 and M2. As shown, the differences are insignificant.

Complementary consistency assessments are obtained by presenting the scatter plots of instantaneous results obtained from LES-FD and MC. The MC density as given by Eq. (3.42) is highly correlated with the fluid filtered density, as Fig. 24 shows. Figure 25 shows the scatter plots of the velocity components. For all these quantities, there is a high level of correlation between LES-FD and MC results. In Fig. 26, the consistency of the passive scalar field is demonstrated. The highly scattered data points along the horizontal axis is an indication of relatively high numerical oscillations in LES-FD results. In addition, while the LES-FD scalar field violates the realizability condition for the filtered scalar field, the MC predictions are always bounded between 0, 1 (without using any additional limiter). The satisfaction of realizability condition is of primary importance when finite-rate chemistry models are employed. For all the first order moments the linear regression line almost coincides with the 45° line. The scatter plot of scalar correlation is also shown in Fig. 26. As shown, the scalar variance shows increased statistical variations and hence, a decreased correlation coefficient. The high level of correlations for all these quantities further establishes the consistency of VSFMDf methodology.

3.8 VALIDATION VIA DNS

The objective of this section is to analyze some of the characteristics of the VSFMDf via comparative assessments against DNS of a three-dimensional temporal mixing layer. In addition, comparisons are also made with LES via the “conventional” Smagorinsky^{42,74} model

$$\begin{aligned}\tau_L(u_i, u_j) &= -2 \nu_t (S_{ij} - \frac{1}{3} S_{kk} \delta_{ij}) + \frac{2}{3} k \delta_{ij}, \\ \tau_L(u_i, \phi) &= -\Gamma_t \frac{\partial \langle \phi \rangle_L}{\partial x_i},\end{aligned}\tag{3.43}$$

where

$$S_{ij} = \frac{1}{2} \left(\frac{\partial \langle u_i \rangle_L}{\partial x_j} + \frac{\partial \langle u_j \rangle_L}{\partial x_i} \right), \quad (3.44)$$

$$\nu_t = C_\nu \Delta_L^2 S, \quad \Gamma_t = \frac{\nu_t}{Sc_t},$$

$C_\nu = 0.04$, $Sc_t = 1$, $S = \sqrt{S_{ij}S_{ij}}$ and Δ_L is the characteristic length of the filter. The isotropic part of SGS stress is expressed using Yoshizawa's⁸³ expression

$$k = C_I \Delta_L^2 S^2. \quad (3.45)$$

The Yoshizawa's constant of $C_I = 0.18$ is adopted from the dynamic simulations of Moin et al.⁸⁴

For comparison, the DNS data are filtered from the original high resolution 193^3 points to the coarse 33^3 points. In the comparisons, we also consider the “resolved” and the “total” components of the Reynolds-averaged moments. The former are denoted by $\overline{R(a, b)}$ with $R(a, b) = \left(\langle a \rangle_L - \overline{\langle a \rangle_L} \right) \left(\langle b \rangle_L - \overline{\langle b \rangle_L} \right)$; and the latter is $\overline{r(a, b)}$ with $r(a, b) = (a - \bar{a})(b - \bar{b})$. In DNS, the “total” components are directly available, while in LES they are approximated by $\overline{r(a, b)} \approx \overline{R(a, b)} + \overline{\tau_L(a, b)}$.⁶⁷

Figure 27 shows the instantaneous iso-surface of the $\langle \phi \rangle_L$ field at $t = 80$. By this time, the flow is going through pairings and exhibits strong 3D effects. This is evident by the formation of large scale spanwise rollers with the presence of secondary structures in streamwise planes,⁶⁸ as also illustrated in Figs. 28-31. These figures show the vorticity and the scalar fields obtained from DNS, VSF MDF, Smagorinsky on planes in spanwise and streamwise directions. As Figs. 28, 29 show, the two neighboring rollers are being paired and in Figs. 30, 31, the formation of secondary structures are evident. As illustrated in these figures and consistent with the results presented in Chapter 2 and also in the previous works,^{11,67} the results obtained from Smagorinsky closure are overly smooth. This is due to the excessive amount of SGS diffusion with the Smagorinsky model. As shown, there is a more resemblance in the structures predicted by VSF MDF and DNS. The Reynolds-averaged values of the filtered temperature field at $t = 80$ are shown in Fig. 32, The filtered and unfiltered DNS data yield virtually indistinguishable results. The Smagorinsky model underpredicts the spread of the layer due to dissipative nature of this model. All VSF MDF

predictions compare well with DNS data in predicting the spread of the layer. This is also evident in Fig. 33. This figure shows the temporal variation of the momentum thickness of the layer and the “scalar thickness” defined as

$$\delta_s(t) = |y(\overline{\langle\phi\rangle}_L = 0.9)| + |y(\overline{\langle\phi\rangle}_L = 0.1)|. \quad (3.46)$$

Several components of the Reynolds-averaged values of the second order SGS moments are compared with DNS data in Figs. 34, 35. In general, the VSF MDF results are in better agreement with DNS data than those predicted by the Smagorinsky model. In this configuration, there are no strong velocity and scalar gradients in the streamwise and spanwise directions and, thus, a gradient-diffusion type model such as Smagorinsky is not capable of providing correct prediction of scalar flux values in these directions. Consequently, the VSF MDF is expected to be more effective for LES of reacting flows provided that the extent of SGS mixing is heavily influenced by these SGS moments.^{5,75}

Several components of the resolved second order moments are presented in Figs. 36, 37. As expected, the performance of the Smagorinsky model is not satisfactory as it does not predict the spread and peak values accurately. The VSF MDF provides more reasonable predictions. The “total” components also yield very good agreement with DNS data as shown in Figs. 38, 39. It is important to note that (as also observed in the VSF DF predictions in Chapter 2 and in Ref.¹¹) the “total” components predicted by VSF MDF are almost insensitive to the model parameters. This is pleasing since we are primarily interested in predicting the total field (for comparison with experimental data, *etc.*). Obviously, the values cannot be set in such a way that the contribution of the SGS components to the total components becomes too large. As all these figures demonstrate, models M1 and M2 yield very close predictions.

With the constant values chosen for VSF MDF, while the SGS scalar flux in cross-stream direction predicted by Smagorinsky is in closer agreement with DNS data, VSF MDF yields much more accurate prediction of the resolved field and, hence, the total field is predicted much more accurately by VSF MDF.

3.9 VALIDATION VIA LABORATORY DATA

The three-dimensional spatially developing mixing layer simulations (2) are consistent with the experimental studies of Mungal and Dimotakis⁷⁶. These experiments are conducted with several values of equivalence ratio, defined as $\phi = c_{02}/c_{01}$ where c_{01} and c_{02} denote the high- and low-speed stream mole fractions, respectively. In the current simulations, the equivalence ratios of $\phi = 1, 2, 4$ are considered by keeping F_2 concentration at 1% and varying the H_2 concentration from 1% to 2% and 4%. In addition, the flip experiments are also considered in which the low- and high-speed compositions are simply switched to attain the inverse equivalence ratios ($\phi = 1, \frac{1}{2}, \frac{1}{4}$). These simulations are performed using VSFMD. The implementation of DNS and LES-FD are not possible for this flow.

The results are compared to the experimental results both qualitatively and quantitatively. Figure 40 shows the instantaneous temperature field as obtained by LES-FD and VSFMD. The resemblance of the structures in these figures, is an indication of the consistency of these simulations. The three-dimensionality of the flow in spatially developing mixing layer simulations is evident by the presence of primary and secondary structures, as shown in Fig. 41. This figure shows the contour surfaces of the instantaneous filtered scalar field.

The time series of the filtered temperature field recorded by 15 probes across the layer, are shown in Fig. 42. These probes are located at $x = 45.7 \text{ cm}$ downstream and are symmetrically distributed in cross-stream direction about the centerline with the vertical distance of 0.457 cm between each two. The high-speed stream located on top and carries 1% H_2 and the low-speed stream is in the bottom with 1% F_2 composition. In this figure, the horizontal axis corresponds to the non-dimensional time starting at one flow-through time. The vertical axis for each section represents the temperature ranging from the ambient to the maximum temperature recorded by each probe (denoted as T_{max}). Several features observed experimentally⁷⁶ are also present in these time series, namely: the presence of large, hot structures; the cold regions extending deep into the layer and the near-uniformity of temperature within the structure. The non-uniformity of temperatures in the simulations by Jaber et al.¹⁰ was attributed to the lack of proper small-scale mixing due to two-dimensionality of

their simulations. The present simulations substantiate this, as the more effective small-scale mixing in three-dimensional simulations tends to make the temperature more uniform inside the structures.

Figure 43 shows a comparison of VSFMDf predictions with the experimental data. In this figure, the time-averaged filtered temperature profile corresponding to the case with equivalence ratio $\phi = 1$ is compared with the experimental data. The predictions from both stochastic models M1 and M2 are presented. As this figure shows, both peak value of the temperature profile and the spread of the layer are very well predicted and the two stochastic models give very close results. The peak value of the time-averaged temperature profile is lower than the adiabatic flame temperature, as also indicated in Ref.⁷⁶

The flip experiment predictions also demonstrate the same features as the laboratory observations. The time-averaged filtered temperature profiles in these predictions are integrated along the cross-stream direction to obtain the product thicknesses, as defined in the experiment:⁷⁶

$$\delta_{P1} = \int_{-\infty}^{+\infty} \frac{C_p \overline{\langle T \rangle}_L}{c_{01} \Delta Q} dy, \quad \delta_{P2} = \int_{-\infty}^{+\infty} \frac{C_p \overline{\langle T \rangle}_L}{c_{02} \Delta Q} dy, \quad (3.47)$$

where C_p is the molar heat capacity of the carrier gas and ΔQ is the amount of heat release per mole of the reactant. Figure 44 shows the comparison of product thicknesses obtained from VSFMDf with the experiment data. Consistent with the experiment, the 1% thickness δ_1 is used to normalize the product thicknesses. The 1% thickness is defined as the distance at which the mean temperature rise is equal to 1% of the maximum mean temperature. In the experiment, a mean value of $\delta_1/(x - x_0) = 0.165$ (where $x - x_0 = 45.7 \text{ cm}$) is used to normalize all the product thicknesses. As shown in this figure, at low equivalence ratios, the product thicknesses vary almost linearly with the equivalence ratio, as the low-speed reactant reacts with excessive amount of high-speed reactant. At high equivalence ratios, the product thicknesses reach to asymptotic limits. These limits correspond to reaction of high-speed reactant with excessive amount of low-speed reactant. As a result, the amount of product shows little increase with the equivalence ratio. As shown in this figure, the VSFMDf predictions compare reasonably well with the experimental data.

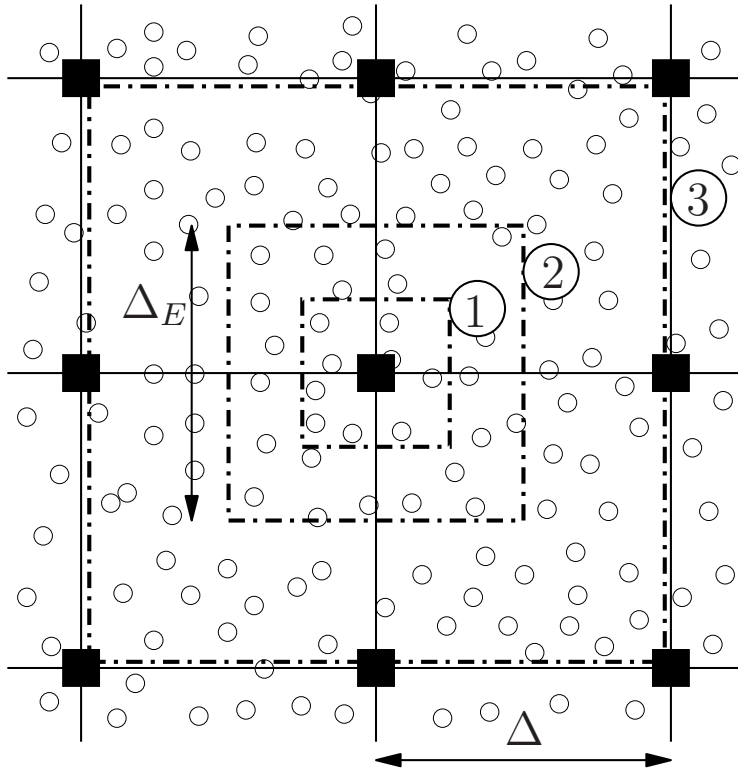


Figure 20: Concept of ensemble averaging. Shown are three different ensemble domains: $1(\Delta_E = \Delta/2)$, $2(\Delta_E = \Delta)$, $3(\Delta_E = 2\Delta)$. Black squares denote the finite-difference grid points, and the circles denote the MC particles.

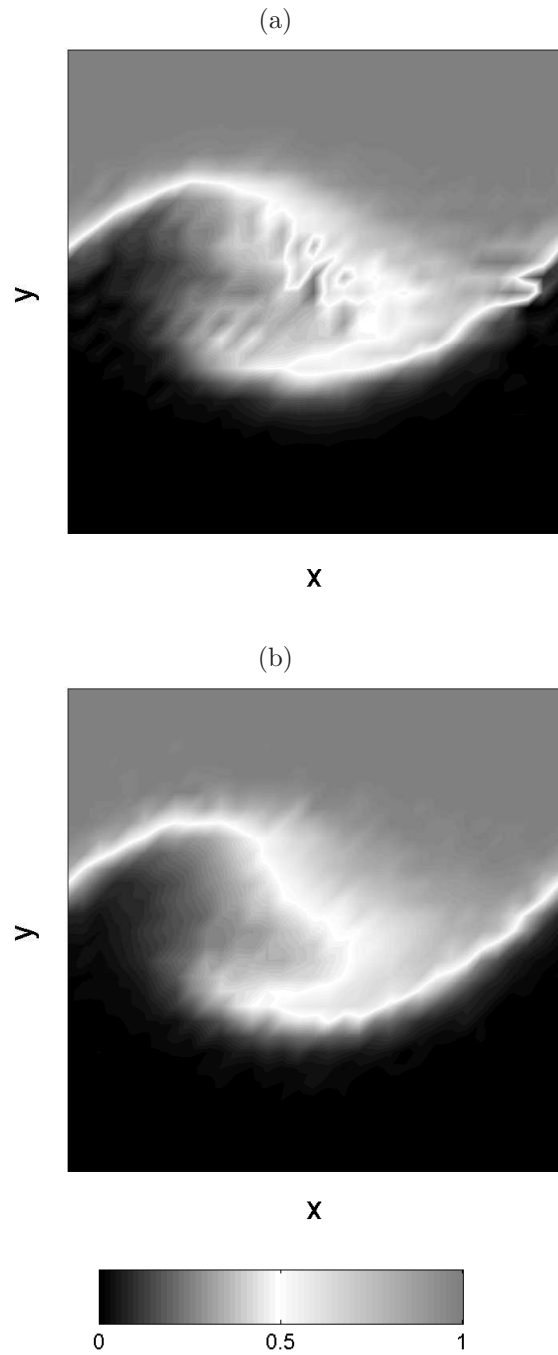


Figure 21: Contours of the instantaneous filtered scalar field as obtained by: (a) LES-FD, (b) MC.

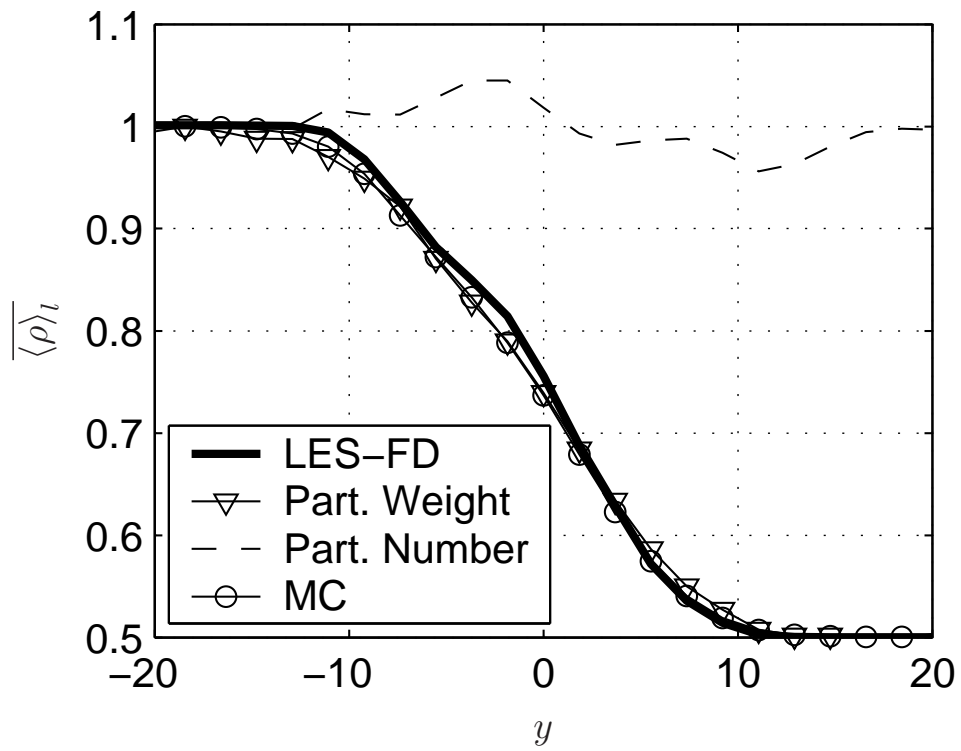


Figure 22: Cross-stream variations of the filtered density in the three-dimensional temporal mixing layer obtained from LES-FD and MC using M1 at $t = 60$.

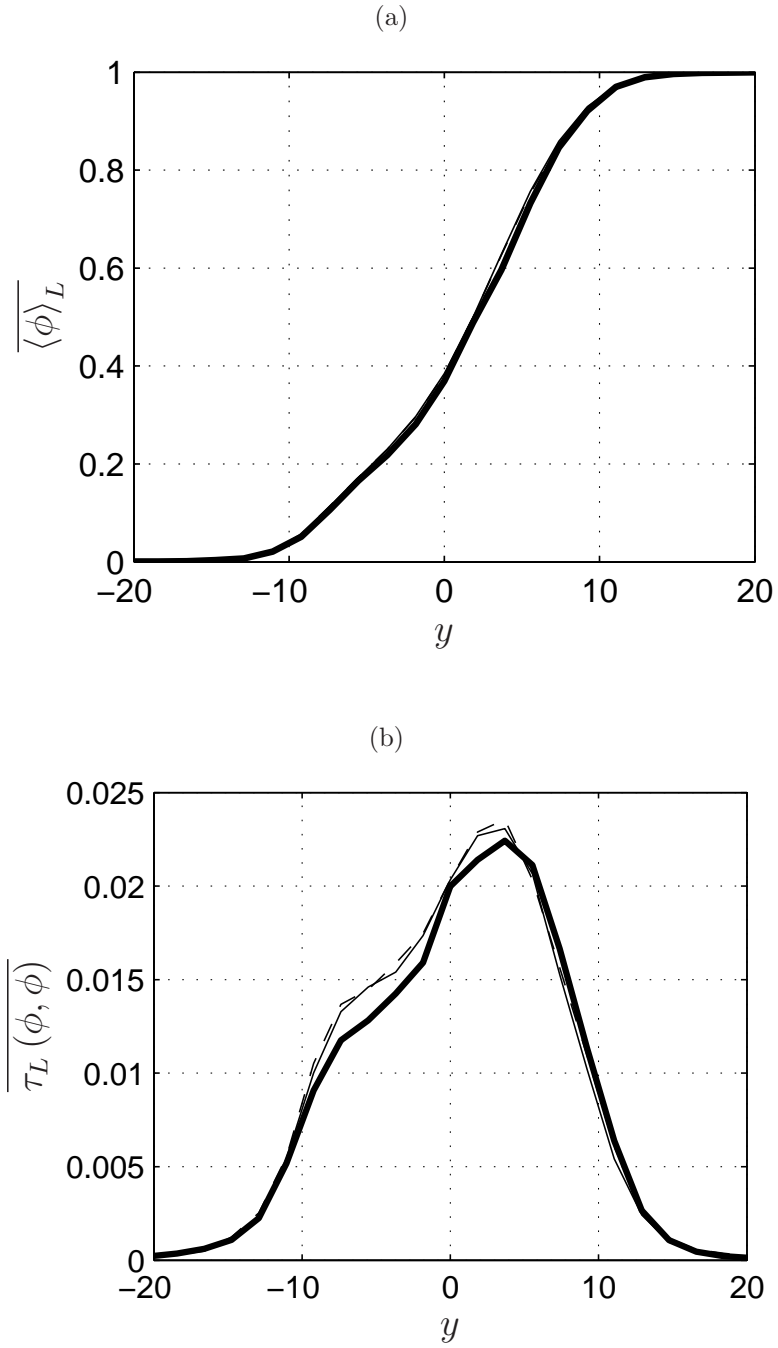


Figure 23: Cross-stream variations of the Reynolds-averaged values of (a) $\langle \phi \rangle_L$, (b) $\tau_L(\phi, \phi)$. The thick solid line denotes LES-FD predictions. The thin solid and dashed lines denote MC predictions via M1 and M2, respectively.

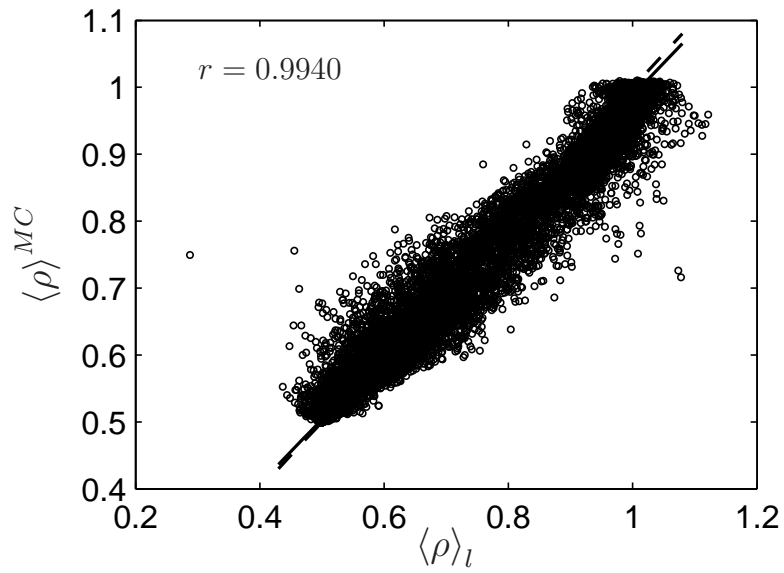


Figure 24: Scatter plots of density obtained at $t = 60$ from LES-FD ($\langle \rho \rangle_t$) and MC density ($\langle \rho \rangle^{MC}$, as given in Eq. (3.42)). The solid and dashed lines denote the linear regression and 45° lines, respectively. The parameter r denotes the correlation coefficient.

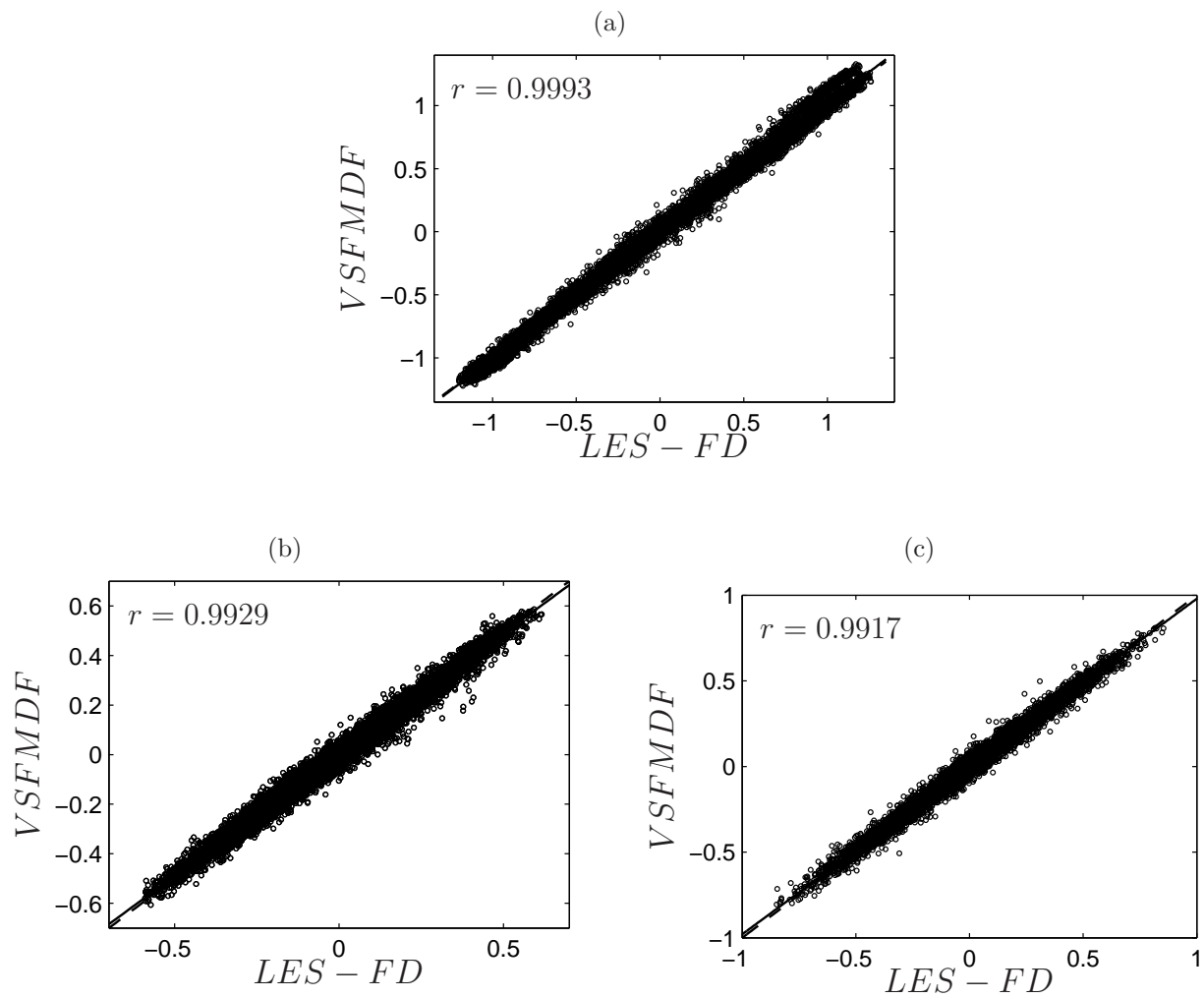


Figure 25: Scatter plots of velocity components at $t = 80$. (a) $\langle u \rangle_L$, (b) $\langle v \rangle_L$ and (c) $\langle w \rangle_L$. The solid and dashed lines denote the linear regression and 45° lines, respectively. The parameter r denotes the correlation coefficient.

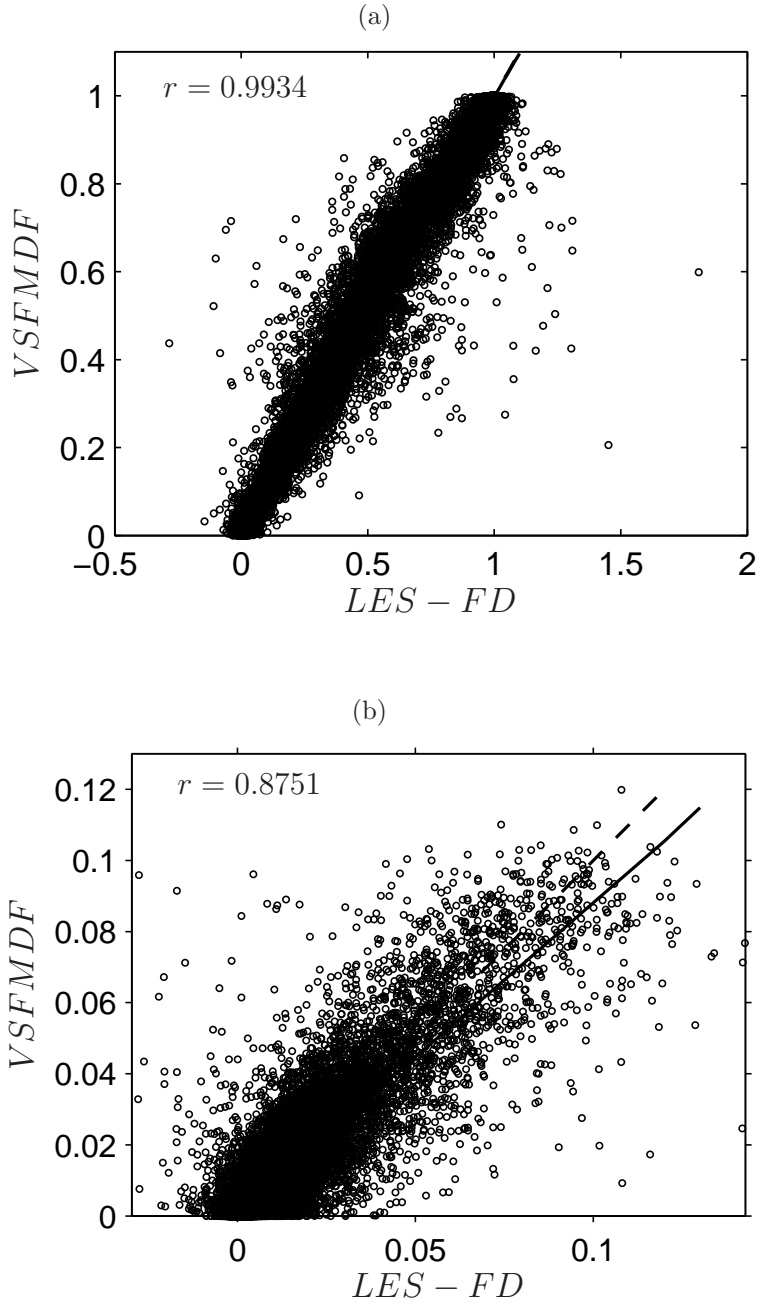


Figure 26: Scatter plots of scalar statistics at $t = 80$. (a) $\langle \phi \rangle_L$, (b) $\tau_L(\phi, \phi)$. The solid and dashed lines denote the linear regression and 45° lines, respectively. The parameter r denotes the correlation coefficient.

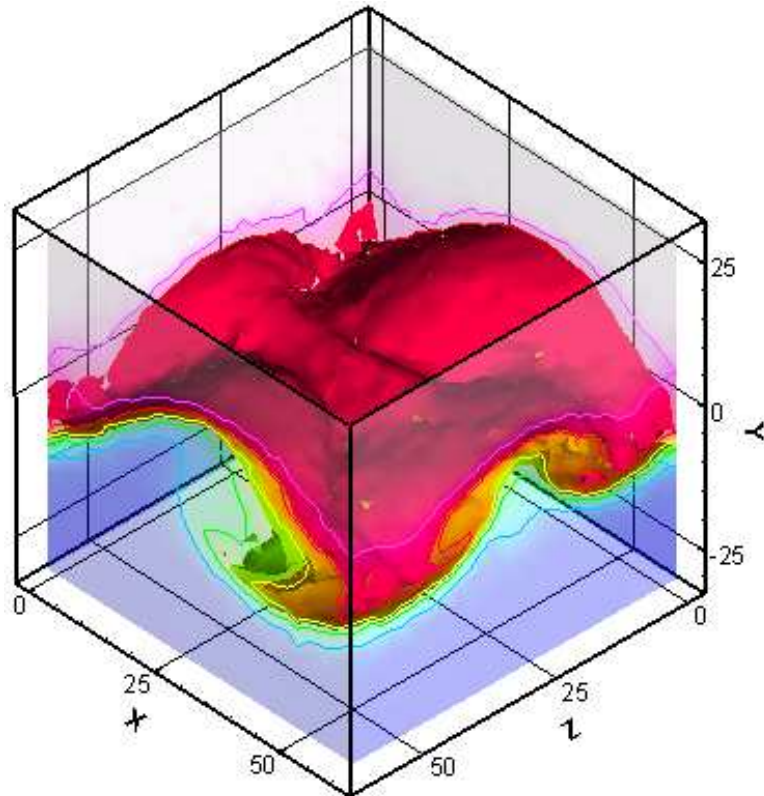


Figure 27: Contour surfaces of the instantaneous $\langle \phi \rangle_L$ field in the 3D mixing layer at $t = 80$ as obtained by VSFMDP.

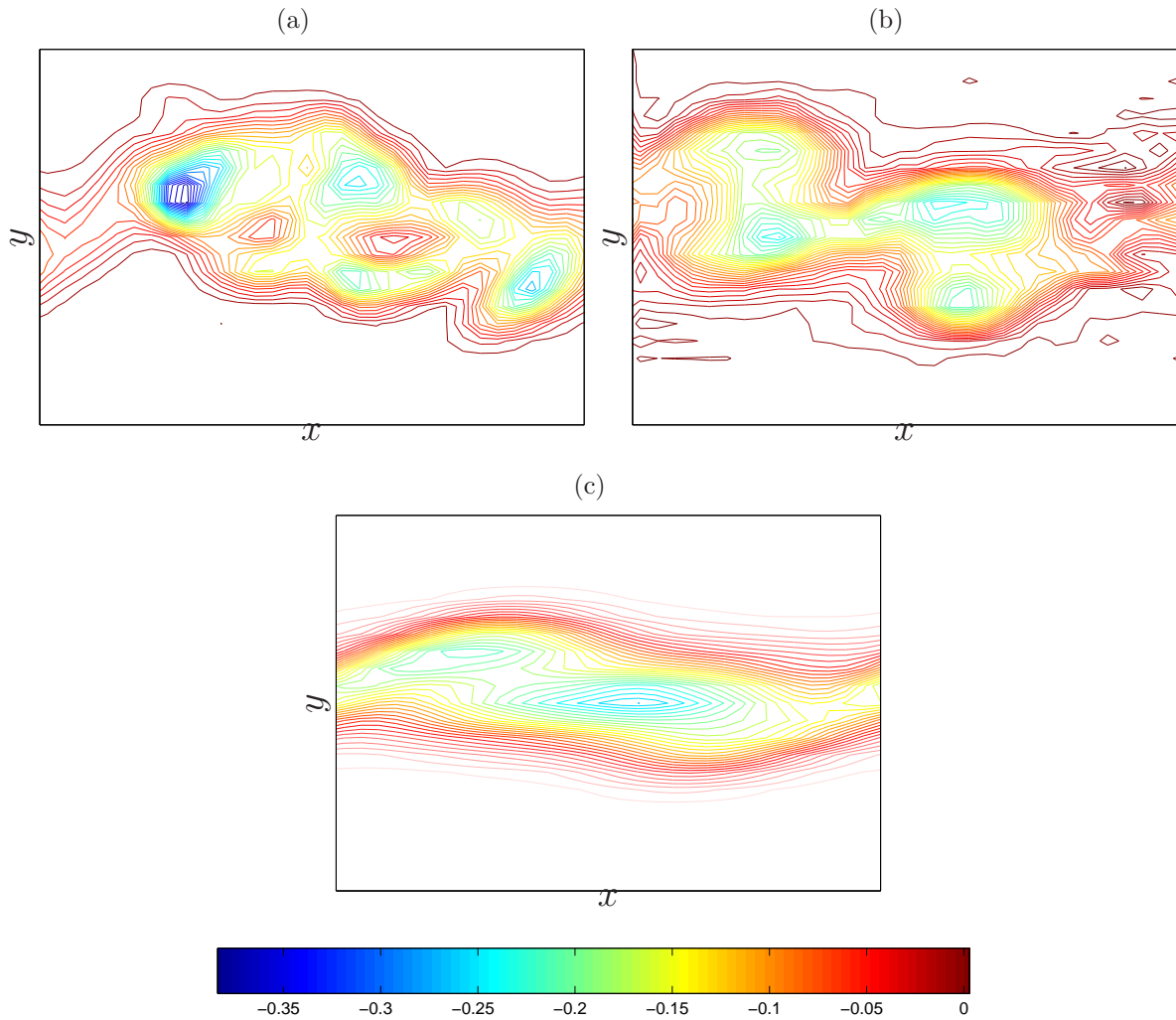


Figure 28: Contour plots of the spanwise vorticity field at $z = 0.75 L$, $t = 80$ in the 3D temporal mixing layer as obtained by: (a) DNS, (b) VSF MDF, (c) Smagorinsky.

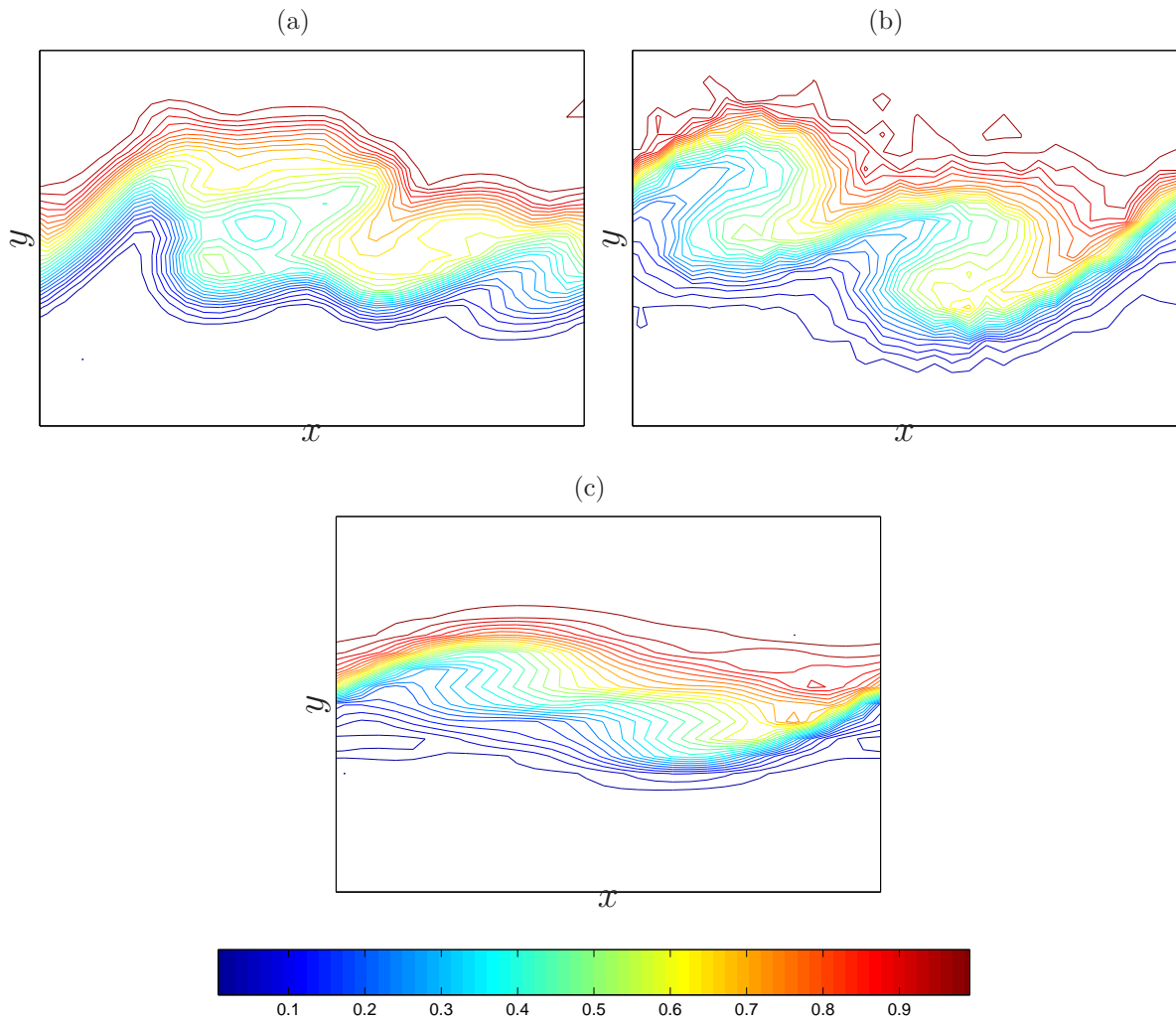


Figure 29: Contour plots of $\langle \phi \rangle_L$ field on spanwise plane at $z = 0.75 L$, $t = 80$ in the 3D temporal mixing layer as obtained by: (a) DNS, (b) VSF MDF, (c) Smagorinsky.

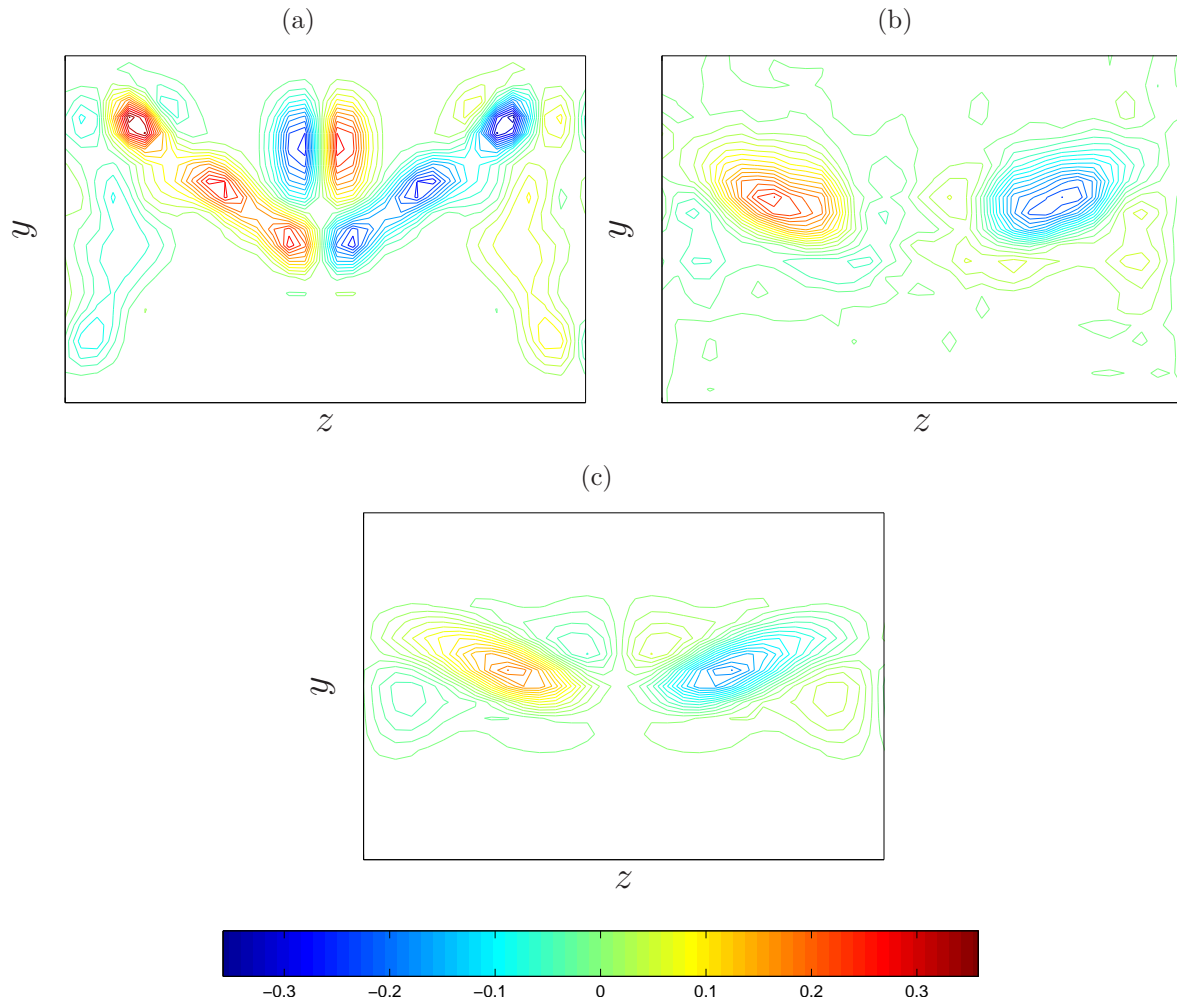


Figure 30: Contour plots of the streamwise vorticity field at $x = 0.25 L$, $t = 80$ in the 3D temporal mixing layer as obtained by: (a) DNS, (b) VSF MDF, (c) Smagorinsky.

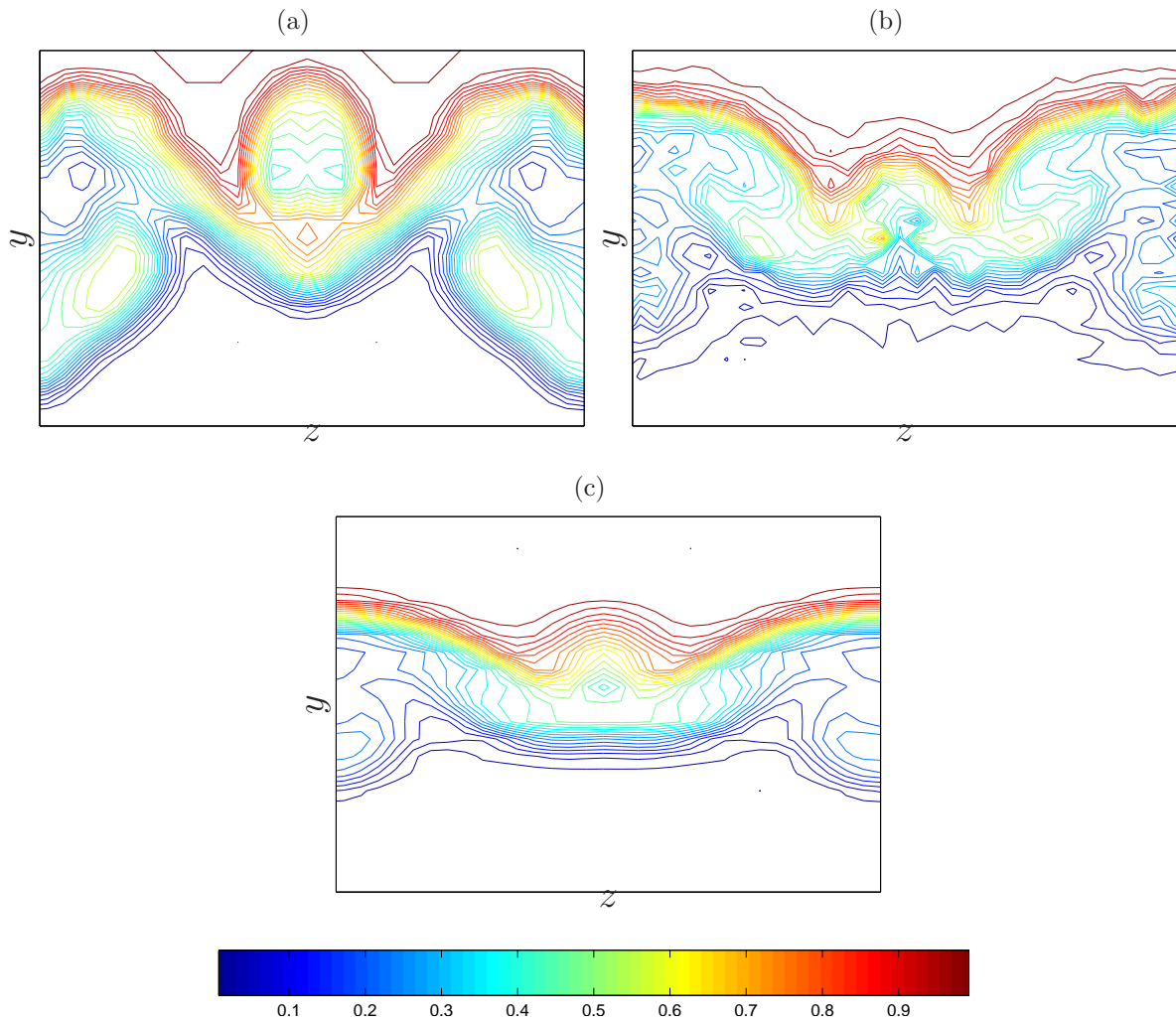


Figure 31: Contour plots of $\langle \phi \rangle_L$ field on streamwise plane at $x = 0.25 L$, $t = 80$ in the 3D temporal mixing layer as obtained by: (a) DNS, (b) VSF MDF, (c) Smagorinsky.

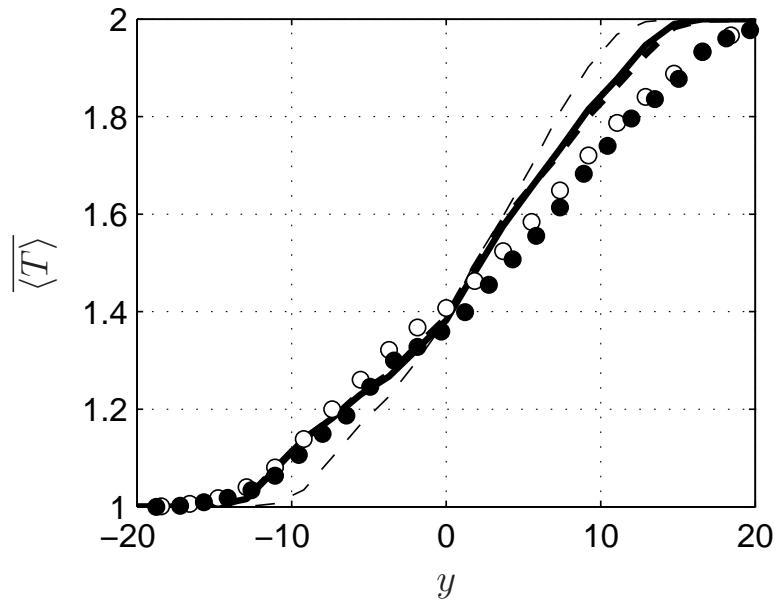


Figure 32: Cross-stream variations of the Reynolds-averaged values of the filtered temperature field at $t = 80$. The thick solid and dashed lines denote VSFMDF predictions via M1 and M2, respectively. The thin dashed line denote the predictions using Smagorinsky closure. The white and black circles show the filtered and unfiltered DNS data, respectively.

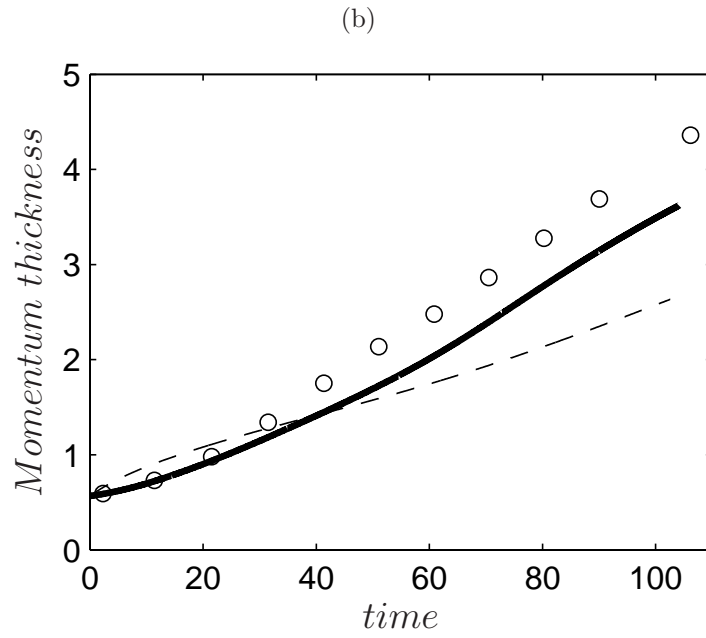
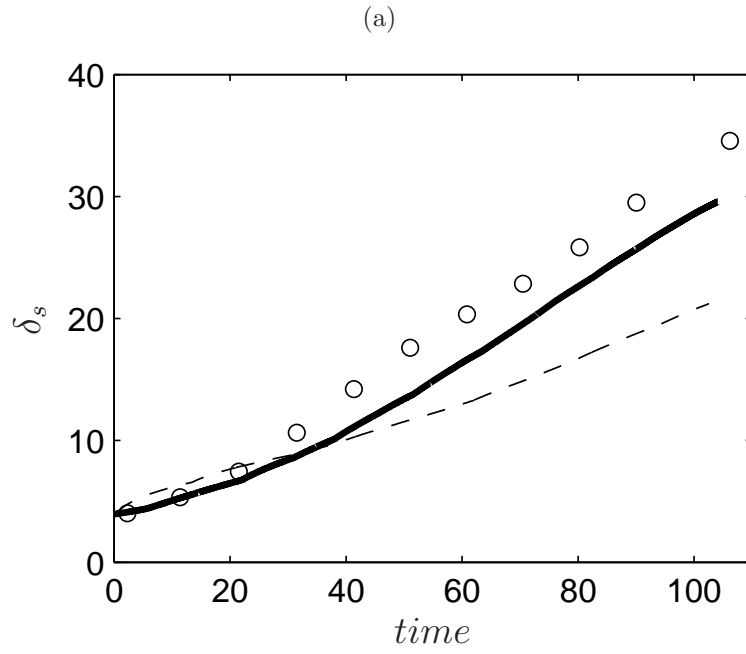


Figure 33: Temporal variation of (a) scalar thickness (δ_s), (b) momentum thickness. The solid and dashed lines denote predictions via VSF MDF (M1) and Smagorinsky closures, respectively. The circles show the filtered DNS data.

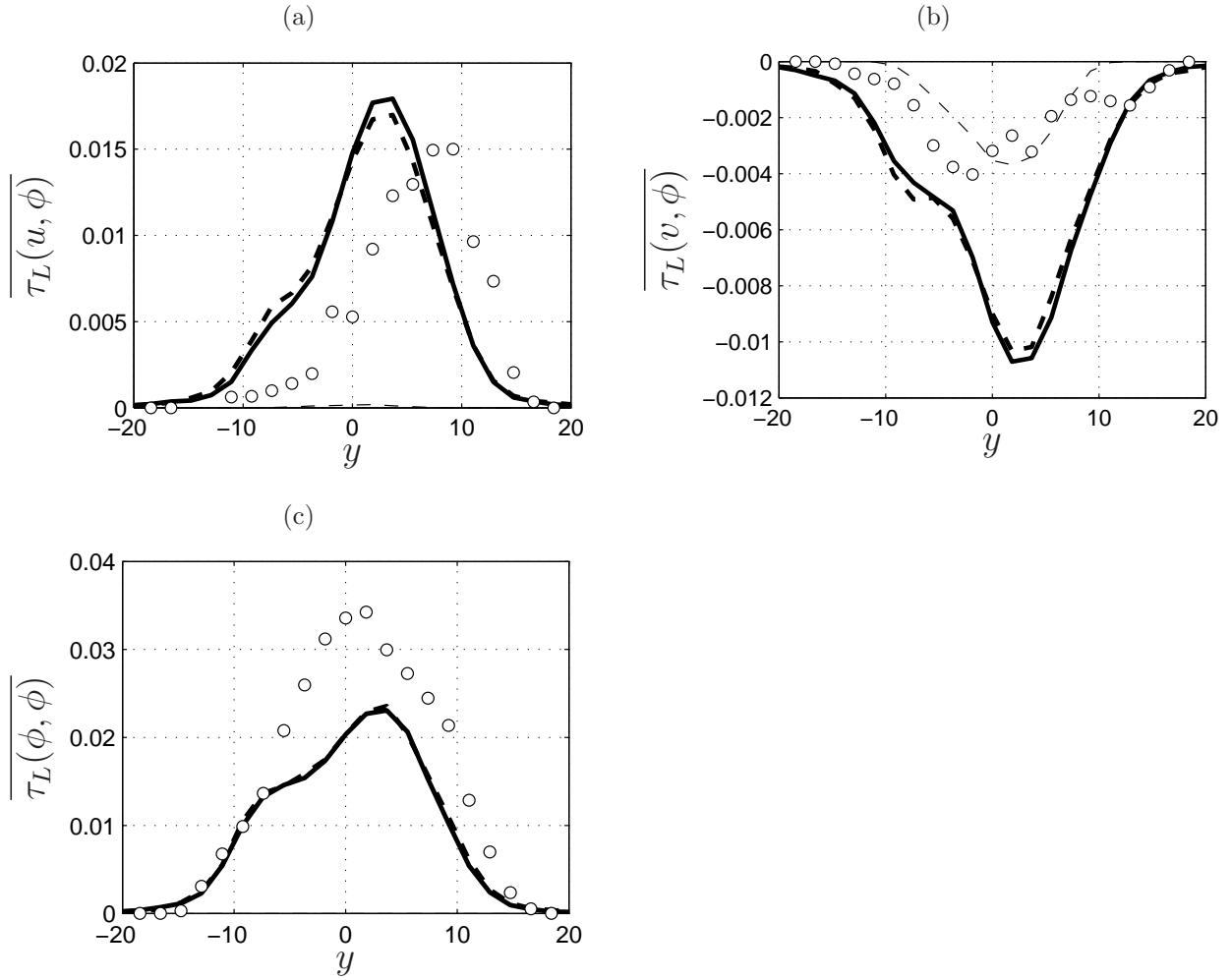


Figure 34: Cross-stream variations of some of the Reynolds-averaged components of τ_L at $t = 60$. The thick solid and dashed lines denote VSFMDF predictions via M1 and M2, respectively. The thin dashed line denote the predictions using Smagorinsky closure. The circles show the filtered DNS data.

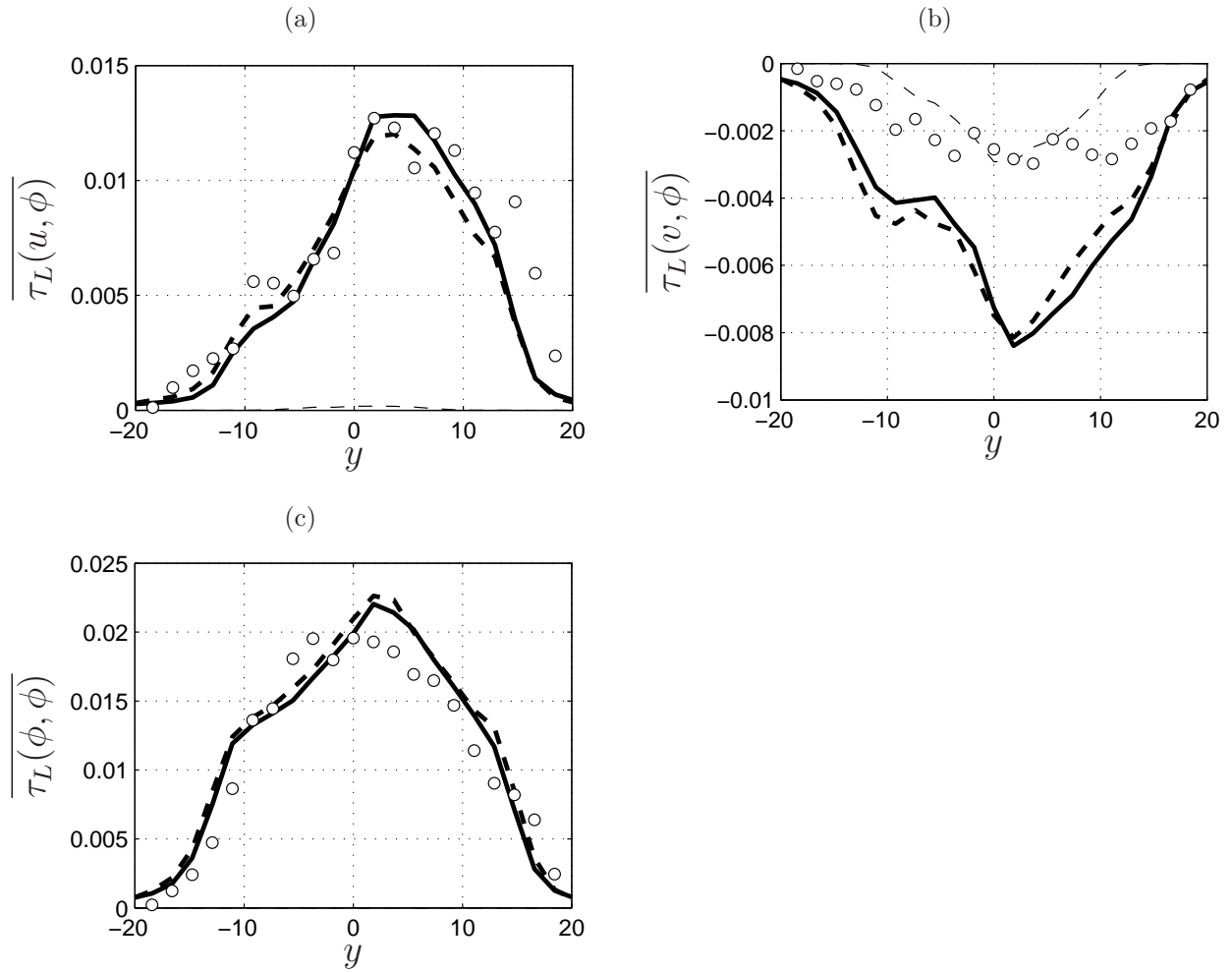


Figure 35: Cross-stream variations of some of the Reynolds-averaged components of τ_L at $t = 80$. The thick solid and dashed lines denote VSF MDF predictions via M1 and M2, respectively. The thin dashed line denote the predictions using Smagorinsky closure. The circles show the filtered DNS data.

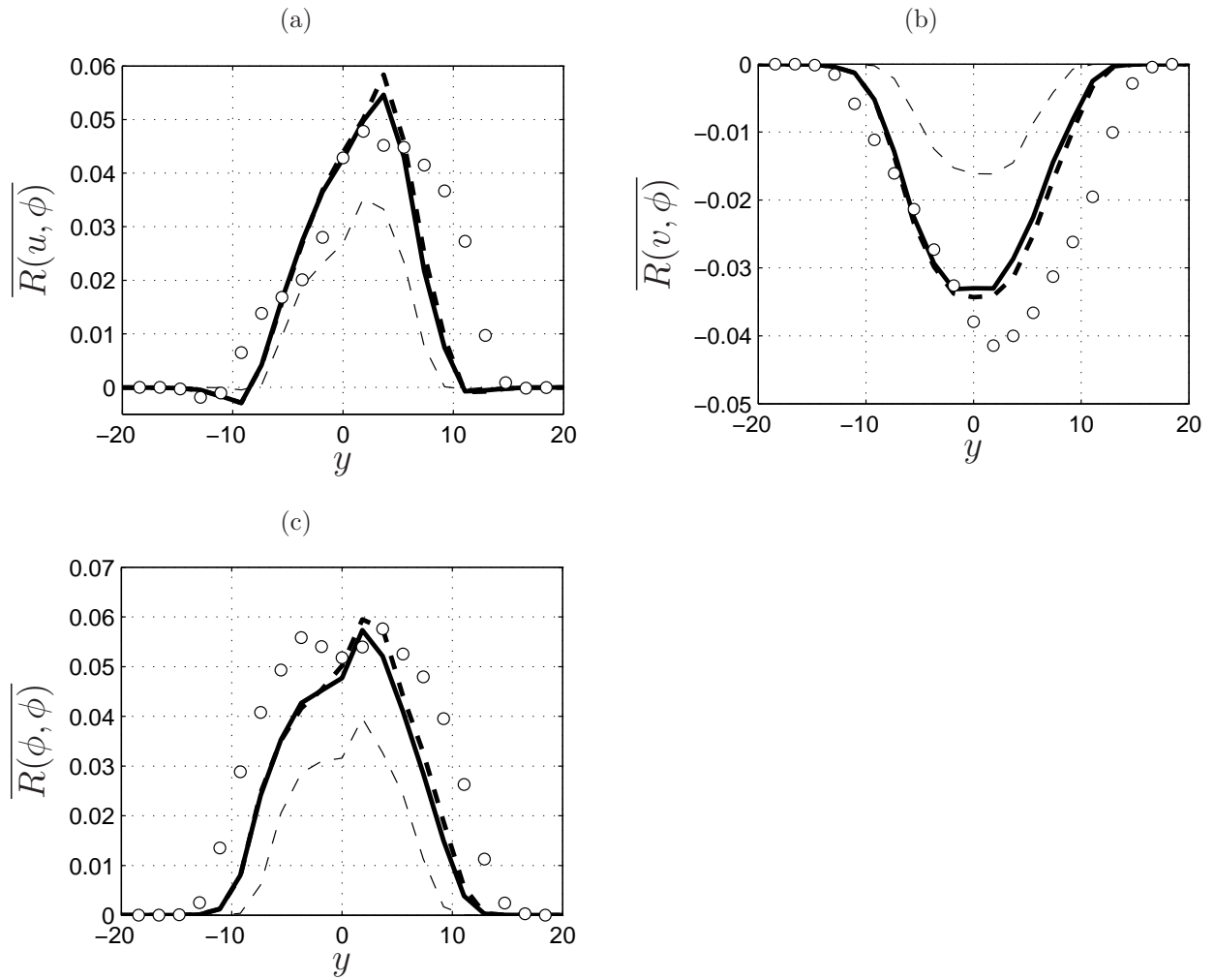


Figure 36: Cross-stream variations of some of the components of \overline{R} at $t = 60$. The thick solid and dashed lines denote VSF MDF predictions via M1 and M2, respectively. The thin dashed line denote the predictions using Smagorinsky closure. The circles show the filtered DNS data.

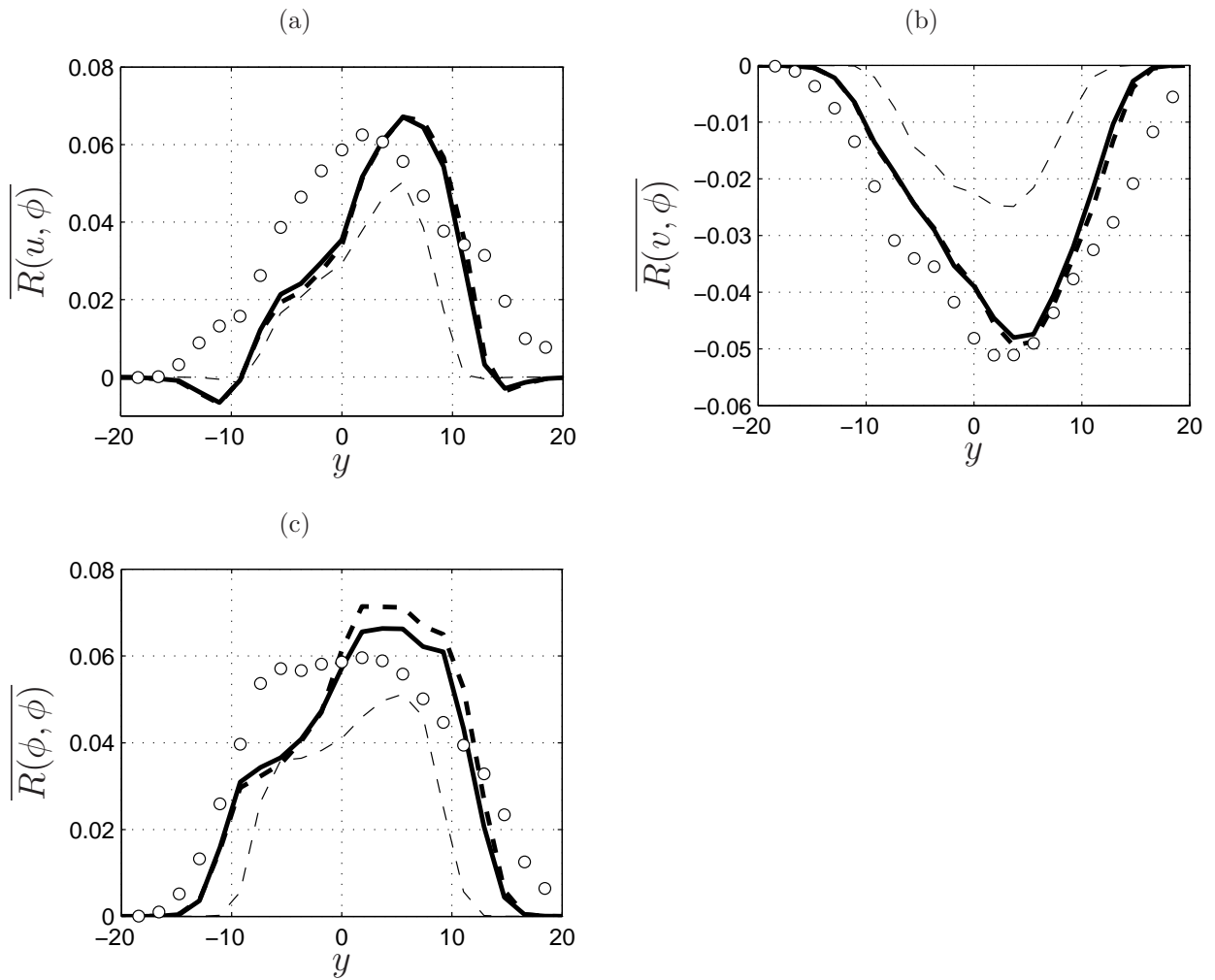


Figure 37: Cross-stream variations of some of the components of \overline{R} at $t = 80$. The thick solid and dashed lines denote VSFMDF predictions via M1 and M2, respectively. The thin dashed line denote the predictions using Smagorinsky closure. The circles show the filtered DNS data.

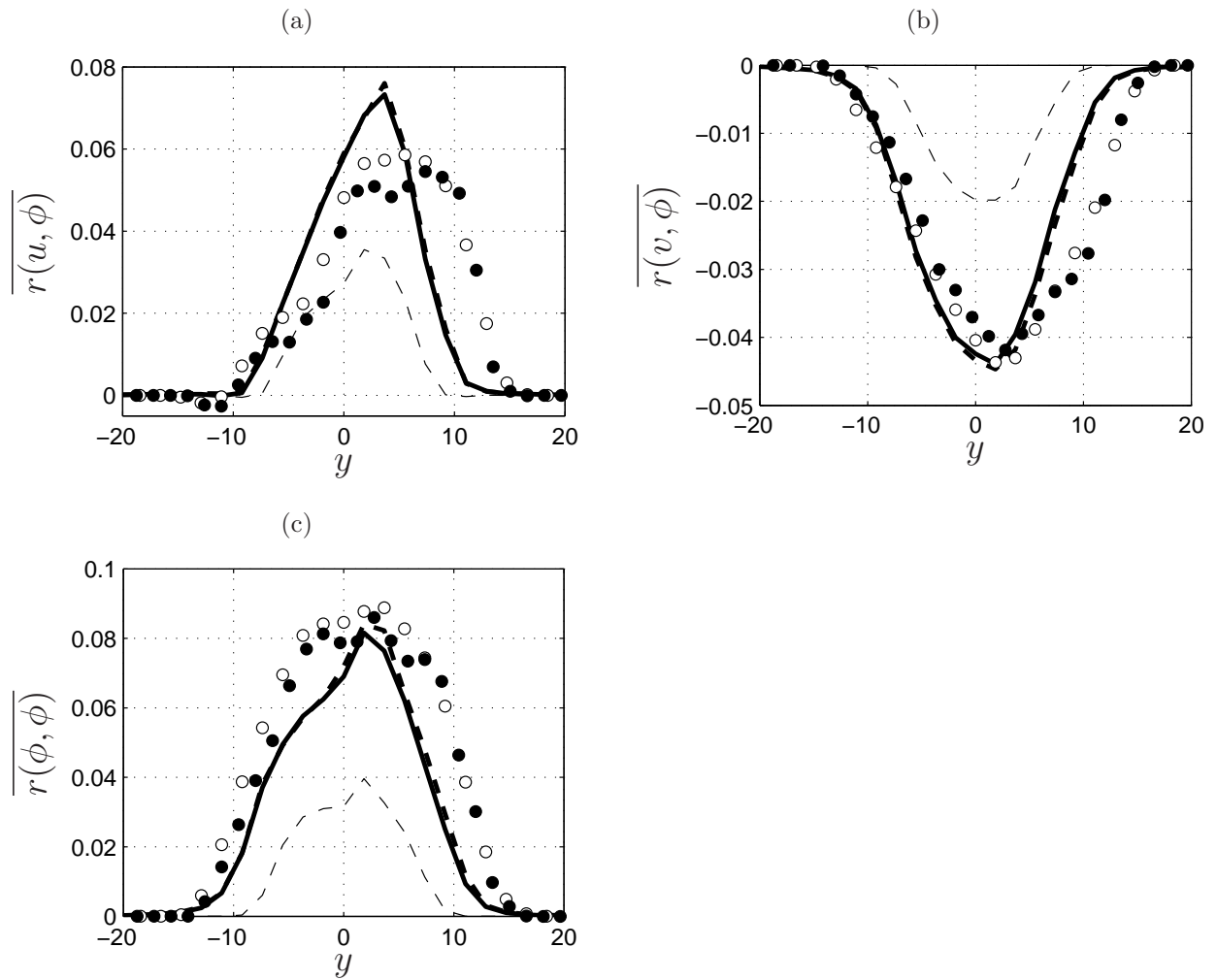


Figure 38: Cross-stream variations of \bar{r} at $t = 60$. The thick solid and dashed lines denote VSFMDF predictions via M1 and M2, respectively. The thin dashed line denote the predictions using Smagorinsky closure. The white and black circles show the filtered and unfiltered DNS data, respectively.

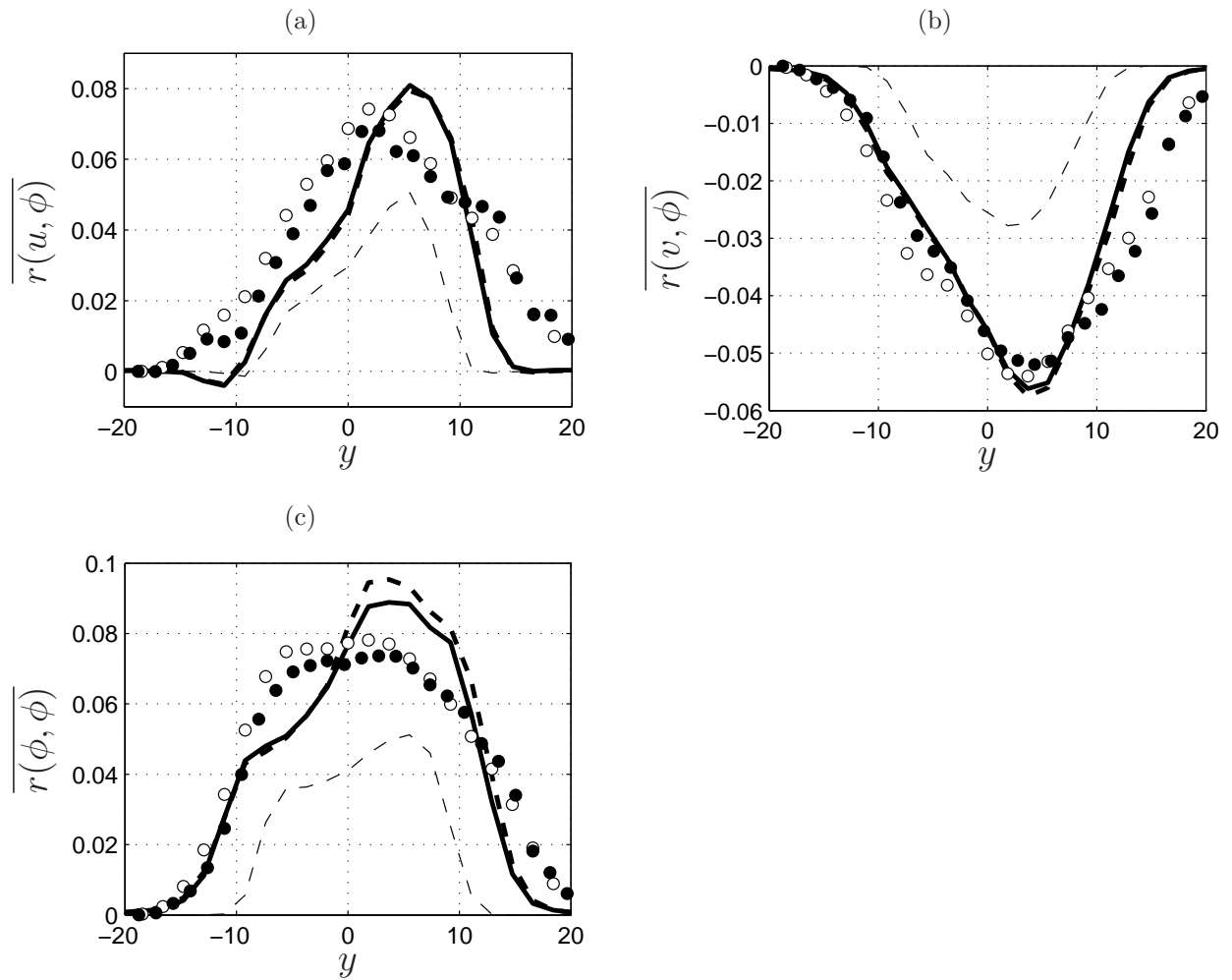
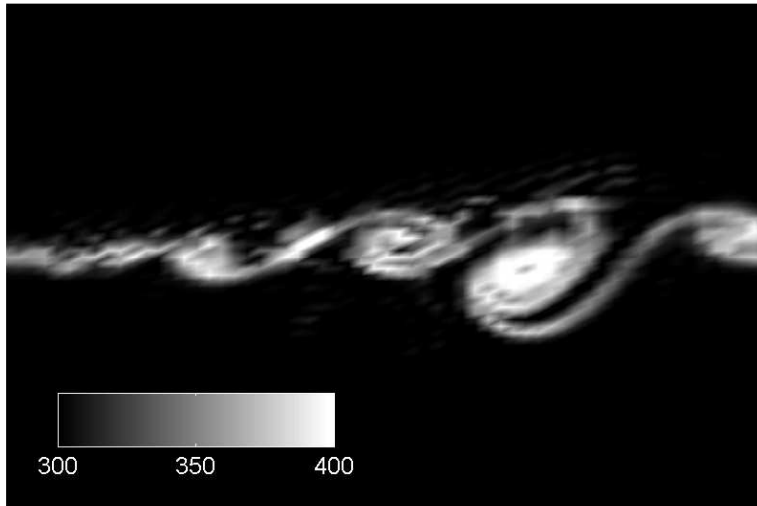


Figure 39: Cross-stream variations of \bar{r} at $t = 80$. The thick solid and dashed lines denote VSFMDF predictions via M1 and M2, respectively. The thin dashed line denote the predictions using Smagorinsky closure. The white and black circles show the filtered and unfiltered DNS data, respectively.

(a)



(b)

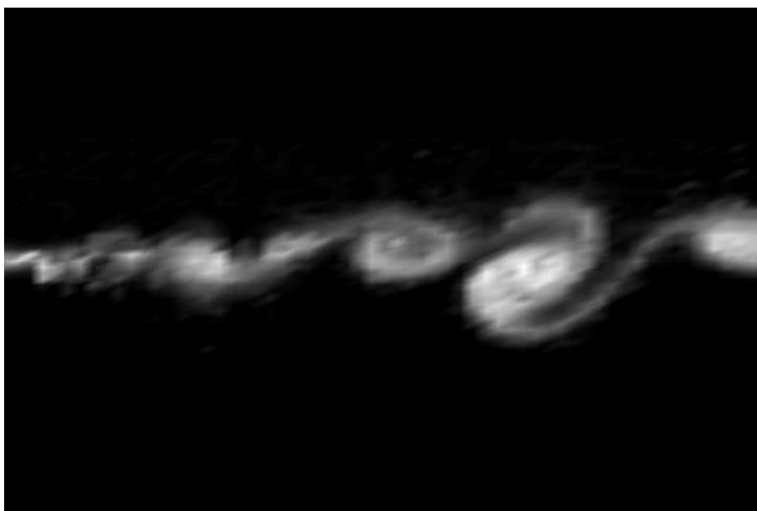


Figure 40: Contours of the instantaneous temperature [$^{\circ}K$] field on a spanwise plane as obtained by: (a) LES-FD, (b) MC.

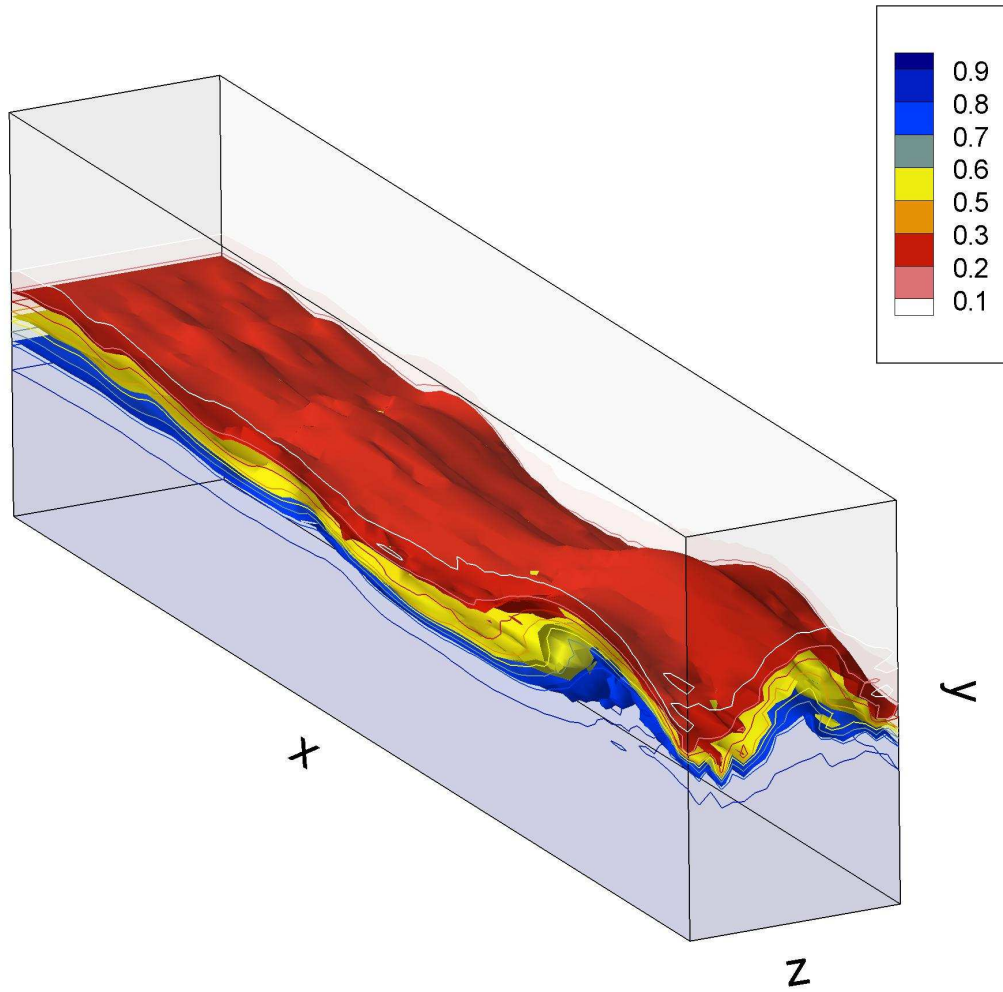


Figure 41: Contour surfaces of the instantaneous filtered passive scalar field in the 3D spatial mixing layer simulations as obtained by VSF MDF.

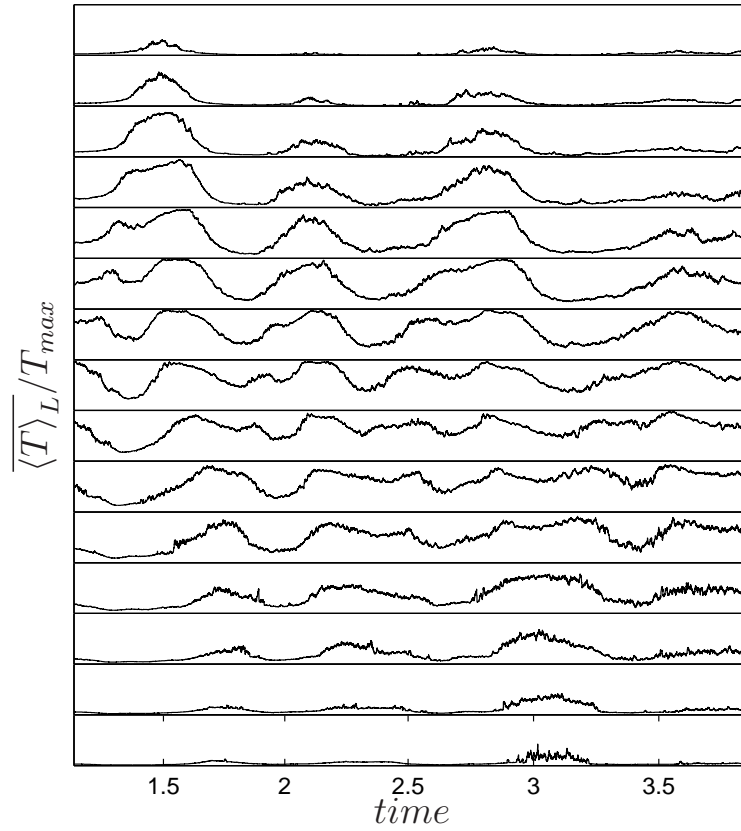


Figure 42: Time series of filtered temperature field at different cross-stream locations across the layer and $x = 45.7 \text{ cm}$ as obtained by VSF MDF. T_{max} denote the maximum temperature recorded by each probe.

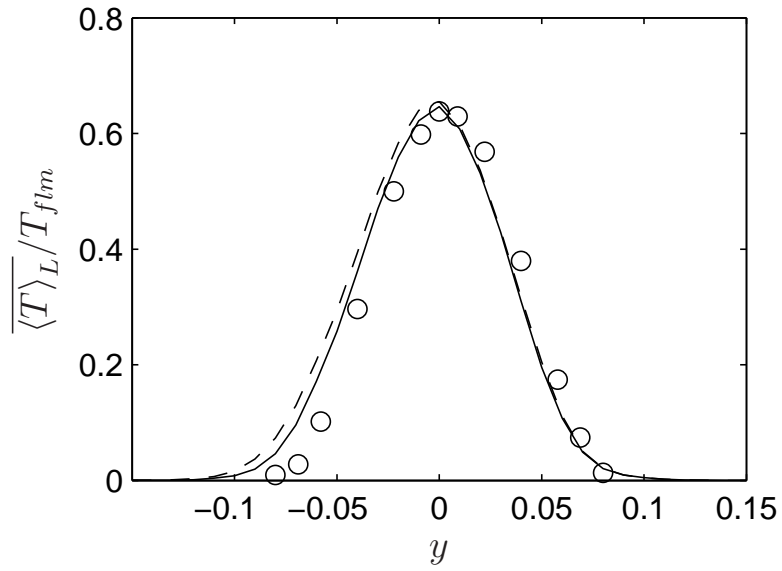


Figure 43: Cross-stream variations of time-averaged filtered temperature field for the case with $\phi = 1$. The solid and dashes lines denote VSF MDF predictions using M1 and M2, respectively. The circles denote experimental data. T_{flm} denotes the adiabatic flame temperature.

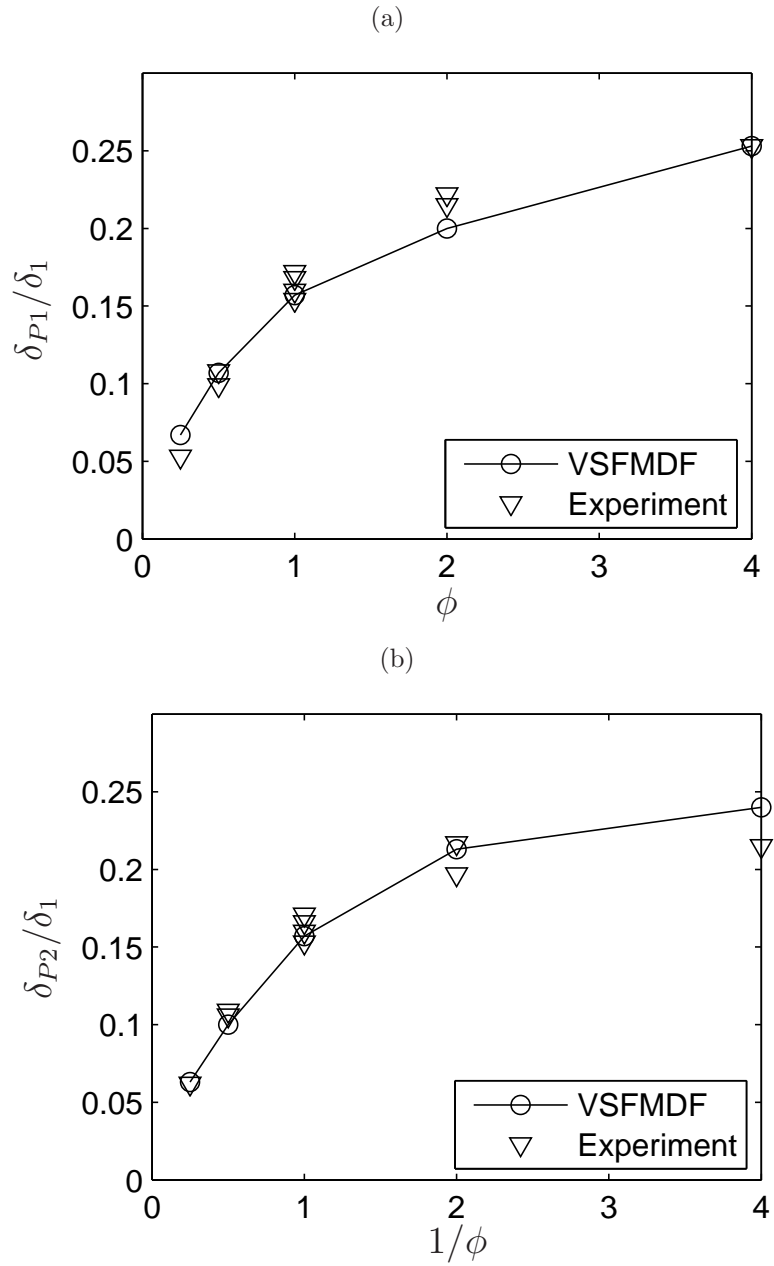


Figure 44: Product thicknesses as obtained by VSF MDF: (a) Product thickness based on high-speed stream concentration, (b) Product thickness based on low-speed stream concentration.

4.0 CONCLUSIONS

The filtered density function (FDF) methodology has proven very effective for large eddy simulation (LES) of turbulent reactive flows. In previous investigations, the marginal FDF of the scalar or that of the velocity were considered. The objective of this dissertation is to develop the joint velocity-scalar FDF methodology. For this purpose, the exact transport equation governing the evolution of FDF is derived. It is shown that effects of SGS convection and chemical reaction appear in closed forms. The unclosed terms are modeled in a fashion similar to those typically followed in probability density function (PDF) methods in Reynolds-averaged simulations (RAS). The modeled FDF transport equation is solved numerically by a Lagrangian Monte Carlo (MC) scheme via consideration of a system of equivalent stochastic differential equations (SDEs). These SDEs are discretized via the Euler-Maruyama discretization.

First, the joint velocity-scalar FDF (VSFDF) is considered for constant-density flows. To simulate variable-density flows, next the joint “velocity-scalar filtered mass density function” (VSF MDF) is considered. The consistency and accuracy of both VSFDF and VSF MDF are assessed in LES of temporally developing mixing layers involving the transport of a passive scalar. This assessment is made by comparing the moments obtained from the MC solver with those obtained by solving the corresponding transport equations directly by finite-difference method (LES-FD). The LES-FD equations are closed by including the moments from the MC solver. The consistency of the MC solution are demonstrated by good agreements of the first two SGS moments with those obtained by LES-FD.

The FDF predictions are compared with those obtained using the Smagorinsky⁴² SGS closure. All of the results are also compared with direct numerical simulation (DNS) data of the same flow. It is shown that the FDF performs well in predicting some of the phe-

nomena pertaining to the SGS transport. Most of the overall flow statistics, including the mean field, the resolved and total stresses are in good agreements with DNS data. The VSFMDf methodology is applied to a three-dimensional spatially developing shear layer. This flow involves a fast chemical reaction with non-premixed reactants. The predictions are appraised by comparison with laboratory data. The agreement is observed to be very good and VSFMDf predictions capture many of the features of this flow as observed in the experiment.

To evaluate the computational requirements of VSFDF, the computational times are measured for the 3D temporal mixing layer simulations. Table 2 lists the CPU times corresponding to LES via the Smagorinsky⁴² SGS closure, VSFDF; and direct numerical simulation (DNS). The CPU times are normalized by that required in the simulation via the Smagorinsky model. The simulations are performed on SGI Altix 3300 computers with 1.3 GHz Intel Itanium processors. In VSFDF simulations, 320 particles per grid point ($N_E = 40$) are used. It is observed that the computational time for VSFDF is significantly less than that of DNS. Considering the close agreements between VSFDF and DNS results, this suggests that VSFDF can be employed for simulations of reacting flows for which DNS is not feasible.

Table 2: Computational times for the three-dimensional temporal mixing layer simulations.

Simulation	Grid resolution	Normalized CPU time per unit simulation time
Smagorinsky	33^3	1
VSFDF	33^3	15.6
DNS	193^3	1655.2

Some suggestions for possible future work are:

- Development of a stochastic FDF formulation to include the SGS mixing frequency. In the current FDF formulations, this quantity is modeled in an *ad hoc* manner. A stochastic differential equation may be devised as a model for the SGS mixing frequency in a fashion similar to that in RAS. ^{56,85}
- Implementation of higher order closures for the generalized Langevin model parameter G_{ij} . ⁷³ The model parameter considered in this dissertation correspond to Rotta's closure in RAS. ^{1,86} Higher order closure similar to those considered in RAS ^{55,73} may be implemented.
- Introduction of a stochastic model suitable for high Mach number flows. To account for the effect of compressibility, the system of stochastic differential equations (SDEs) should include the corresponding model for thermodynamical variables such as the pressure and the internal energy, similar to those in RAS. ^{87,88}
- Extension of the FDF methodology for flows with differential diffusion effects. ⁸⁹⁻⁹⁴ The models developed in this dissertation are limited to flows with unity Prandtl and/or Schmidt numbers.
- Extension of the VSFMDf for simulation of complex turbulent reacting flows. The SFDF has proven very effective in LES of turbulent flames. ^{15,23} It is recommended to implement the VSFMDf for prediction of these flames.

BIBLIOGRAPHY

- [1] S. B. Pope. *Turbulent Flows*. Cambridge University Press, Cambridge, UK, 2000.
- [2] S. B. Pope. Computations of turbulent combustion: Progress and challenges. *Proc. Combust. Inst.*, 23:591–612, 1990.
- [3] P. Givi. Filtered density function for subgrid scale modeling of turbulent combustion. *AIAA J.*, 2005. in press.
- [4] P. Givi. Model free simulations of turbulent reactive flows. *Prog. Energy Combust. Sci.*, 15:1–107, 1989.
- [5] N. Peters. *Turbulent Combustion*. Cambridge University Press, Cambridge, UK, 2000.
- [6] R. W. Bilger, S. B. Pope, K. N. C. Bray, and J. F. Driscoll. Paradigms in turbulent combustion research. *Proc. Combust. Inst.*, 30:21–42, 2005.
- [7] C. K. Madnia and P. Givi. Direct numerical simulation and large eddy simulation of reacting homogeneous turbulence. In B. Galperin and S. A. Orszag, editors, *Large Eddy Simulations of Complex Engineering and Geophysical Flows*, chapter 15, pages 315–346. Cambridge University Press, Cambridge, England, 1993.
- [8] F. Gao and E. E. O’Brien. A large-eddy simulation scheme for turbulent reacting flows. *Phys. Fluids A*, 5(6):1282–1284, 1993.
- [9] P. J. Colucci, F. A. Jaber, P. Givi, and S. B. Pope. Filtered density function for large eddy simulation of turbulent reacting flows. *Phys. Fluids*, 10(2):499–515, 1998.
- [10] F. A. Jaber, P. J. Colucci, S. James, P. Givi, and S. B. Pope. Filtered mass density function for large eddy simulation of turbulent reacting flows. *J. Fluid Mech.*, 401: 85–121, 1999.
- [11] L. Y. M. Gicquel, P. Givi, F. A. Jaber, and S. B. Pope. Velocity filtered density function for large eddy simulation of turbulent flows. *Phys. Fluids*, 14(3):1196–1213, 2002.
- [12] X. Y. Zhou and J. C. F. Pereira. Large eddy simulation (2D) of a reacting plane mixing layer using filtered density function. *Flow. Turbul. Combust.*, 64:279–300, 2000.

- [13] S. James and F. A. Jaber. Large scale simulations of two-dimensional nonpremixed methane jet flames. *Combust. Flame*, 123(4):465–487, 2000.
- [14] V. Raman, H. Pitsch, and R. O. Fox. Hybrid large-eddy simulation/Lagrangian filtered-density-function approach for simulating turbulent combustion. *Combust. Flame*, 143(1-2):56–78, 2005.
- [15] M. R. H. Sheikhi, T. G. Drozda, P. Givi, F. A. Jaber, and S. B. Pope. Large eddy simulation of a turbulent nonpremixed piloted methane jet flame (Sandia flame D). *Proc. Combust. Inst.*, 30:549–556, 2005.
- [16] E. van Vliet, J. J. Derksen, and H. E. A. van den Akker. Turbulent mixing in a tubular reactor: Assessment of an FDF/LES approach. *AIChE J.*, 51(3):725–739, 2005.
- [17] S. C. Garrick, F. A. Jaber, and P. Givi. Large eddy simulation of scalar transport in a turbulent jet flow. In D. Knight and L. Sakell, editors, *Recent Advances in DNS and LES*, volume 54 of *Fluid Mechanics and its Applications*, pages 155–166. Kluwer Academic Publishers, The Netherlands, 1999.
- [18] S. Heinz. On Fokker-Planck equations for turbulent reacting flows. part 2. filter density function for large eddy simulation. *Flow. Turbul. Combust.*, 70(1-4):153–181, 2003.
- [19] V. Raman, H. Pitsch, and R. O. Fox. Consistent hybrid LES-FDF formulation for the simulation of turbulent combustion. In *Annual Research Briefs - 2004*, pages 231–241. Center for Turbulence Research, NASA Ames/Stanford University, 2004.
- [20] L. Lu, Z. Ren, V. Raman, S. B. Pope, and H. Pitsch. LES/FDF/ISAT computations of turbulent flames. In *Proceedings of the 2004 Summer Program*, pages 283–294. Center for Turbulence Research, NASA Ames/Stanford University, 2004.
- [21] M. Carrara and P. Desjardin. A probabilistic approach to modeling separated two-phase flows for large eddy simulation. *Bull. Amer. Phys. Soc.*, 49(9):136, 2004.
- [22] V. Raman, D. Cook, and H. Pitsch. Hybrid LES/FDF simulation of a non-premixed bluff-body stabilized flame. *Bull. Amer. Phys. Soc.*, 49(9):57–58, 2004.
- [23] T. G. Drozda. *Implementation of LES/SFMDF for prediction of non-premixed turbulent flames*. Ph.D. Thesis, Department of Mechanical Engineering, University of Pittsburgh, Pittsburgh, PA, 2005.
- [24] J. Réveillon and L. Vervisch. Subgrid-scale turbulent micromixing: Dynamic approach. *AIAA J.*, 36(3):336–341, 1998.
- [25] C. M. Cha and P. Troulet. A subgrid-scale mixing model for large-eddy simulations of turbulent reacting flows using the filtered density function. *Phys. Fluids*, 15(6):1496–1504, 2003.

- [26] C. Tong. Measurements of conserved scalar filtered density function in a turbulent jet. *Phys. Fluids*, 13(10):2923–2937, 2001.
- [27] D. Wang and C. Tong. Conditionally filtered scalar dissipation, scalar diffusion, and velocity in a turbulent jet. *Phys. Fluids*, 14(7):2170–2185, 2002.
- [28] A. G. Rajagopalan and C. Tong. Experimental investigation of scalar-scalar-dissipation filtered joint density function and its transport equation. *Phys. Fluids*, 15(1):227–244, 2003.
- [29] D. Wang, C. Tong, and S. B. Pope. Experimental study of velocity filtered joint density function for large eddy simulation. *Phys. Fluids*, 16(10):3599–3613, 2004.
- [30] D. Wang and C. Tong. Experimental study of velocity-scalar filtered joint density function for LES of turbulent combustion. *Proc. Combust. Inst.*, 30:567–574, 2005.
- [31] A. Chandy, G. M. Goldin, and S. H. Frankel. Modeling turbulent nonpremixed jet flames using Fluent’s PDF transport model: Effect of mixing model on flame extinction. In *30th International Symposium on Combustion, Abstracts of Work-In-Progress Posters*, page 447, Pittsburgh, PA, 2004. The Combustion Institute.
- [32] D. J. Glaze, S. H. Frankel, and J. C. Hewson. Non-premixed turbulent jet mixing using LES with the FMDF model. In *30th International Symposium on Combustion, Abstracts of Work-In-Progress Posters*, page 79, Pittsburgh, PA, 2004. The Combustion Institute.
- [33] R. O. Fox. *Computational Models for Turbulent Reacting Flows*. Cambridge University Press, Cambridge, UK, 2003.
- [34] S. Heinz. *Statistical Mechanics of Turbulent Flows*. Springer, New York, NY, 2003.
- [35] F. A. Jaber, C. K. Madnia, and P. Givi. Large eddy simulation of heat and mass transport in turbulent flows. In W. J. Minkowycz, E. M. Sparrow, and J. Y. Murthy, editors, *Handbook of Numerical Heat Transfer*, chapter 5. John Wiley & Sons, Inc., New York, NY, second edition, 2005. in press.
- [36] M. R. H. Sheikhi, T. G. Drozda, P. Givi, and S. B. Pope. Joint velocity-scalar filtered density function for large eddy simulation of turbulent flows. In *Bull. Amer. Phys. Soc.*, volume 47(10), Program of the 55th Annual Meeting of the Division of Fluid Dynamics of the American Physical Society, page 141, Dallas, TX, November 24-26, 2002.
- [37] T. G. Drozda, M. R. H. Sheikhi, P. Givi, and S. B. Pope. Large eddy simulation of scalar transport in a turbulent mixing layer. In *Chemical and Physical Processes in Combustion*, Technical Meeting of the Eastern States Section of the Combustion Institute, pages 237–240, University Park, PA, October 26-29, 2003.
- [38] M. R. H. Sheikhi, T. G. Drozda, P. Givi, and S. B. Pope. Velocity-scalar filtered density function for large eddy simulation of turbulent flows. *Phys. Fluids*, 15(8):2321–2337, 2003.

- [39] M. R. H. Sheikhi, P. Givi, and S. B. Pope. Joint velocity-scalar filtered mass density function for large eddy simulation of turbulent reacting flows. In *Bull. Amer. Phys. Soc.*, volume 49(9), Program of the 57th Annual Meeting of the Division of Fluid Dynamics of the American Physical Society, page 217, Seattle, WA, November 21-23, 2004.
- [40] M. R. H. Sheikhi, P. Givi, and S. B. Pope. Latest developments in filtered density function formulation. Proceedings of the 4th Joint Meeting of the U.S. Sections of the Combustion Institute, page 60, Philadelphia, PA, March 20-23, 2005.
- [41] M. R. H. Sheikhi, P. Givi, and S. B. Pope. Implementation of the velocity-scalar filtered mass density function for large eddy simulation of turbulent reacting flows. In *Bull. Amer. Phys. Soc.*, volume 50(9), Program of the 58th Annual Meeting of the Division of Fluid Dynamics of the American Physical Society, page 261, Chicago, IL, November 20-22, 2005.
- [42] J. Smagorinsky. General circulation experiments with the primitive equations. I. The basic experiment. *Mon. Weather Rev.*, 91(3):99–164, 1963.
- [43] P. A. Libby and F. A. Williams, editors. *Turbulent Reacting Flows*, volume 44 of *Topics in Applied Physics*. Springer-Verlag, Heidelberg, 1980.
- [44] S. B. Pope. PDF methods for turbulent reactive flows. *Prog. Energy Combust. Sci.*, 11: 119–192, 1985.
- [45] R. W. Bilger. Molecular transport effects in turbulent diffusion flames at moderate Reynolds number. *AIAA J.*, 20:962–970, 1982.
- [46] U. Piomelli. Large-eddy simulation: Achievements and challenges. *Progress in Aerospace Sciences*, 35:335–362, 1999.
- [47] C. Meneveau and J. Katz. Scale-invariance and turbulence models for large-eddy simulations. *Annu. Rev. Fluid Mech.*, 32:1–32, 2000.
- [48] B. J. Geurts, editor. *Modern Simulation Strategies for Turbulent Flow*. R. T. Edwards, Inc., Philadelphia, PA, 2001.
- [49] P. Sagaut. *Large Eddy Simulation for Incompressible Flows*. Springer, New York, NY, 2001.
- [50] E. E. O’Brien. The probability density function (PDF) approach to reacting turbulent flows. In Libby and Williams⁴³, chapter 5, pages 185–218.
- [51] B. Vreman, B. Geurts, and H. Kuerten. Realizability conditions for the turbulent stress tensor in large-eddy simulation. *J. Fluid Mech.*, 278:351–362, 1994.
- [52] S. Karlin and H. M. Taylor. *A Second Course in Stochastic Processes*. Academic Press, New York, NY, 1981.

- [53] N. Wax. *Selected Papers on Noise and Stochastic Processes*. Dover, New York, NY, 1954.
- [54] C. W. Gardiner. *Handbook of Stochastic Methods*. Springer-Verlag, New York, NY, 1990.
- [55] D. C. Haworth and S. B. Pope. A Generalized Langevin model for turbulent flows. *Phys. Fluids*, 29(2):387–405, 1986.
- [56] T. D. Dreeben and S. B. Pope. Probability density function and Reynolds-stress modeling of near-wall turbulent flows. *Phys. Fluids*, 9(1):154–163, 1997.
- [57] H. Risken. *The Fokker-Planck Equation, Methods of Solution and Applications*. Springer-Verlag, New York, NY, 1989.
- [58] M. Muradoglu, P. Jenny, S. B. Pope, and D. A. Caughey. A consistent hybrid-volume/particle method for the PDF equations of turbulent reactive flows. *J. Comp. Phys.*, 154(2):342–371, 1999.
- [59] M. Muradoglu, S. B. Pope, and D. A. Caughey. The hybrid method for the PDF equations of turbulent reactive flows: Consistency conditions and correction algorithms. *J. Comp. Phys.*, 172(2):841–878, 2001.
- [60] P. E. Kloeden, E. Platen, and H. Schurz. *Numerical Solution of Stochastic Differential Equations through Computer Experiments*. Springer-Verlag, New York, NY, corrected second printing edition, 1997.
- [61] I. I. Gikhman and A. V. Skorokhod. *Stochastic Differential Equations*. Springer-Verlag, New York, NY, 1972.
- [62] M. H. Carpenter. A high-order compact numerical algorithm for supersonic flows. In K. W. Morton, editor, *Twelfth International Conference on Numerical Methods in Fluid Dynamics*, volume 371 of *Lecture Notes in Physics*, pages 254–258. Springer-Verlag, New York, NY, 1990.
- [63] C. A. Kennedy and M. H. Carpenter. Several new numerical methods for compressible shear-layer simulations. *Appl. Num. Math.*, 14:397–433, 1994.
- [64] J. J. Riley and R. W. Metcalfe. Direct numerical simulations of a perturbed, turbulent mixing layer. AIAA Paper 80-0274, 1980.
- [65] N. D. Sandham and W. C. Reynolds. Three-dimensional simulations of large eddies in the compressible mixing layer. *J. Fluid Mech.*, 224:133–158, 1991.
- [66] R. D. Moser and M. M. Rogers. The three-dimensional evolution of a plane mixing layer: Pairing and transition to turbulence. *J. Fluid Mech.*, 247:275–320, 1993.

- [67] B. Vreman, B. Geurts, and H. Kuerten. Large-eddy simulation of the turbulent mixing layer. *J. Fluid Mech.*, 339:357–390, 1997.
- [68] R. W. Metcalfe, S. A. Orszag, M. E. Brachet, S. Menon, and J. J. Riley. Secondary instabilities of a temporally growing mixing layer. *J. Fluid Mech.*, 184:207–243, 1987.
- [69] S. J. Lin and G. M. Corcos. The mixing layer: Deterministic models of a turbulent flow. Part 3. The effect of plane strain on the dynamics of streamwise vortices. *J. Fluid Mech.*, 141:139–178, 1984.
- [70] R. D. Moser and M. M. Rogers. The three-dimensional evolution of a plane mixing layer: the Kelvin-Helmholtz rollup. *J. Fluid Mech.*, 243:183–226, 1992.
- [71] R. D. Moser and M. M. Rogers. Spanwise scale selection in plane mixing layers. *J. Fluid Mech.*, 247:321–337, 1993.
- [72] G. Erlebacher, M. Y. Hussaini, C. G. Speziale, and T. A. Zang. Toward the large eddy simulation of compressible turbulent flows. *J. Fluid Mech.*, 238:155–185, 1992.
- [73] S. B. Pope. On the relation between stochastic Lagrangian models of turbulence and second-moment closures. *Phys. Fluids*, 6(2):973–985, 1994.
- [74] R. S. Rogallo and P. Moin. Numerical simulation of turbulent flow. *Annu. Rev. Fluid Mech.*, 16:99–137, 1984.
- [75] R. W. Bilger. Future progress in turbulent combustion research. *Prog. Energy Combust. Sci.*, 26(4):367–380, 2000.
- [76] M. G. Mungal and P. E. Dimotakis. Mixing and combustion with low heat release in a turbulent mixing layer. *J. Fluid Mech.*, 148:349–382, 1984.
- [77] N. D. Sandham and W. C. Reynolds. Some inlet-plane effects on the numerically simulated spatially-developing mixing layer. In *Turbulent Shear Flows 6*, pages 441–454. Springer-Verlag, New York, NY, 1989.
- [78] S. B. Pope. Ten questions concerning the large-eddy simulation of turbulent flows. *New J. Phys.*, 6:35–58, 2004.
- [79] J. Giridhar. *A framework for large eddy simulation of incompressible flows with error control*. Ph.D. Thesis, Sibley School of Mechanical and Aerospace Engineering, Cornell University, Ithaca, NY, 2005.
- [80] T. J. Poinso and S. K. Lele. Boundary conditions for direct simulations of compressible viscous flows. *J. Comp. Phys.*, 101:104–129, 1992.
- [81] D. H. Rudy and J. C. Strikwerda. Boundary conditions for subsonic compressible Navier-Stokes calculations. *J. Comp. Phys.*, 36:327–338, 1980.

- [82] T. G. Drozda. Consistency assessment of velocity-scalar filtered density function for large-eddy simulation of turbulent flows. M.S. Thesis, Department of Mechanical and Aerospace Engineering, University at Buffalo, State University of New York, Buffalo, NY, 2002.
- [83] A. Yoshizawa. Statistical theory for compressible turbulent shear flows, with the application to subgrid modeling. *Phys. Fluids*, 29(7):2152–2164, 1986.
- [84] P. Moin, W. Squires, W. H. Cabot, and S. Lee. A dynamic subgrid-scale model for compressible turbulence and scalar transport. *Phys. Fluids A*, 3(11):2746–2757, 1991.
- [85] T. D. Dreeben and S. B. Pope. Probability density function / Monte Carlo simulation of near-wall turbulent flows. *J. Fluid Mech.*, 357:141–166, 1998.
- [86] David C. Wilcox. *Turbulence Modeling for CFD*. DCW Industries, Inc., La Cañada, CA, 1993.
- [87] B. J. Delarue and S. B. Pope. Application of PDF methods to compressible turbulent flows. *Phys. Fluids*, 9(9):2704–2715, 1997.
- [88] B. J. Delarue and S. B. Pope. Calculations of subsonic and supersonic turbulent reacting mixing layers using probability density function methods. *Phys. Fluids*, 10(2):487–498, 1998.
- [89] F. A. Jaber, R. S. Miller, F. Mashayek, and P. Givi. Differential diffusion in binary scalar mixing and reaction. *Combust. Flame*, 109(4):561–577, 1997.
- [90] L. L. Smith, R. W. Dibble, L. Talbot, R. S. Barlow, and C. D. Carter. Laser Raman scattering measurements of differential molecular diffusion in nonreacting turbulent jets of H_2/CO_2 mixing with air. *Phys. Fluids*, 7(6):1455–1466, 1995.
- [91] A. R. Kerstein, M. A. Cremer, and P. A. McMurtry. Scaling properties of differential molecular diffusion effects in turbulence. *Phys. Fluids*, 7(8):1999–2007, 1995.
- [92] M. B. Long, S. H. Starner, and R. W. Bilger. Differential diffusion in jets using joint PLIF and Lorenz-Mie imaging. *Combust. Sci. and Tech.*, 92:209–224, 1993.
- [93] V. Nilsen and G. Kosály. Differential diffusion in turbulent reacting flows. *Combust. Flame*, 17(3):493–513, 1999.
- [94] P. K. Yeunga, S. Xu, and K. R. Sreenivasan. Schmidt number effects on turbulent transport with uniform mean scalar gradient. *Phys. Fluids*, 14(12):4178–4191, 2002.